1-1-2014

Shape-Control and Doping of Lanthanides and Transition Metal Oxide Nanocrystals With Tailored Properties and Their Shape-Directed Self-Assembly

Taejong Paik
University of Pennsylvania, paiktae@gmail.com

Shape-Control and Doping of Lanthanides and Transition Metal Oxide Nanocrystals With Tailored Properties and Their Shape-Directed Self-Assembly

Abstract

Lanthanide and transition metal oxides are widely used in various applications such phosphors, lasers, magnets, and catalysts, and have formed an important platform for biomedical research and clinical medicine. The synthesis of highly uniform nanomaterials with controlled size, shape, and compositions is paramount to precisely understanding their physical properties and to arrange them into highly ordered arrays to design functional metamaterials. Herein, I describe novel chemistry to synthesize highly uniform lanthanide and transition metal oxide nanocrystals. The size, shape, and compositions of lanthanide-based nanocrystals are systematically controlled with the addition of alkali metal salts. The reaction mechanism is investigated to understand the nanocrystal growth and characterized by X-ray measurements and microscopic analysis. The magnetic resonance relaxometry and the optical properties including phosphorescece, upconversion, and X-ray excited optical luminescence are investigated, which make these nanocrystals a promising platform for multimodal imaging in biomedical applications. The shape-controlled synthesis of isotopically labeled rare earth fluoride nanocrystals is also demonstrated, which is designed for *in vitro* and *ex vivo* radioisotopic detection, as well as non-invasive nuclear, optical radioluminescence, and magnetic resonance imaging. Using anisotropic nanocrystal building blocks, shape-directed liquid crystalline self-assembly is presented to understand how complex anisotropic superstructures can be designed with single and binary components in a predictable manner. Finally, transition metal oxides such as tungsten, oxide, titanium oxide, and vanadium oxide are synthesized using non-injection heating up method. In addition, I demonstrate that vanadium oxide nanocrystal can be utilized as the precursors to fabricate thermochromic VO_2, which is an important building block for energy research, optics, and electronic devices.

Degree Type
Dissertation

Degree Name
Doctor of Philosophy (PhD)

Graduate Group
Chemistry

First Advisor
Christopher B. Murray

Keywords
Lanthanide, Nanocrystal, Self assembly, Shape control, Superlattice, Transition metal oxide

Subject Categories
Chemistry | Mechanics of Materials | Nanoscience and Nanotechnology

SHAPE-CONTROL AND DOPING OF LANTHANIDES AND TRANSITION METAL OXIDE

NANOCRYSTALS WITH TAILORED PROPERTIES AND THEIR SHAPE-DIRECTED SELF-

ASSEMBLY

Taejong Paik

A DISSERTATION

in

Chemistry

Presented to the Faculties of the University of Pennsylvania

in

Partial Fulfillment of the Requirements for the

Degree of Doctor of Philosophy

2014

Supervisor of Dissertation

_____

Dr. Christopher B. Murray

Richard Perry Professor of Chemistry and Materials Science and Engineering

Graduate Group Chairperson

_____

Dr. Gary A. Molander

Hirschmann-Makineni Professor of Chemistry

Dissertation Committee

Dr. Donald H. Berry, Professor of Chemistry

Dr. Cherie R. Kagan, Professor of Chemistry, and Materials Science and Engineering, and

Electrical and System Engineering

Dr. Eric J. Schelter, Professor of Chemistry

SHAPE-CONTROL AND DOPING OF LANTHANIDES AND TRANSITION METAL OXIDE

NANOCRYSTALS WITH TAILORED PROPERTIES AND THEIR SHAPE-DIRECTED SELF-

ASSEMBLY

COPYRIGHT

2014

Taejong Paik

To my wife, my son, and family

ACKNOWLEDGMENT

nanostructures. Hong's tireless work ethic was an inspiration, and helped both with the experimental data presented and also with furthering my knowledge of fabrication procedures in general. Finally, I also want to acknowledge the many collaborators I worked with outside of my group. Thanks to Ann-Marie Chacko and John Mikitsh for the work involving radiolabeling of nanocrystals. This work could not be done without their incredible support. I also would like to recognize Prof. Joseph Friedberg, Prof. Jarod Finlay, Michael Tenuto, and Andrew. M. Prantner, for their help in the nano-bio project, and Prof. Nadar Engheta and Humeyra Caglayan for the contribution to the metamaterial project.

Personally, I want to extend my deepest gratitude to my family, particularly my parents and my sister, for their support. My entire family has always inspired and encouraged me to give my best efforts in every situation and provided every resource so that I could focus on my researches. Specifically, I'd like to recognize the influence and immense happiness I get from being a father to my son, Jun-Hyuk. Last, but not least, I give me enduring gratitude to the love of my life, Yea Hwa, I cannot imagine how I could finish all of my work without her supports and encouragement. She has unselfishly spent most of her time helping me to focus while at the same time trying to develop her own career. All of my achievements have been ours, together, and I owe all of my success to her. She is a wonderful wife, mother, and great supporter. Thanks you for helping me over the last five years.

Thank you

ABSTRACT

SHAPE-CONTROL AND DOPING OF LANTHANIDES AND TRANSITION METAL OXIDE

NANOCRYSTALS WITH TAILORED PROPERTIES AND THEIR SHAPE-DIRECTED SELF—

ASSEMBLY

Taejong Paik

Dr. Christopher B. Murray

Lanthanide and transition metal oxides are widely used in various applications such phosphors, lasers, magnets, and catalysts, and have formed an important platform for biomedical research and clinical medicine. The synthesis of highly uniform nanomaterials with controlled size, shape, and compositions is paramount to precisely understanding their physical properties and to arrange them into highly ordered arrays to design functional metamaterials. Herein, I describe novel chemistry to synthesize highly uniform lanthanide and transition metal oxide nanocrystals. The size, shape, and compositions of lanthanide-based nanocrystals are systematically controlled with the addition of alkali metal salts. The reaction mechanism is investigated to understand the nanocrystal growth and characterized by X-ray measurements and microscopic analysis. The magnetic resonance relaxometry and the optical properties including phosphorescece, upconversion, and X-ray excited optical luminescence are investigated, which make these nanocrystals a promising platform for multimodal imaging in biomedical applications. The shape-controlled synthesis of isotopically labeled rare earth fluoride nanocrystals is also demonstrated, which is designed for *in vitro* and *ex vivo* radioisotopic detection, as well as non-invasive nuclear, optical radioluminescence, and magnetic resonance imaging. Using anisotropic nanocrystal building blocks, shape-directed liquid crystalline self-assembly is presented to understand how complex anisotropic superstructures can be designed with single and binary components in a predictable manner. Finally, transition metal oxides such as tungsten, oxide, titanium oxide, and

vanadium oxide are synthesized using non-injection heating up method. In addition, I demonstrate that vanadium oxide nanocrystal can be utilized as the precursors to fabricate thermochromic VO_2, which is an important building block for energy research, optics, and electronic devices.

TABLE OF CONTENTS

LIST OF TABLES

LIST OF ILLUSTRATIONS

CHAPTER 1. INTRODUCTION

1.1 Solution Phase Synthesis of Colloidal Nanocrystals.

Since the development of colloidal synthetic chemistry,[1,2] nanocrystals that have length scales between 1nm and 100nm have played an increasingly important role in many fields of emerging science and technology.[3] The properties of nanocrystals are tunable by changing their chemical composition and structural parameters. For example, semiconducting quantum dots, such as CdS, CdSe, CdTe and PbSe, have tunable absorption and emission properties based on their sizes due to the quantum confinement effect.[4] Electrical, optical, and magnetic properties are strongly size and shape dependant and by the choice of compositions among noble metals, transition metal oxides, metal chalcogenides, and lanthanides.[5]

Solution-based synthesis allows for the design of nearly monodisperse colloidal nanocrystals with precise control of their size and shape. Although various methods have been developed to synthesize colloidal nanocrystals, for example using sol-gel reactions[6], hydrothermal methods[7], and reverse micelle methods[8], the pioneering work to prepare nearly monodisperse nanocrystals (the standard deviation of size distribution is less than 5%) was done by Murray *et. al*,[1] for the synthesis of CdSe nanocrystals with precise size control. Later, this chemistry was named as the hot-injection method, where the supersaturated

metal precursor solution is injected into a high boiling point solvent at an elevated temperature. The rapid injection induces a burst nucleation in the reaction mixture forming homogeneous nanocrystalline nuclei. The reaction temperature decreases due to the injection of relatively cold reagents, and the formation of discrete nuclei results in the decreased monomer concentration in the reaction mixtures. These two effects lower the growth rate of nanocrystals after the precursor injection. Therefore, the nucleation and growth steps during the reaction are efficiently separated to prevent additional nucleation, which enables controlled growth from the uniform nuclei. The size distribution of nanocrystals can become more uniform by using subsequent size focusing growth and Ostwald ripening. The hot injection method is widely employed to synthesize II-IV, III-IV, IV-VI semiconducting quantum dots.
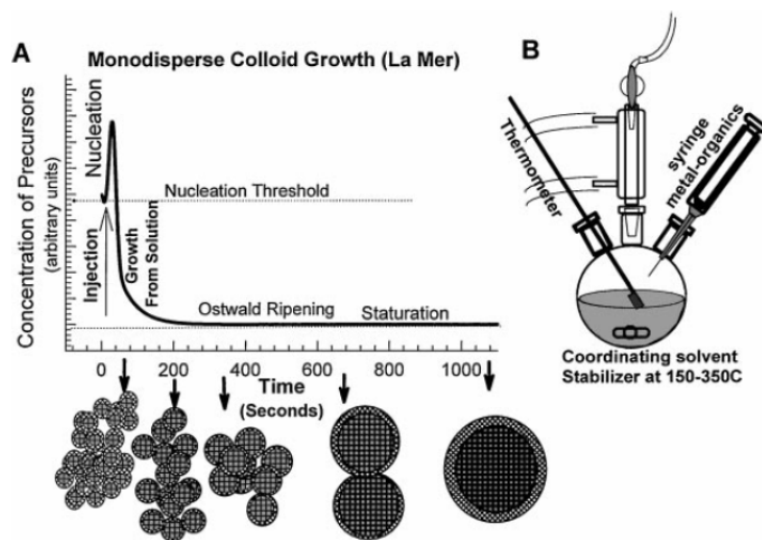
Figure 1.1. (A) General scheme for the growth of nanocrystals by the hot-injection method. (B) Illustration of the apparatus used in synthesizing monodisperse nanocrystals.(Adapted from reference 2)

Effective separation of the nucleation and growth processes to synthesize uniform nanocrystals also can be achieved by a non-injection method, as reported by Hyeon. *et. al.*[9,10] For the synthesis of iron oxide nanocrystals, metal complex precursors such as iron oleate are added to the reaction mixture before the mixture is heated. Nucleation and growth are controlled by the kinetics of precursor decomposition. At a certain temperature, sudden decomposition of the precursors into reactive monomers induces the burst nucleation, followed by sequential growth from the nuclei. The non-injection method is typically employed in the synthesis of metal oxides and widely used to synthesize metal chalcogenide and rare earth based nanocrystals.[11,12]

In order to understand the effect of the nanocrystal shape, it is important to develop a technique to precisely engineer the morphology of nanomaterials. Shape control of nanocrystals can be achieved using various methods, such as seed-mediated growth,[13] control of reaction kinetics,[14,15] selective passivation by surfactants,[16,17] oriented attachment,[18] and sequential cation exchange processes[19,20]. By using these strategies, the morphology of nanocrystals has expanded to include nanorods[21], nanowires[22], nanoplates[23], nanocubes[24], multipods[25], and other faceted nanocrystals.[5,26] The development of colloidal synthetic methods to synthesize highly uniform nanomaterials with controllable sizes and shapes has opened a new era of understanding the unique physical properties of nanomaterials and hence has enabled a variety of applications of nanocrystals in science and technology.

1.2. Size and Shape Dependent Physical Properties of Nanocrystals

The size and shape of inorganic nanocrystals strongly influence the physical properties of nanomaterials. For instance, semiconducting quantum dots exhibit dramatic and distinct changes of their properties based on their size and shape. When a semiconducting material is formed into a nanocrystal which is smaller than the bulk exciton Bohr radius, the wavefunction of the electrons that are responsible for quantum effects greatly is impacted by the size and shape of the dot. Therefore, in this nanoscale regime, the electrical and optical properties of

semiconducting quantum dots depend strongly on their size and shape. In the case of CdSe nanocrystals, the onset of the absorption and emission shifts from a deep red (1.7eV) to green (2.4eV) as the cluster size decreases from 200 Å to 20 Å.[1,4] The shape is also an important parameter to tune the optical and electronic properties. One dimensional CdSe semiconducting nanorods exhibit optical anisotropy that causes polarized emission along the long axis.[27] In a two dimensional CdSe nanoplate, the electron and hole pairs are strongly confined in one dimension, which results in a high fluorescence quantum yield, a very narrow full width half-maximum(less than 40 meV), and an ultrafast fluorescence life time.[28]

Magnetic nanocrystals are widely explored for their magnetic resonance imaging (MRI) capabilities as a medical diagnostic tool. Cheon *et al.* demonstrated the nanoscale size-dependent magnetism and magnetic resonance properties of tightly size-controlled iron oxide nanocrystals,[29] which influenced the application of monodisperse iron oxide nanocrystals as *in-vivo* magnetic resonance signal enhancers.[30] Since the magnitude of magnetic spins in nanocrystals increases as the sizes of the nanocrystals increase, a larger mass magnetization value facilitates the spin-spin relaxation process of protons in the water molecules surrounding the nanocrystals. Therefore, transverse MR signal intensity increases with an increase in the sizes of the nanocrystals.

1.3. Lanthanide-Based Nanomaterials

A rare earth material is one of a set of the 15 lanthanides, scandium, and yttrium. A lanthanide element has a partially-filled f electron inner shell that is responsible for its characteristic optical and magnetic properties. The f orbitals are well shielded by the outer 5p and 6s orbitals, causing characteristic narrow-line atomic absorption and emission. The optical transition between f orbitals is a parity forbidden transition that results in very low molar extinction coefficients, typically < 3 $M^{-1}s^{-1}$.[31] In addition, atomic transitions of lanthanides show longer excited state lifetimes, typically in the microsecond to millisecond range.[32]

When two or more lanthanide elements are doped in a nanomaterial host, an efficient energy transfer can occur between the atomic levels of the doped lanthanide ions. The absorption and emission properties of the material can be controlled by using one or more different types of lanthanide dopants placed at a distance close enough that energy transfer can occur. With proper lanthanide selection, lanthanide ions show many interesting non-linear optical processes, such as two-photon upconversion and downconversion.[32,33] Upconversion refers to the process in which two or more low energy photons are absorbed and combined to produce one higher energy photon. Conversely, downconvesion is the process in which a high energy photon is absorbed and split into two lower energy photons. When energy transfer occurs between two dopants, one dopant is considered a sensitizer (donor) and absorbs light, and the other is called an

activator (acceptor) and contributes to the luminescence of the material. Due to these unique properties, coupled with the magnetic properties of rare earth elements, lanthanide-based nanomaterials are widely used in various applications such phosphors, lasers, magnets, and catalysts, and have formed an important platform for biomedical research.

The host material also plays an important role in engineering the luminescence properties of the optically active dopants. The host separates the dopants to prevent concentration quenching between optically active ions as well as the quenching of populated atomic levels by the outer molecules. This host material requires similar lattice parameters to the lanthanide dopants for efficient doping. Low phonon energies of the hosts are desirable to prevent non-radiative deactivation between f orbitals. In general, the non-radiative transition of lanthanide ions occurs via multi-phonon relaxation.[34,35] This process happens by simultaneous creation of several phonons which bridge the energy gap between f orbitals. The multi-phonon relaxation rate constant (k) across an energy gap is described as,

$$k = C exp(\frac{-\beta \Delta E}{\hbar \nu_{max}})$$

where C and β are positive constants of the material characteristics, ΔE is the energy gap between f-f states, and $\hbar \nu_{max}$ is the highest energy vibrational mode of the host lattice.[36] This suggests that the multi-phonon relaxation rate

decreases when a host with lower phonon energy is used. The highest energy longitudinal optical phonon mode is typically the stretching mode of anions whose frequency varies with the anion compositions.[35] Therefore, fluoride-type materials are ideal candidates due to their low lattice phonon energies, typically less than 500 cm^{-1}, and high chemical stabilities.[37]

Among the various types of hosts, $NaYF_4$ and $NaGdF_4$ are known as the most efficient materials for light emission, including upconversion, and are widely studied.[38] These materials form two different polymorphs, which are the kinetically stable cubic (α)-phase and the thermodynamically stable hexagonal (β)-phase. The hexagonal phase exhibits intense luminescence, including two-photon upconversion, that is about an order of magnitude more intense than luminescence produced by the cubic phase.[38] The crystal structures affect the emission intensity due to the different local crystal field around the optically active dopants tailored by the different symmetry of the hosts. Electronic transitions between *f* orbitals are forbidden due to quantum mechanical selection rules. Hosts with low crystal symmetry increase the possibility to mix a small amount of opposite-parity wavefunction into the 4f-states, resulting in some enhancement of the radiative relaxation from populated *f*-orbitals.[37,39] The high luminescence efficiency of the hexagonal phase may be attributed to the lower symmetry of optically active dopants. In addition, the lattice phonon frequency of hexagonal phase materials is much smaller than that of cubic phase materials, which prevents non-radiative deactivation.[37]

In order to understand the physical properties of lanthanide-doped nanomaterials, it is important to develop synthetic methods to precisely tune size, shape, composition, and crystal structure on a nanometer scales. There are several methods to synthesize lanthanide-based nanomaterials, for example, hydrothermal methods, sol-gel reactions, combustion syntheses, and co-precipitation methods.[39] Among them, one of the most commonly used methods is high temperature thermal decomposition with metal precursors that produce highly uniform lanthanide-based nanomaterials with controllable sizes and shapes. This method was developed by Yan *et. al.*, to synthesize triangular LaF_3 nanoplates.[40] They introduced trifluoroacetate salts as single source metal precursors and heated them up to the 280^oC in the presence of oleic acid and octadecene to induce the nucleation and growth of nanocrystals. Lanthanum trifluoroacetate salts thermally decompose as suggested in Scheme 1.1.,[41] forming highly uniform triangular LaF_3 nanoplates. The non-injection, heating-up approach using the trifluoroacetate salts has been applied to synthesize many different types of fluoride-based lanthanide nanocrystals such as $NaYF_4$[42,43], $NaGdF_4$[44], $LiYF_4$[45], and YF_3[46]. Since the luminescence properties highly depend on their composition and crystal structure, it is important to develop chemistry that enables the production of phase-pure inorganic nanomaterials. Therefore, the investigation of growth mechanisms to understand the evolution of the size, shape, and crystal structure that occurs during the reaction is essential.

$$Ln(CF_3COO)_3 \cdot 3H_2O \longrightarrow Ln(CF_3COO)_3 \longrightarrow LnF_3 + (CF_3CO)_2O + CO_2 + CO$$

$$(CF_3CO)_2O \longrightarrow CF_3COF + COF_2 + CO$$
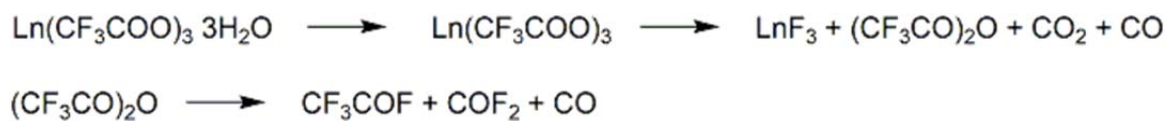
Scheme 1.1. Thermal decomposition reaction of rare earth trifluoroacetate salts.
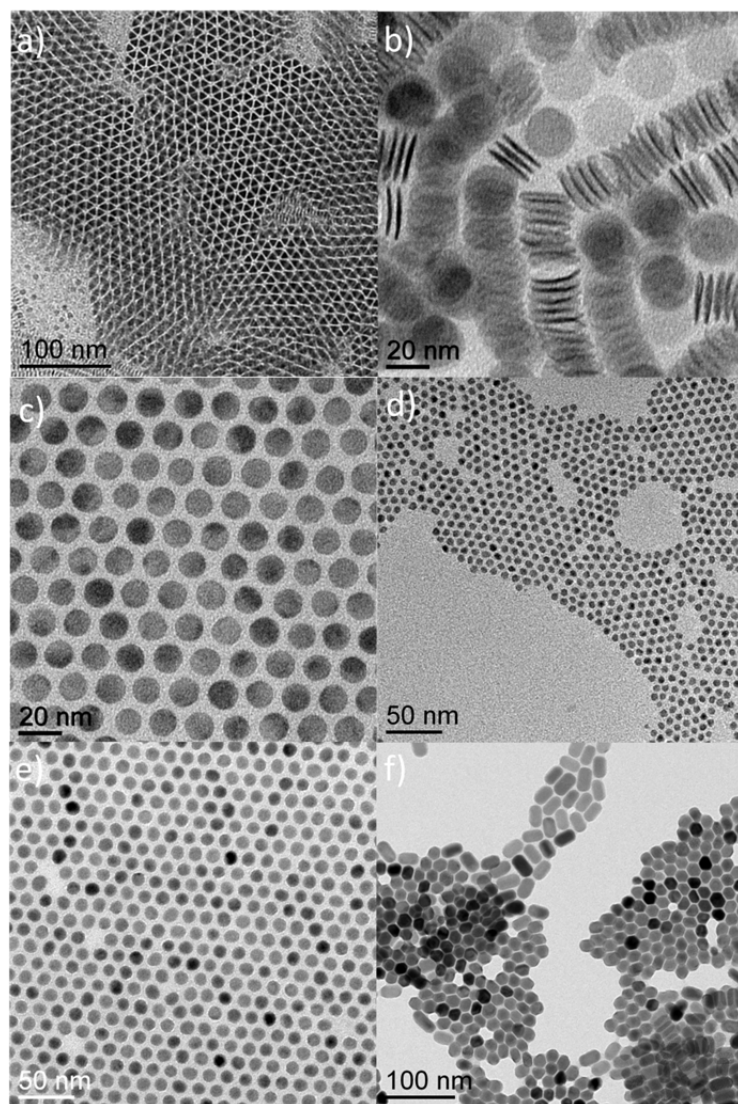
Figure 1.2. TEM images of lanthanide based nanocrystals. a) triangular and b) spherical LaF$_3$ nanoplates, c) EuF$_3$ nanodisks, d) cubic(α)-phase NaGdF$_4$ nanospheres, e) hexagonal(β)-phase NaGdF$_4$ nanospheres and f) nanorods.

Upconversion luminescence, which is a non-linear process achieved by customizing the composition of nanocrystals, provides a unique optical modality for a variety of applications including bioimaging, sensing, and therapy.[47] The upconversion process consists of the sequential absorption of low energy photons followed by the emission of a higher energy photon as anti-Stokes emission. The upconverter is composed of two or more lanthanide dopants that act as sensitizers and activators and the host material. Erbium(Er^{3+}), thulium(Tm^{3+}), and holmium(Ho^{3+}) have been used as activators that emit light under low energy excitation, and ytterbium (Yb^{3+}) is the most commonly used element as the sensitizer for the upconversion process. Yb^{3+} has a relatively large absorption cross-section and the energy gap between the $^2F_{7/2}$ ground state and $^2F_{5/2}$ excited state of ytterbium matches well with the transition energy between the atomic levels of Er^{3+} or Tm^{3+}.[39] Therefore, the resonance energy transfer from the sensitizer to the activators can be facilitated, resulting in the enhancement of the upconversion efficiency. The absorption wavelength of ytterbium is around 980nm, which is located at the transparent near-IR window in biological tissues. Therefore, upconversion luminescence offers higher penetration depth in the biological system, enabling efficient *in-vivo* imaging capability. In addition, large anti-Stoke shifts minimize the autofluorescence from the background, which helps to increase the signal-to-noise ratio. With a careful choice of host materials, upconverting nanocrystals exhibit remarkable photostability without photo-bleaching and blinking.[48]

1.4. Lanthanide-Based Nanocrystals for Biomedical Application.

Lanthanide-based inorganic nanomaterials are a promising platform for biomedical research, such as medical diagnostics and clinical therapy. Among the lanthanides, gadolinium is particularly interesting due to its unique paramagnetic properties and its potential applications in MRI contrast agents.[49] MRI is a routine diagnostic tool in modern clinical medicine. It is a non-invasive and real time imaging method that provides excellent spatial resolution and anatomical information with unlimited tissue penetration. The MRI signal is generated by the transverse relaxation of the net magnetization of protons in water molecules. Gd^{3+}-based agents shorten the relaxation time of nearby water protons to create the contrast in MR signals.[49] Although many different types of Gd^{3+} complexes and clusters have been explored to increase sensitivity and spatial resolution, they still have a couple of drawbacks.[50] Small molecule Gd^{3+} complexes show a very short body circulation time due to the rapid excretion through urine, which poses as a problem in long term tracking. A low local concentration of Gd ions causes relatively low contrast due to its small relaxivity. Gd^{3+} complexes suffer from the risk of dissociation of the complexes into free ligands and Gd ions, which could cause an acute toxic effect from the free gadolinium, such as nephrogenic system fibrosis. In addition, the functionalization of the Gd^{3+} small molecule agent with the specific targeting agents is not trivial, which limits the utilization of this type of contrast agents for site-selective imaging.

Gd-based nanocrystals have the potential to overcome the many disadvantages of Gd-complexes.[51] The nanocrystal is composed of a large number of Gd ions that increase the local concentration of Gd at the region of interest. Due to the large surface-to-volume ratio of the nanocrystals, it is relatively easy to functionalize the contrast agents with targeting molecules for site selective imaging. The circulation time and clearance can be controlled by changing the size and shape of the nanocrystals. In addition, doping Gd-based nanocrystals with optically active lanthanide elements or radio-lanthanides can be conducted to easily customize their multimodal imaging capacity. Thanks to the progress of synthesis strategies for highly uniform nanocrystals, many different types of Gd-based nanocrystals, such as $NaGdF_4$, GdF_3, $GdPO_4$, and Gd_2O_3, have been explored for MRI applications and studied to understand the effect of nanocrystal morphology on MR relaxivity.[52] For example, van Veggel *et. al* reported size dependent MR contrast enhancement of hexagonal phase $NaGdF_4$.[44] They synthesized nanocrystals with various sizes from 2.5 nm to 8.0 nm and investigated T_1 longitudinal relaxivity at 1.5 Tesla. They observed that ionic relaxivity increases as the size of the nanocrystals decreases, which may be attributed to the enhancement of the surface-to-volume ratio. However, they also argued that the surface ions on a larger nanocrystal affect the relaxivity more strongly than the ions on a smaller one due to the increase of the tumbling time (τ_R) in larger nanocrystals which can counteract the effect of the surface-to-volume ratio. These results reveal that both the size and the shape dramatically

influence the MR relaxivity for MRI imaging. However, systematic studies to understand how size, shape, and composition of highly monodisperse Gd-type nanocrystals influences the MR relexivities have not been sufficiently performed.

The properties of nanocrystals may be further manipulated through controlled aggregation or self-assembly of individual nanocrystals *in vivo*.[53-55] Weissleder and coworkers developed magnetic nanosensors from DNA-hybridized magnetic nanocrystals.[56] Controlled hybridization by adding specific molecules that can induce the self-assembly of magnetic nanocrystals works as magnetic relaxation switching in MRI, resulting in an increase of spin-spin relaxation time of protons in the surroundings due to the enhancement of the magnetic properties of assembled clusters. This enables the detection of specific and selective molecular interactions that can induce the aggregation of DNA-functionalized magnetic nanoparticles. These results reveal that understanding the processes of the self-assembly, which are governed by nanocrystal size, shape, composition, and surface functionality, is important for establishing the design rules to engineer the properties of superstructures.

1.5. Nanocrystal Shape-Effect on Nano-Bio Interactions.

While early studies focused on understanding of how the physical properties of nanocrystals are modified by particle size and shape, evidence suggests that the size and shape of nanocrystals can strongly influence physiological interactions in biological systems, such as effects on cellular binding,

internalization, and toxicity.[57-59] The effect of nanocrystal size on enhanced permeability and retention (EPR) and *in-vivo* blood circulation time is well documented in the literature.[57,58,60] More recently, the nanocrystal shape was also shown to influence cellular internalization and nanoparticle-cell interactions.[61-66] For example, DeSimone and co-workers reported that rod-like high-aspect-ratio hydrogels (several hundred nanometers in size) were internalized faster than more symmetric cylindrical particles even though both particles are almost the same in volume. Further studies revealed that, even among the anisotropic shapes, disk-shaped hydrogel nanoparticles more preferentially accumulate within tumor vasculature than rod-shaped nanoparticles and thus increase the sensitivity of tumor detection.[67] This result indicates the importance of nanocrystal shape on biological interactions and suggests that the transport mechanism and kinetics of nanocrystal-based tracers or delivery carriers in biomedical applications can be engineered by the size and shape control of nanomaterials

In addition, in order to utilize nanocrystal-based tracers for bio-applications, environmental and health aspects such as toxicity should be clearly understood. The size and shape dependent toxicity of nanocrystals has been widely studied. For example, Zink *et. al* reported that increasing the aspect ratio of nanomaterials, such as in cerium oxide nanowires, results in increased cytotoxicity acting as fiber-like substances that can damages lysosomes.[68] Thus, including tracking/imaging elements into nanocrystals with different size, shape, and functionality can also allow for the unambiguous exploration of

environmental and health effects of engineered nanomaterials.[69,70] For the precise studies of the size and shape effects of nanocrystals on transport mechanisms and cell interactions, size monodispersity and shape uniformity are essential because it allows for the accurate analysis of biodistributions without the confounding effect of size and shape-dependent clearance. Therefore, it is prerequisite to develop methods to tune the morphology of highly uniform nanocrystals that can be directly applied for this type of study.

1.6. Nanocrystal Superlattices with Anisotropic Nanocrystals

The self-assembly of small building blocks such as molecules, and nanocrystals enables the integration of small building blocks into macroscopic superstructures through a bottom-up approach.[71,72] In nature, this process frequently occurs to construct large-scale biological structures exhibiting collective functions beyond the individual building blocks. For example, lipids, which are a group of naturally existing amphiphilic small molecules, are self-assembled into lipid bilayer membranes by spontaneous and non-covalent interactions. Membranes are essential structural building blocks for living creatures and further assemble to form superstructures such as vesicles, micelles, and liposomes. Much larger and more complex superstructures are also constructed by these self-assembly approaches. For instance, the tobacco mosaic virus is a helical virus particle which is composed of 2130 identical sub-units.[73] In the physiological conditions, the protein sub-units form as disk-shaped

small clusters. In the presence of RNA, small subunits are self-assembled *via* non-covalent interactions to construct rod-like superstructures 300 nm in length and 18 nm in diameter. Inorganic materials also self-assemble into arrays to form ordered superlattices in nature. A natural opal is composed of silica particles which are self-assembled into close-packed arrays. Although individual nanoparticles are colorless, their assembled structure exhibits internal colors due to diffraction caused by grating created by the stacked planes of self-assembled nanoparticles.

Artificially synthesized colloidal nanocrystals are promising building blocks for the formation of novel functional metamaterials *via* self-assembly. Due to the recent development of colloidal chemistry, the size, shape, chemical compositions, and surface chemistry of nanomaterials are able to be systematically tuned, which enables the physical properties of highly uniform nanocrystals to be precisely controlled.[5] In addition, the properties of superlattices can be tailored by the careful selection of the type of building blocks among the nanocrystals exhibiting plasmonic, magnetic, semiconducting, and dielectric properties. Figure 1.3 shows TEM images of single component superlattices composed of different types of nanocrystals, such as metal (Figure a, Au nanocrysals), dielectric nanocrystals (Figure b, CaF_2), and semiconductors (Figure c and d, Indium-doped CdO). The interactions between nanocrystals in the superlattices gives rise to novel collective properties of artificial solids from a set of building blocks, which is distinct from the properties of individual

nanoparticles. Control over single and binary nanocrystal superlattice structures is exerted through a variety of factors contributing to an emerging set of design rules which incorporate the type of nanocrystal,[74,75] particle size and relative size ratio,[75,76] and self-assembly conditions.[77,78]
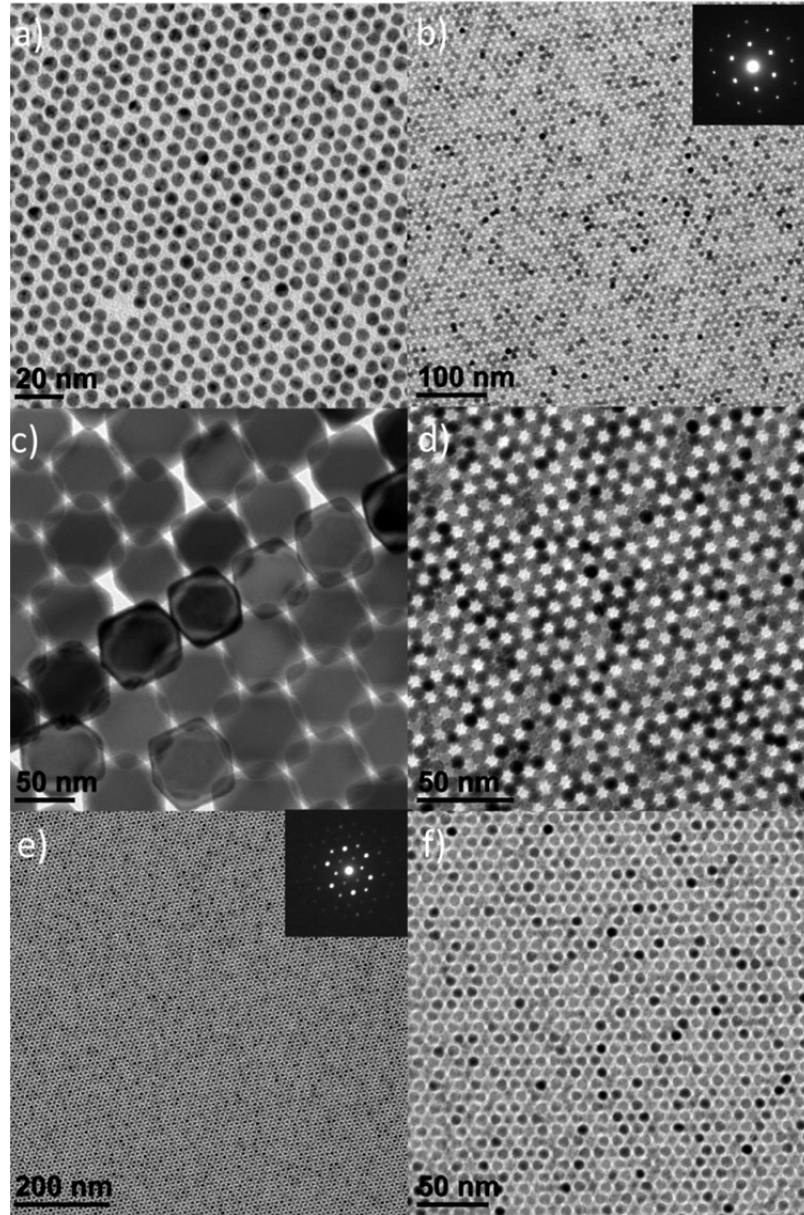
Figure 1.3 TEM images of single component superlattices of a) Au (metal), b) CaF$_2$ (dielectric), c) octahedral and d) spherical indium-doped CdO (semiconductors). e) and f) Long range [001] projection of an MgZn$_2$-type binary nanocrystal superlattices of 7.5 nm indium-doped Cd nanocrystals and 5.0 nm PbSe nanocrystals. The inset shows small-angle electron diffraction pattern of the binary superlattices.

Among the vast collection of nanocrystal building blocks, anisotropic nanocrystals offer a new design criterion for tuning assemblies, allowing for the formation of liquid crystalline phases with differing orientational and positional order.[79,80] These non-spherical building blocks provide more extended phase diagrams and packing arrangements, which is predicted by theoretical simulation,[81-87] and has been demonstrated experimentally through the use of anisotropic building blocks, in which complex shapes are organized into ordered superlattices.[88-96] Nanorods are well-known anisotropic building blocks which form oriented liquid crystalline superlattices, previously fabricated by drying-mediated self-assembly,[97] electric-field-assisted assembly,[98] depletion attraction,[99] and the Langmuir-Blodgett technique.[100] Liquid crystalline assemblies of nanoplates have also been demonstrated.[40,85,101-106] Cao *et al.* demonstrated highly ordered assemblies of gadolinium oxide (Gd_2O_3) square nanoplates.[101]

Liquid crystalline superlattices offer interesting properties due to non-spherical building blocks as well as the anisotropic structure of superlattices. Talapin *et al.* reported that the self-organization of CdSe and CdSe/CdS nanorods into nematic, smectic, and crystalline solids.[107] Liquid crystalline superlattices of CdSe nanorods are grown *via* controlled destabilization of CdSe nanorods in solution by slow diffusion of a non-solvent. It is observed that anisotropic superlattices display strong optical anisotropy of the nanorods and characteristic birefringence due to the specific texture of the nanorod assembly.

The macroscopic orientation of the semiconducting nanorods in self-assembled structures have also influenced their electrical properties. Sirringhaus *et al.* reported that self-assembled ZnO nanorods, which are preferentially oriented along in-plane directions on the substrates, shows significant improvement of field effect transistors device performance, indicating higher charge transport than devices in which ZnO nanorods are isotropically aggregated.[108] This reveals that the orientation and orders of the anisotropic building blocks in self-assembled superlattices does strongly influence the collective behaviors of artificial solids. Therefore, it is important to develop methods to systematically control the macroscopic orientation and positional orders of anisotropic building blocks in self-assembly in order to engineer the properties of superlattices.

1.7. Thesis Overview

The goal of this thesis is to develop novel chemistry for synthesizing highly uniform nanocrystals with controllable size, shape, and chemical compositions, investigate the reaction mechanism to understand nanocrystal growth, characterize the structure and properties of synthesized nanocrystals, and develop designable methods to order self-assembled anisotropic building blocks into structured arrays to create complex nanocrystal solids

In Chapter 2, I demonstrate the shape controlled synthesis of lanthanide based nanomaterials with the addition of alkali metal salts. We observed that

nanocrystal shapes are dramatically influenced by the type of salts used for the reaction. I characterize their optical and magnetic properties to investigate the potential biomedical applications of these materials. In Chapter 3, I synthesize the radiolabelled nanomaterials with controlled size and shape using the synthesis method developed in Chapter 2. In Chapter 4, I will explain the shape-directed self-assembly of anisotropic nanocrystals and demonstrated that complex anisotropic superstructures are fabricated with single and binary components by a careful design of anisotropic building blocks. In Chapter 5, I extend the concept of the heating up method to synthesize transition metal oxides nanomaterials *via* non-hydrolytic reaction between metal halides and primary alcohols. In Chapter 6, I investigate that vanadium oxide (VO_x) colloidal nanocrystals can be utilized as the precursors to synthesize thermochromic VO_2, which is an important building block for energy research, optics, and electronic devices.

CHAPTER 2. SHAPE-CONTROLLED SYNTHESIS OF GADOLINIUM-BASED NANOCRYSTALS

2.1. Introduction

Establishing methods to synthesize nanocrystals with well-defined size and shape is crucial, as the size, shape, surface, and crystal structure all strongly influence the properties of nanocrystals.[2,109,110] Synthesis of nanocrystals with tailored morphology allows for correlation of the optical, magnetic, and electronic properties with the nanocrystal size and shape. This insight guides the design of nanocrystals optimized for various applications.[29,111,112] Shape control of nanocrystals is achieved using various methods, including seed-mediated growth,[13] control of reaction kinetics,[14,15] selective passivation by surfactants,[16,17] oriented attachment,[18] and sequential cation exchange processes[19,20]. Using these strategies, the morphology of nanocrystals has expanded to include nanorods[21], nanowires[22], nanoplates[23], nanocubes[24], multipods[25], and other faceted nanocrystals.[5,26]

In biomedical research and clinical medicine, nanocrystals play an increasingly important role as imaging agents and tracers.[113,114] Nanocrystal-based imaging probes can offer enhanced sensitivity and spatial resolution through incorporation of two or more imaging modalities into a single nanocrystal.[12,65,115,116] The properties of nanocrystals may be further manipulated

through controlled aggregation or self-assembly of individual nanocrystals *in vivo*.[53-55] Furthermore, the high surface area of nanocrystals facilitates their surface modification with targeting reagents providing enhanced detection sensitivity and selective targeting of therapeutic agents.[117,118] While early studies focused on understanding how the physical properties of nanocrystals are modified by particle size and shape, evidence suggests that the size and shape of nanocrystals can also directly influence the interaction of nanocrystals with biological systems. The effect of nanocrystal size on enhanced permeability and retention (EPR) and *in-vivo* blood circulation time is well documented in the literature.[57,58,60] More recently, the nanocrystal shape was also shown to influence cellular internalization and nanoparticle-cell interaction. For example, disc-shaped nanocrystals preferentially accumulate within tumor vasculature and increase the sensitivity of tumor detection,[67] which indicates the importance of nanocrystal shape on biological interactions. Monodispersity is essential in this investigation because it allows for accurate analysis of biodistributions without the confounding effect of size-dependent clearance. Therefore, it is prerequisite to develop methods to tune the morphology of highly uniform nanocrystals that can be directly applied as imaging agents.

Lanthanide-based nanocrystals are promising candidates for nano-medicine applications.[39,119-123] A rich morphological diversity of lanthanide-based nanocrystals exists that may be tailored by precisely controlling reaction conditions.[124-128] Lanthanide ions have free f-electrons which are responsible for

their unique magnetic and optical properties and allow for the design of customized nanocrystals by simply incorporating multiple lanthanide ions into the nanocrystals. The optical transition between *f* orbitals is a parity forbidden transition, resulting in long excited state lifetimes (> 1 μs). This facilitates energy transfer between atomic levels in lanthanide dopants, which can result in non-linear optical properties such as near-IR to visible two-photon upconversion.[38,129-131] In addition, lanthanide-based nanocrystals act as scintillating materials due to their high atomic number, providing an additional optical modality under high-energy radiation such as X-ray.[132-134] The paramagnetic behavior of several lanthanide elements, including gadolinium (Gd), enables the use of lanthanide-based materials as magnetic resonance imaging (MRI) contrast agents.

In this section, we introduce the synthetic method to control the shape of highly uniform lanthanide-based nanocrystals. With an addition of alkali metal salts, the size and morphologies of nanocrystals can be tightly controlled by the careful control of reaction parameters. The structures are precisely characterized with electron microscopy and X-ray based measurement techniques coupled with X-ray simulations. Then, we measure their optical and magnetic properties. The expression of these properties suggests that these shape-controlled nanomaterials can be utilized as promising platforms for the various biomedical applications. In chapter 2.2, we discuss the shape-controlled synthesis of gadolinium fluoride-type nanocrystals. In chapter 2.3, we extend the type of host

to oxide-based nanocrystals and demonstrate that a wide range of structural diversity can be designed by this salt-mediated synthesis.

2.2. Shape-Controlled Synthesis and Characterization of Gadolinium Fluoride-type Nanocrystals

Scheme 2.1 is the synthetic method for $NaGdF_4$ nanocrystals doped with lanthanides. Gadolinium trifluoroacetate is used as the metal precursor, which is prepared by dissolving gadolinium oxide in a trifluoroacetic acid and water mixture (50:50 vol%) under refluxing conditions. Then, the precursors, sodium fluoride, oleic acid, and 1-octadecene, are added into a 125ml three neck flask and degassed at $125^{\circ}C$ for 1hr. The mixture is then heated to $290^{\circ}C$ and kept at this temperature for 5 hours. The product is precipitated by adding excess ethanol and collected by centrifugation.

$$Gd_2O_3 \ + \ CF_3COOH \longrightarrow Gd(CF_3COO)_3 \, xH_2O \xrightarrow[\substack{OA, \ ODE \\ 290^{\circ}C, \ 5hr}]{NaF} \beta\text{-phase } NaGdF_4$$
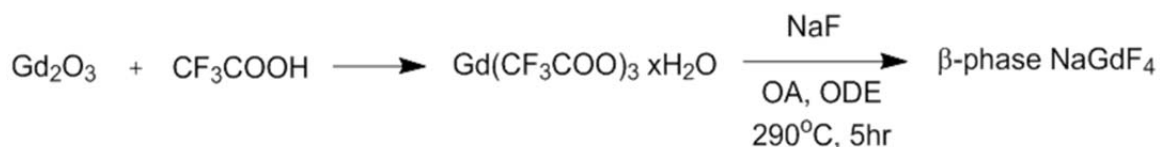
Scheme 2.1. Synthesis of hexagonal(β)-phase $NaGdF_4$
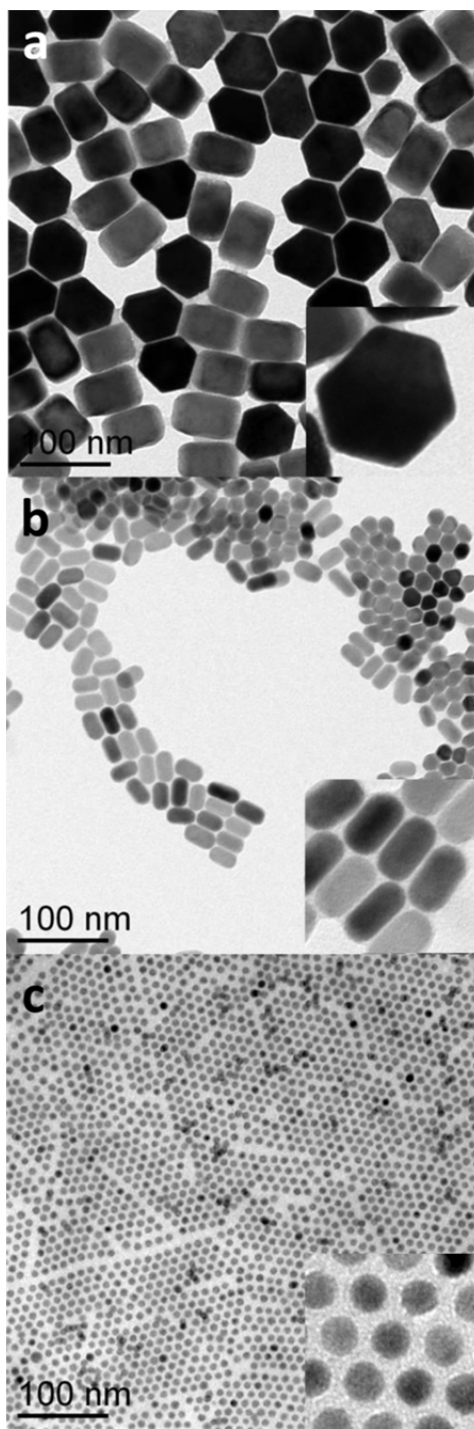
Figure 2.1. TEM images of hexagonal phase NaGdF$_4$ nanoparticles synthesized by varying the molar ratio of NaF to Gd^{3+} a) 1.3 : 1, b) 2.5 : 1, and c) 5 : 1.

The morphology of the nanocrystals is tuned by changing the ratio of NaF to Gd^{3+} in the reaction. Figure 2.1 shows the TEM images of β-NaGdF$_4$ nanocrystals synthesized with different NaF to Gd^{3+} molar ratios. At low NaF to Gd^{3+} ratios, large hexagonal plates of β-NaGdF$_4$ are obtained with edge-to-edge distances of 64nm and an average thickness of 44 nm (Figure 2.1a). With increasing NaF to Gd^{3+} ratios, the morphology of β-NaGdF$_4$ changes to nanorods with a length of 32nm and a width of 5nm. At even higher ratios, monodisperse spheres are synthesized as the final product with 10 - 13nm in average size. The size, shape, and monodispersity of nanocrystals are maintained even after the addition of different types of dopants, up to 20% molar ratio. However, the NaF to Gd^{3+} ratio to synthesize uniform spherical nanocrystals increases with dopant concentration, especially for the heavy lanthanide elements.(Figure 2.2) When the NaF to Gd^{3+} ratio is further increased, the average size of the particles decreases but the overall product becomes less monodisperse.
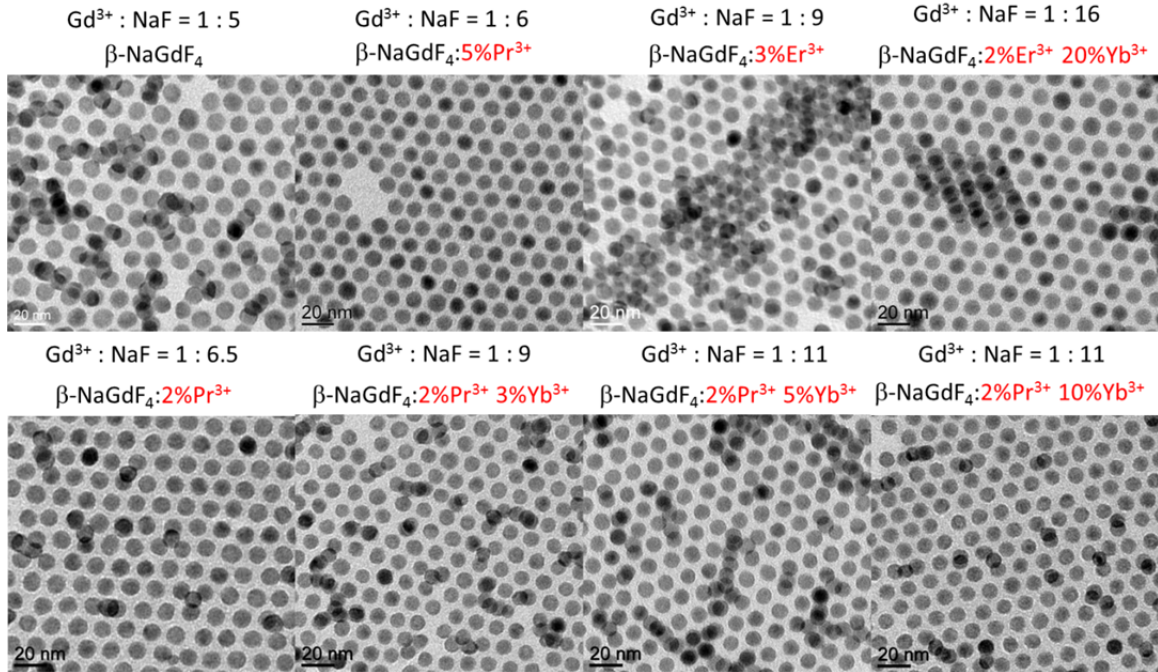
Figure 2.2. TEM images of spherical β-NaGdF$_4$ nanocrystals synthesized with different dopant concentrations and optimum NaF to Gd^{3+} ratio to obtain the spherical morphology

NaGdF$_4$ particles have two stable crystal structures at room temperature, cubic phase(α) and hexagonal phase(β). It is known that the cubic phase is kinetically stable and the hexagonal phase is thermodynamically stable structure. During the reaction, we observe the phase transformation, which occurs from the kinetically stable cubic phase to thermodynamically stable hexagonal phase. In order to monitor the growth mechanism, aliquots are taken during the reaction and analyzed by TEM and powder X-ray diffraction (PXRD). Figure 2.3 shows the TEM images of the nanocrystals and PXRD results corresponding to TEM

images. After a 1hr reaction time at 290°C, spherical nanocrystals smaller than 5nm in diameter are observed. The XRD data shows that the crystal structure at this stage is the kinetically stable α-phase. After continued growth at the same temperature for additional hours, the cubic-to-hexagonal phase transformation occurs, as indicated in corresponding XRD patterns, and the morphology of the nanocrystals changes from small α-phase nanospheres to β-phase nanorods with bimodal distribution, which is corroborated by PXRD patterns (Figure 2.3b, e). With extended reaction times, a decrease in the fraction of small particles in the TEM images is observed and the relative amount of α-phase nanospheres is also reduced, as monitored in PXRD measurements. After 5 hours, only nanorods are observed in the TEM image and the XRD pattern indicates that the nanorods are purely β-phase. This result suggests that the kinetically stable α-NaGdF$_4$ nanocrystals are formed in the early stages of the reaction and transformed into thermodynamically stable β-phase NaGdF$_4$ with sufficient thermal energy. This is further supported by the fact that a higher reaction temperature accelerates α to β phase transformation. At 300° C, nanorods are grown through the same phase transformation pathway, but pure β-phase nanorods are obtained within 2 hours.
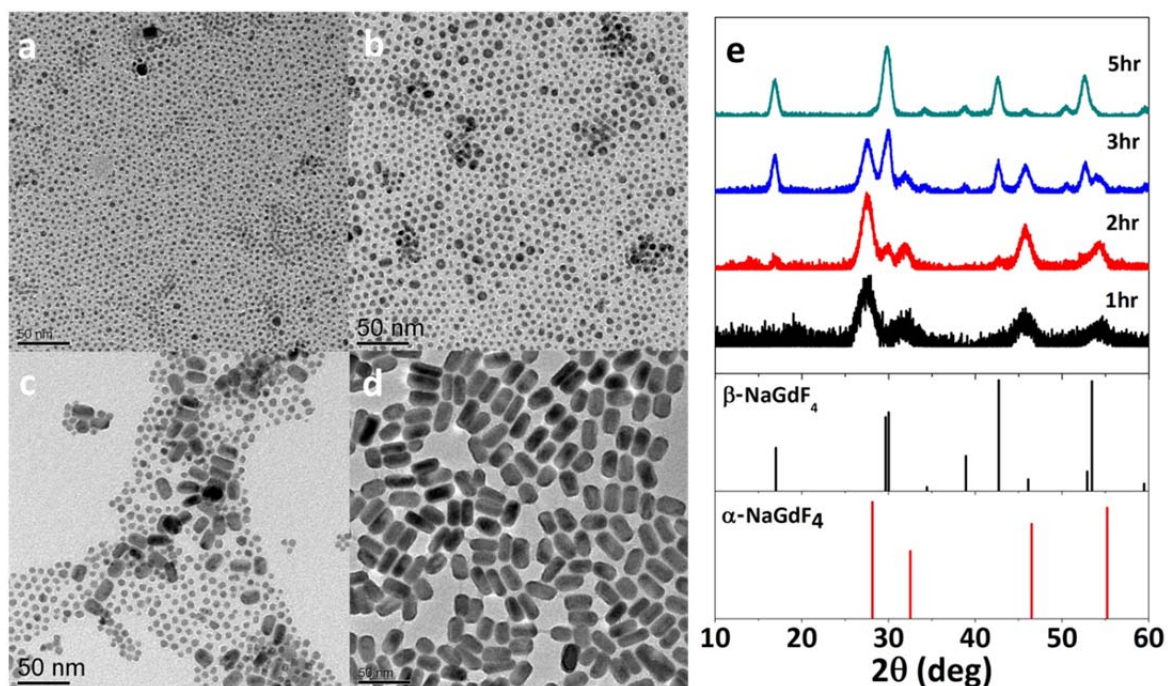
Figure 2.3. Reaction time dependent shape and phase transformation. TEM images of nanocrystals synthesized at 290°C for a) 1 hour, b) 2 hours, c) 3 hours, and d) 5 hours. e) PXRD patterns of NaGdF$_4$ nanocrystals at different reaction times.

Figure 2.4 shows the TEM images of NaGdF$_4$ nanocrystals synthesized with different NaF to Gd^{3+} ratios. At low NaF to Gd^{3+} ratios, β-NaGdF$_4$ hexagonal nanoplates approximately 35 nm in size are obtained after reacting for 5 hours. The α to β phase transformation is still observed during the nanocrystal growth. α-phase nanocrystals are no longer present after 5 hours. By increasing the amount of NaF, it is observed that the α to β phase transformation is completed at a much earlier stage, typically after a 4 hour reaction time, to form pure β-

phase nanorods. By increasing the ratio of NaF to Gd^{3+} even further, the α to β phase transformation is completed within 2 hours forming β-phase spherical nanocrystals with an average diameter of 10 nm. This trend indicates that the increased presence of NaF affects not only the final morphology of nanocrystals, but also the kinetics of the phase transformation. Under these reaction conditions, nanocrystals do not form without the addition of NaF even at elevated reaction temperatures, up to 320°C, revealing that NaF is involved in the initiation of the precursor decomposition required to generate reactive nuclei. When the relative amount of NaF decreases, the initiation rate could be reduced, resulting in a decrease of the number of nuclei formed in the reaction mixture. This indicates that the relatively large population of precursors which could be grown on the nuclei remains in the reaction mixture. Therefore, during the rest of the reaction, larger sizes of nanocrystals could be formed from relatively large amounts of precursors and a small number of nuclei. On the other hand, with the large amount of NaF added, more nuclei could be formed due to the fast initiation of the precursors yielding smaller amounts of precursors available for the growth. Therefore, a larger number of smaller sized nanocrystals are synthesized as final products. A similar mechanistic study is reported in the literature, wherein higher reaction temperatures result in faster thermal decomposition, yielding more initial nuclei and thus a larger number of smaller sized crystallites.[135]
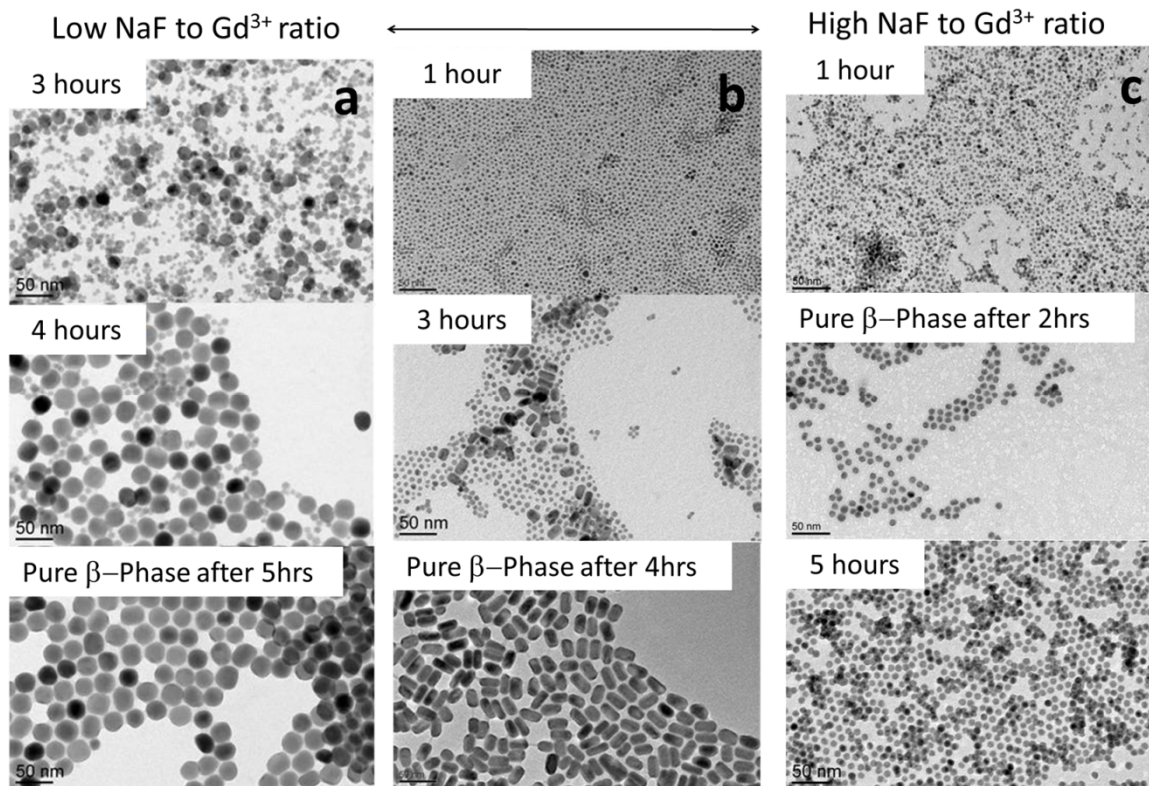
Figure 2.4. TEM images of β-NaGdF$_4$ nanocrystals synthesized with varying NaF to Gd^{3+} ratios and their time dependent shape transformation.

Upconverting β-phase NaGdF$_4$ are synthesized by doping with erbium (Er^{3+}) and ytterbium (Yb^{3+}) co-dopants. Two-photon upconverting nanophosphors convert two low energy photons into one visible photon. Near-IR photons show superb penetration into biological media, suggesting the possibility of utilizing these nanocrystals as efficient energy converters and optical imaging probes for *in-vivo* applications. In order to enhance the upconversion luminescence efficiency, upconverting nanophosphors are overcoated with additional layers of host materials, preventing the fluorescence quenching by defects on the surface

of nanocrystals or by solvent molecules. After synthesizing Er^{3+} and Yb^{3+} co-doped β-phase $NaGdF_4$, these core nanocrystals can be over-coated simply by adding Gd precursors into the crude reaction mixture of core nanocrystals, followed by additional heating at 290^oC for 2 hours. Figure 2.5a and 2.5b show the TEM images of Er^{3+}, Yb^{3+} co-doped β-phase $NaGdF_4$ before and after overcoating. It is observed that the spherical morphology of nanocrystals is maintained after shell formation. To confirm the size and size distribution of nanocrystals, small angle X-ray scattering (SAXS) experiments are conducted. In SAXS, scattering arises from the electron density difference between the nanoscale object and the surrounding medium. The intensity of the scattering radiation is expressed as, $I(q) = |f(q)|^2 \cdot S(q)$ where $f(q)$ is the form factor which depends on the size and shape of the particle and $S(q)$ is the structure factor which gives the correlation between particles.[136] Formulation of $f(q)$ using the standard spherical model with the distribution function accounting for the size dispersion and equating $S(q) = 1$ for a dilute assumption scattering profile can be fitted to obtain the average size and distribution of the tested nanocrystals.[137,138] The X-ray fittings indicate that the core nanocrystals are roughly 13.4 ± 1.2 nm in diameter and the core-shell nanocrystals are 16.9 ± 1.4 nm, in good agreement with statistical analysis from TEM images.(Figure 2.5c and d) Core-shell upconverting nanocrystals show stable colloidal dispersion in nonpolar solution without any noticeable aggregation and display green phosphorescence under 980 nm excitation (Figure 2.5e).
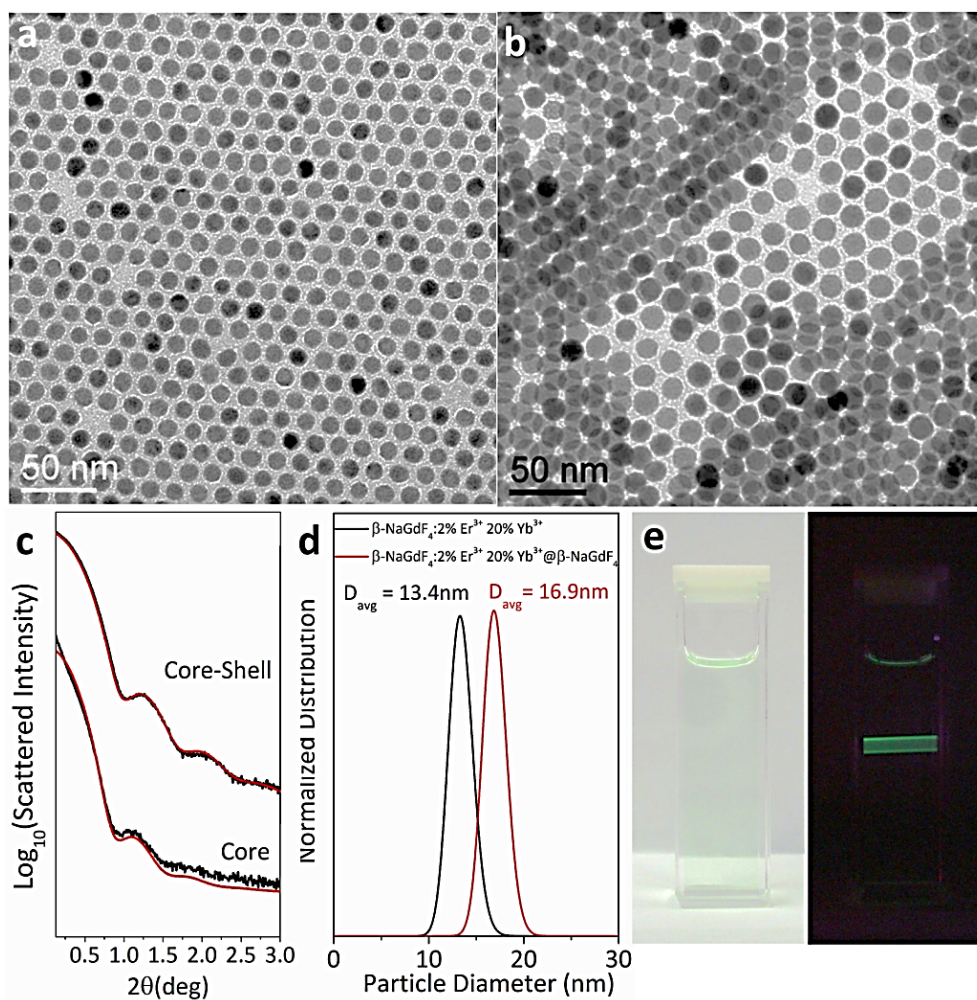
Figure 2.5. TEM images of a) β-NaGdF$_4$: 2%Er^{3+} 20%Yb^{3+} core and b) β-NaGdF$_4$:2%Er^{3+} 20%Yb^{3+}/β-NaGdF$_4$ core-shell structure. c) SAXS patterns and d) average size and size distribution of core and core-shell nanocrystals. e) Photograph of upconversion luminescence of β-NaGdF$_4$:2%Er^{3+} 20%Yb^{3+}/β-NaGdF$_4$ core-shell nanocrystals under 980nm excitation.

With an addition of lithium fluoride (LiF) instead of NaF, gadolinium trifluoride (GdF$_3$) nanocrystals are obtained as a final product with 2-D plate morphology. The size and shape are readily tuned through the modification of reaction parameters, such as the ratio of LiF to Gd^{3+}, reaction time, and reaction temperature. We observed that the size of nanoplates increases by increasing the amount of LiF in the reaction mixture, extending the reaction time, and increasing the reaction temperature. Figure 2.6 shows TEM images of GdF$_3$ nanoplates synthesized with different reaction conditions. The length and width of the nanoparticles vary over a wide range, typically from 10 to 50nm while maintaining the high uniformity, but their thickness only varies between 1.5 nm to 3nm.
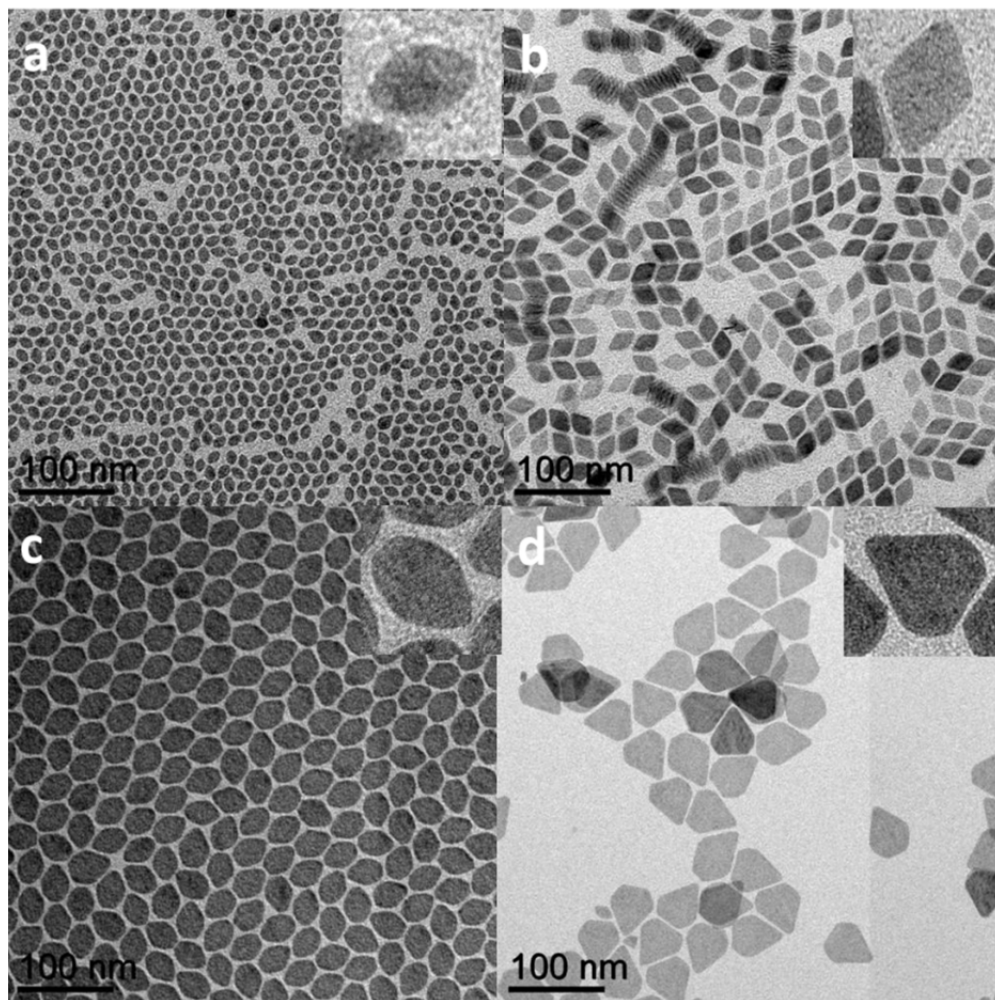
Figure 2.6. TEM images of GdF$_3$ nanoparticles synthesized by changing reaction conditions. The insets represent high magnification images.

In colloidal systems, larger crystals with smaller surface-to-volume ratios are more energetically favorable than smaller crystals, resulting in the growth of larger particles at the expense of smaller ones. This phenomenon is referred to

as Ostwald ripening.[139] This is attributed to the fact that smaller particles possess higher interfacial energies because atoms on the surface are energetically less stable than atoms that are already well-ordered and packed inside the crystals. A similar phenomenon is observed during the growth and shape transformation of GdF_3 nanoplates. In order to investigate the shape evolution, aliquots are taken during the reaction and analyzed by TEM and PXRD. Figure 2.7 a-d represents TEM images of nanoplates taken at increasing time intervals at a 290°C reaction temperature. It is observed that ellipsoidal nanoplates are firstly formed after an hour with tip-to-tip distances of 10 nm (Figure 2.7a). After aging at the same temperature, the dissolution of small nanoplates is observed with the growth of large nanoplates, yielding a bimodal size distribution of nanoplates (Figure 2.7b). With extending the reaction time, the large nanoplates further grow to form a rhombic morphology with consecutive consumption of small nanoplates.(Figure 2.7c) After a 4 hour reaction, small ellipsoidal nanoplates are completely replaced after ripening by nearly monodisperse rhombic nanoplates.
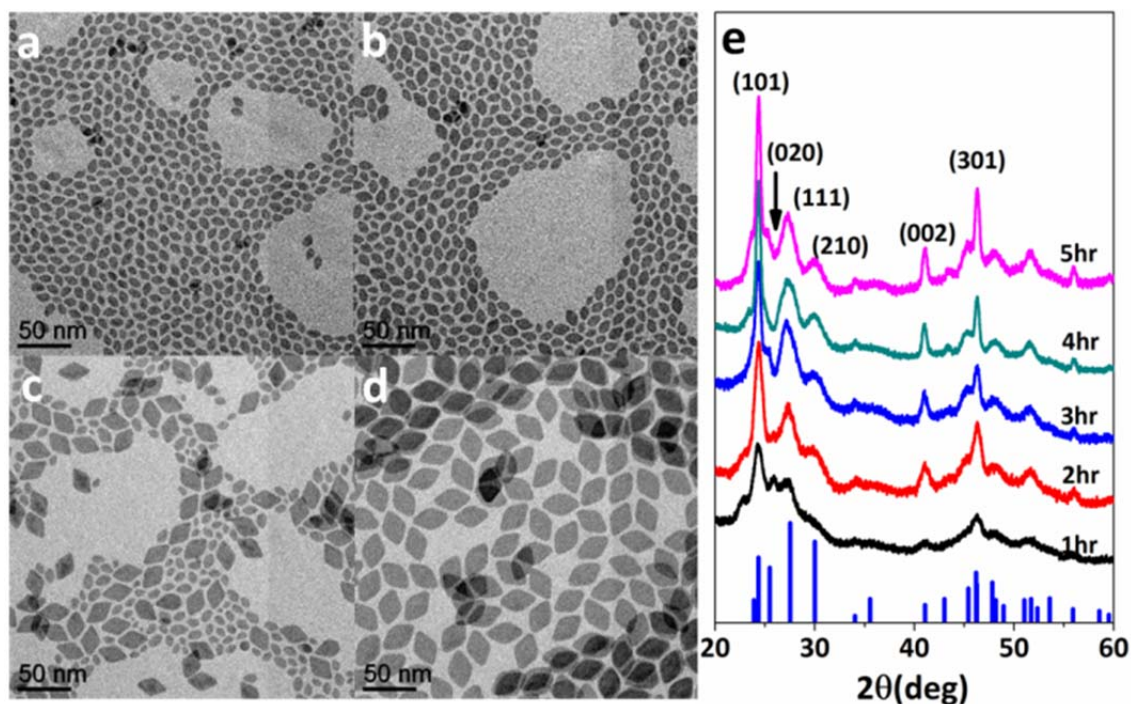
Figure 2.7. Size and morphology evolution of GdF_3 nanoplates during the reaction. TEM images at a) 1 hour, b) 2 hours, c) 3 hours, d) 4 hours reaction times. e) PXRD patterns of GdF_3 nanoplates corresponding to the reaction times.

Figure 2.7e displays PXRD patterns of GdF_3 nanoplates corresponding to the samples shown in TEM images. The crystal structure of GdF_3 nanoplates matches the orthorhombic phase (JCPDS#00-049-1804).[140] Figure 2.8 is a high-resolution transmission electron microscopy (HRTEM) image of GdF_3 rhombic nanoplates. Fast-Fourier transform (FFT) of HRTEM image of this structure shows the diffraction spots that are indexed as the {101}, {301}, {002} and {200} families of planes and the (101) plane lies in the edges of the nanoplates. This

indicates that our nanoplates are confined by the (020) plane and that growth occurs along the [101] direction. This description is further supported by the fact that the angles between the edges of nanoplates measured from the TEM image are 67.5^o and 112.5^o, which are consistent with the angles between the (101) planes calculated from the orthorhombic crystal structures. In addition, it is observed that peak intensities of (101), (301), and (002) reflections increase and the peak broadenings become narrower while broad peaks for the other planes maintain their intensities and broadenings. This also supports the fact that the nanoplates are growing along the [101] direction during the shape transformation.
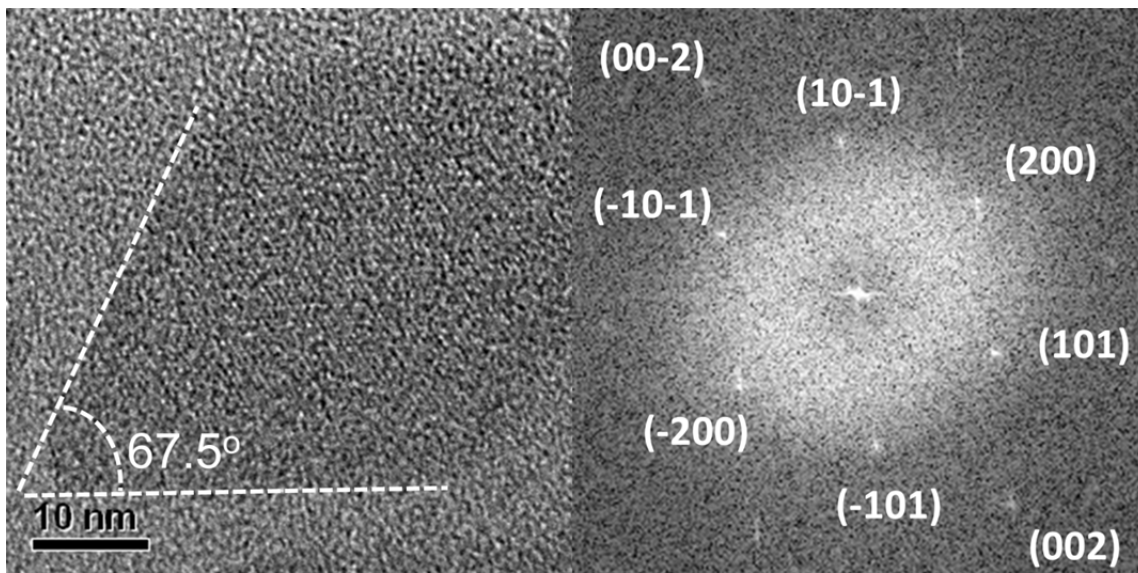
Figure 2.8. HRTEM image and FFT pattern of rhombic GdF$_3$ nanoplate.

While the width and length of the plates are easily measured by TEM, the thickness of the nanoplates is more difficult to measure due to the tilt in the

sample orientation when lying edge-on. To confirm the size and shape of the rhombic nanoplates, PXRD and SAXS are simulated based on atomistic models of nanoplates generated from the statistical analysis of TEM images. SAXS is highly sensitive to the size distribution of the particles and wide angle PXRD is sensitive to interatomic spacings and crystal structures. The GdF_3 nanoplate models are constructed using the orthorhombic unit cell. Atomic coordinates and scattering factors are entered into the Debye formula to generate the simulated patterns.[1] A size-series of nanocrystals were simulated and entered into a Gaussian dispersion equation, thus introducing a size distribution into simulated patterns. Due to the tendency of the nanoplates to align face-to-face, nanoplates on drop-cast films are found to have a preferred orientation. This results in inaccurate ratios of diffraction intensities in the experimental data. To circumvent this issue, we collect PXRD patterns of concentrated nanocrystal solutions filled in a glass capillary using transmission geometry, enabling the diffraction patterns to be obtained for randomly oriented nanoplates. Figure 2.9 shows the SAXS and PXRD patterns and the simulation results. The input parameters for the simulation are varied to fit the experimental pattern yielding a length of 35nm, a width of 25nm, a thickness of 2.4nm, and a dispersion in the length and width (defined as the standard deviation divided by the mean size) of 8%. The average length and dispersion, determined by measuring the length of 150 nanocrystals in TEM images, are 34.9nm and 4%, respectively, which is in accordance to the values obtained from X-ray simulation.
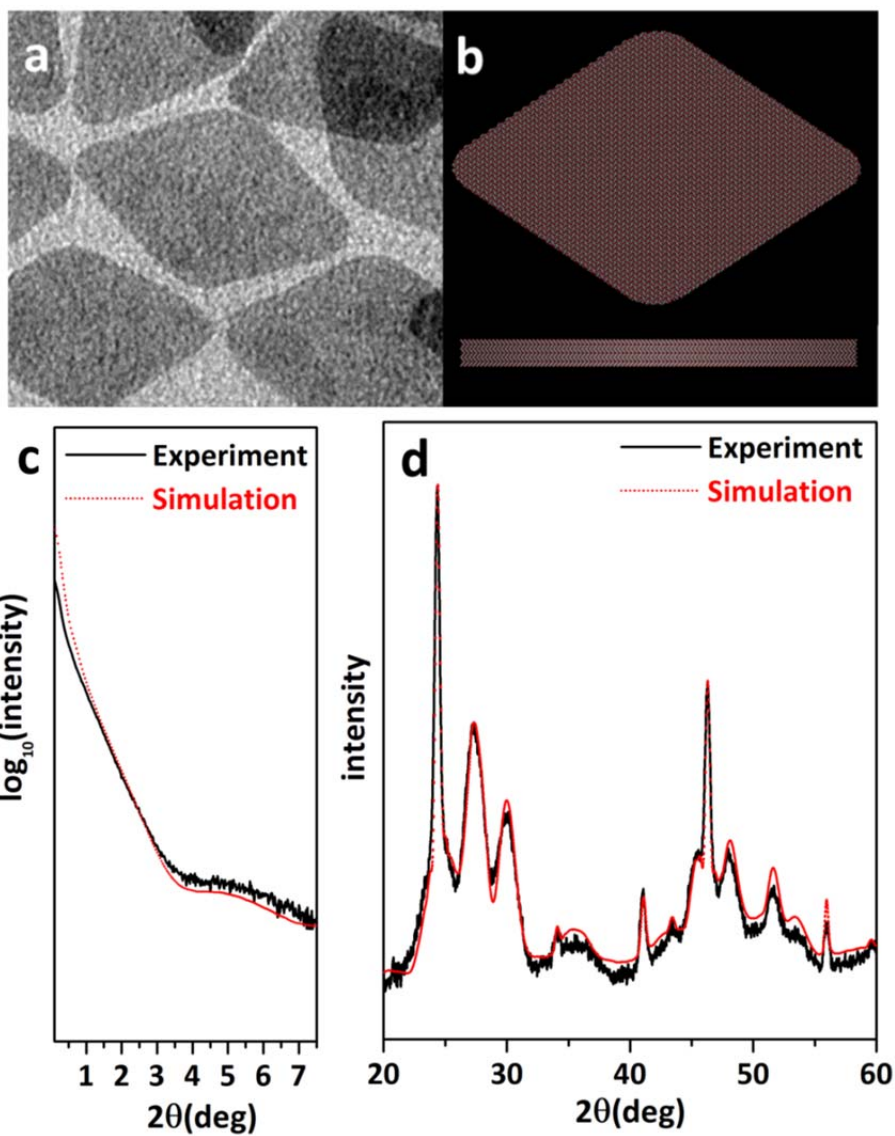
Figure 2.9. a) TEM image of rhombic nanoplates used for powder X-ray simulation. b) the atomistic model generated for simulation c) SAXS and d) PXRD pattern of rhombic nanoplates (the experimental data (black line) is plotted together with simulation pattern (red dot) for SAXS and PXRD).

Due to the high monodispersity and tunability in size and shape, the GdF_3 nanoplate could be a promising model system to understand the size and shape effects on magnetic properties. Gadolinium-based nanocrystals are widely used for imaging contrast agents for T_1 weighted MRI which provide positive contrast effects by generating a bright image in the presence of Gd^{3+} ions, which offers higher sensitivity by differentiating from the dark background.[51] In addition, the paramagnetism of lanthanide ions allows these nanomaterials to be utilized as a promising T_2 contrasting agents in high field MRI imaging.[141] In order to investigate the size dependence of nanoplates on MR relaxivity, we synthesized ellipsoidal and rhombic nanoplates and performed the ligand exchange with water-soluble polyacrylic acid to increase the compatibility in aqueous system. Relaxivity of the samples shown in Figure 10a and 10b are collected under a 9.4T magnet. Relaxivity measurement values of the sample in Figure 10a is $r_1 =$ $1.22 mM^{-1}sec^{-1}$, $r_2 = 25.5\ mM^{-1}sec^{-1}$ and the result of the sample in figure 10b is r_1 $= 1.29\ mM^{-1}sec^{-1}$, $r_2 = 80\ mM^{-1}sec^{-1}$, respectively. The results may indicate that the r_1 value is less sensitive to the size of the nanoplates, but the r_2 value is highly affected by the variation of the size. The surface ion of the nanocrystals is known as the major contributor to the longitudinal relaxation of water protons.[44] In the case of spherical nanocrystals, the relaxation rate increases with decreasing sizes of nanocrystals due to an increase in the surface-to-volume ratio. However, no significant change in r_1 relaxivities is observed by changing the size of the nanoplates, which may be attributed to the similar surface-to-volume ratio after changing the size of the nanoplates. On the other hand, increasing the size of the

nanoplates contributes increases their magnetic moment. Therefore, the larger nanoplates show the higher transverse relaxivity, r_2, due to more effective dephasing of the transverse magnetization by larger local magnetic fields. In addition, a high r_2 relaxivity and a high r_2/r_1 ratio indicate the possibility of using GdF_3 nanoplates as T_2 contrast agents for high field MRI imaging.
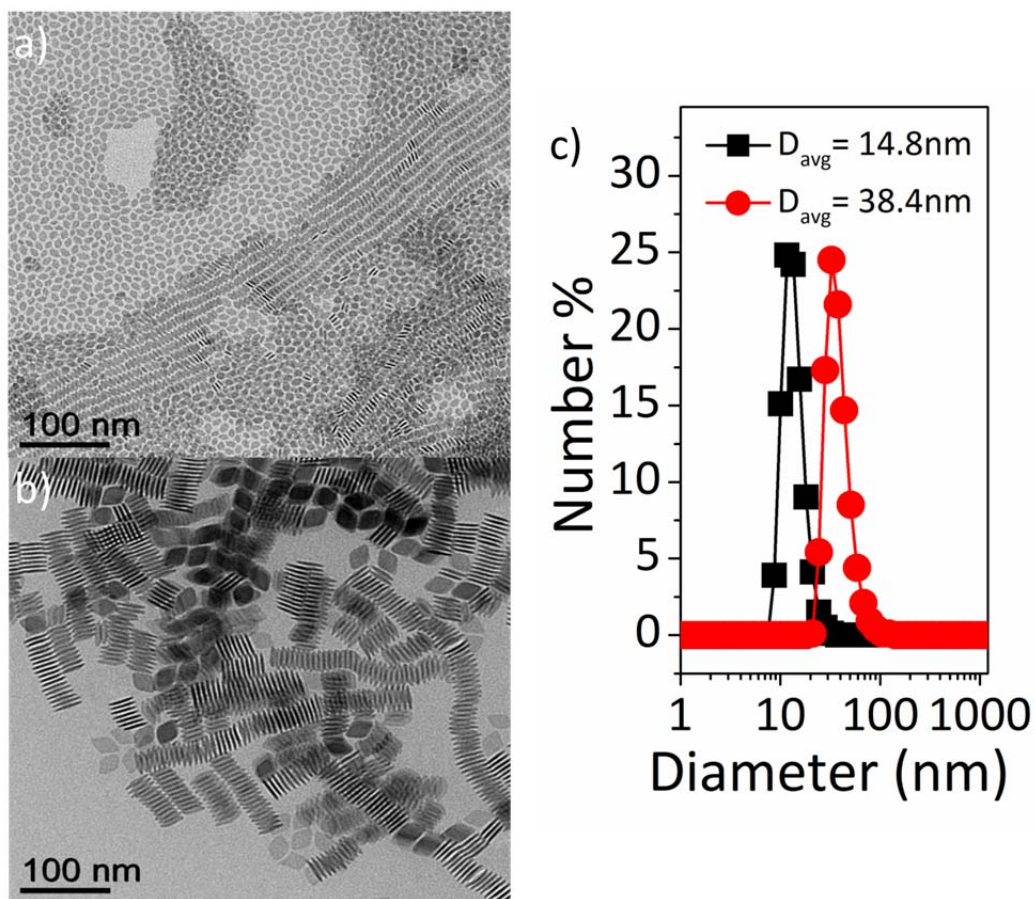
Figure 2.10. TEM images of a) ellipsoidal and b) rhombic GdF$_3$ nanoplates used for proton relaxometry measurement. c) DLS measurements of PAA-coated GdF3 nanoplates. The size of nanoplates after PAA modification is 14.8nm for ellipsoidal nanoplates(Figure 2.10a) and 38.4nm for rhombic nanoplates (Figure 2.10b).

2.3. Shape-Controlled synthesis of Gadolinium Oxide Nanoplates for Multimodal (MRI, NIR, and X-Ray Excited Fluorescence) Imaging

In this section, we report the shape-controlled synthesis of gadolinium oxide (Gd_2O_3) tripodal and triangular nanoplates. Gd_2O_3 is well known as an MRI contrast imaging agent due its unique high spin paramagnetism.[44,142] Through simple addition of lithium hydroxide (LiOH), which is used as a shape-directing agent, highly uniform Gd_2O_3 nanoplates are synthesized with morphology tunable from a tripodal to a triangular shape. The complex morphology of the tripodal nanoplate, which resembles the 14.2 × 8.5 × 3.8 nm shape of an IgG antibody,[143] could provide an additional degree of freedom to tailor shape-dependent properties and physiological interactions in biological system. In addition, we study near-IR to visible upconversion luminescence by co-doping erbium(Er^{3+}) and ytterbium(Yb^{3+}) into the host and X-ray excited optical luminescence (XEOL) with europium(Eu^{3+}) or terbium(Tb^{3+}) dopants. Coupled with magnetic properties, tripodal and triangular Gd_2O_3 nanoplates can offer unique opportunities for multimodal imaging probes.

Gadolinium oxide nanoplates are synthesized through thermal decomposition of gadolinium acetate precursors in the presence of lithium hydroxide. Lithium hydroxide is initially added to a non-polar solvent mixture of oleic acid and 1-octadecene and, upon heating to $110^{o}C$, lithium hydroxide reacts with oleic acid, likely forming lithium oleate, and becomes soluble in non-polar media. After

adding gadolinium acetate precursors, the reaction solution is heated to around $300^\circ C$ to $320^\circ C$, resulting in the formation of Gd_2O_3 nanoplates. A high N_2 flow rate during the heating was found to be critical to synthesize uniform Gd_2O_3 nanoplates with the desired morphology. We propose that upon heating, acetic acid formed from the acetate salts or decomposed components and water which volatilize in the reaction mixture can adversely affect the growing of nanocrystals.
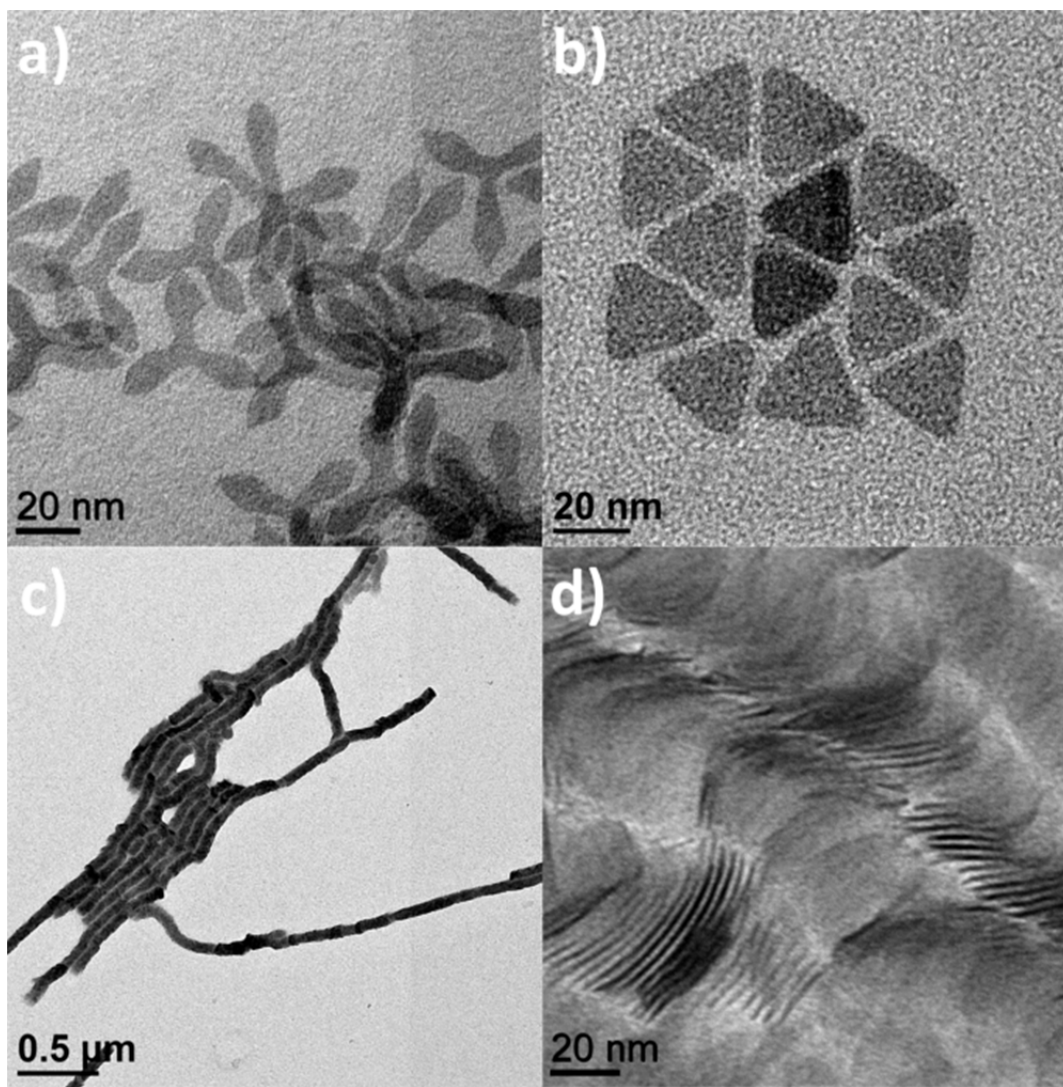
Figure 2.11. TEM images of Gd$_2$O$_3$ synthesized in presence of LiOH. a) tripodal nanoplates and b) triangular nanoplates. c,d) self-assembled Gd$_2$O$_3$ nanodisks synthesized in presence of NaOH

Shape control of Gd$_2$O$_3$ nanoplates is achieved by controlling the reaction time and temperature. Figure 2.11 displays transmission electron microscope

(TEM) images of Gd_2O_3 nanoplates synthesized at different temperatures. Gd_2O_3 nanoplates with tripodal plate morphology are formed after 1 hour at 300^oC (Figure 2.11a). At a reaction temperature of 320^oC, with the same reaction time, triangular shaped nanoplates are obtained as the final product (Figure 2.11b). Tripodal nanoplates show remarkable uniformity with narrow distributions even in the arm length and width (Figure 2.12). In addition, pure tripods are obtained exclusively without any other shape impurities, such as rods, bipods, or spheres. Lithium ions play an important role in the formation of tripod morphology. When sodium ions are used instead of lithium salts, disk-shape ultra-thin nanoplates are formed exclusively without any tripod or multipod morphologies (Figure 2.11c, d).
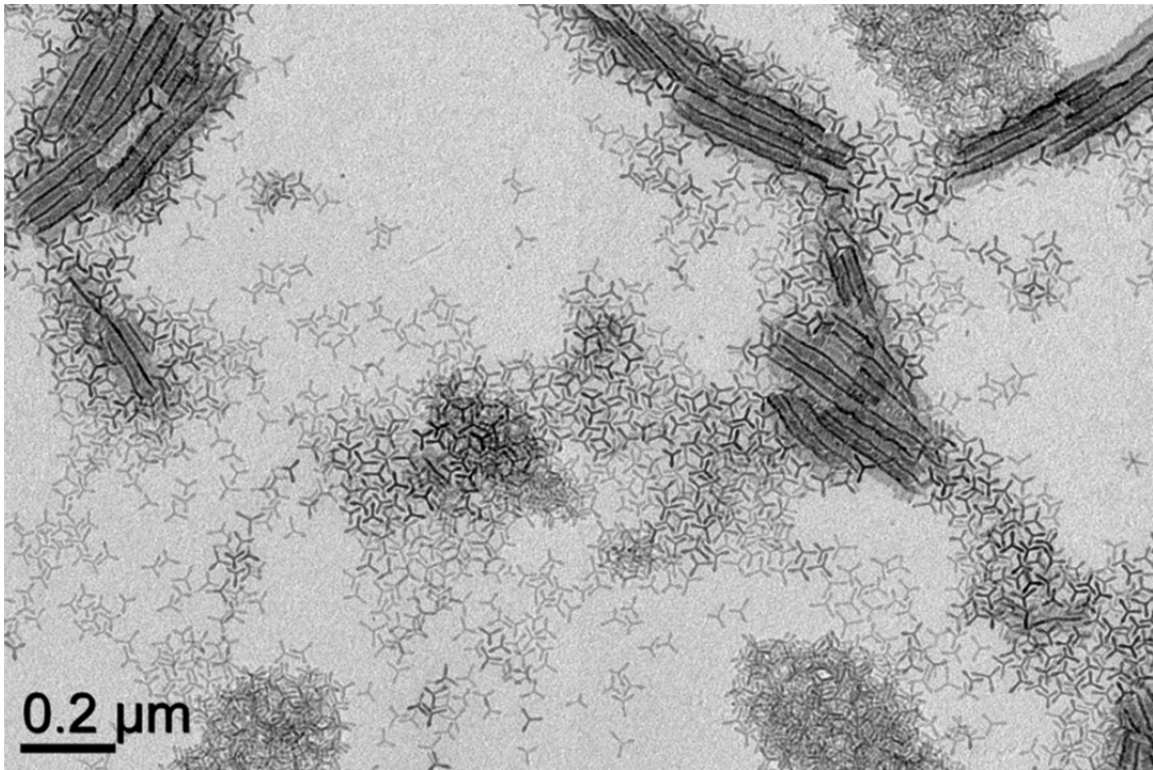
Figure 2.12. Low-magnification TEM image of Gd_2O_3 tripodal nanoplates

The crystal structure of Gd_2O_3 is characterized by powder X-ray diffraction (PXRD) and electron microscopy. Figure 2.13a displays the PXRD data of tripodal and triangular Gd_2O_3 nanoplates. The crystal structure of plate shaped Gd_2O_3 nanoplates most closely resembles the cubic-phase bixbyite structure (JCPDS No.43-1014). Similarities of peak broadening and intensity between the diffraction patterns of two different shapes indicate that the crystallographic structure of the tripodal and triangular nanoplates is maintained during the morphological transformation. Both nanoplates show a sharp (440) reflection in PXRD patterns and broad peaks for the other planes, suggesting that the (440)

plane lies in the plane of the nanoplates. Figure 2.13b-e displays high-resolution transmission electron microscopy (HRTEM) images of tripodal and triangular Gd_2O_3 nanoplates. Fast-Fourier transform (FFT) of HRTEM images of these structures show single-crystalline patterns with six-fold symmetry. For a cubic crystal structure, this symmetry would only be shown from the [111] zone axis, indicating that our nanoplates are confined by the (111) plane and that growth occurs along the [110] direction. This description is consistent with the tripod morphology where three arms of a nanoplate forming 3-fold symmetry correspond to the three equivalent {110} vectors in the [111] plane. In a previous report on Gd_2O_3 by Cao *et* al.[101] and an extended study of rare earth oxide nanoplates,[125] it is reported that Gd_2O_3 nanoplates form a structure where the top and bottom planes of Gd_2O_3 nanoplates are enclosed by (001) planes with the c-axis as the direction of thickness. By applying similar concepts to our experimental data, it is expected that the addition of lithium may stabilize the (111) plane of Gd_2O_3 relative to the (100) plane resulting in the formation of nanoplate morphology truncated by (111) plane.
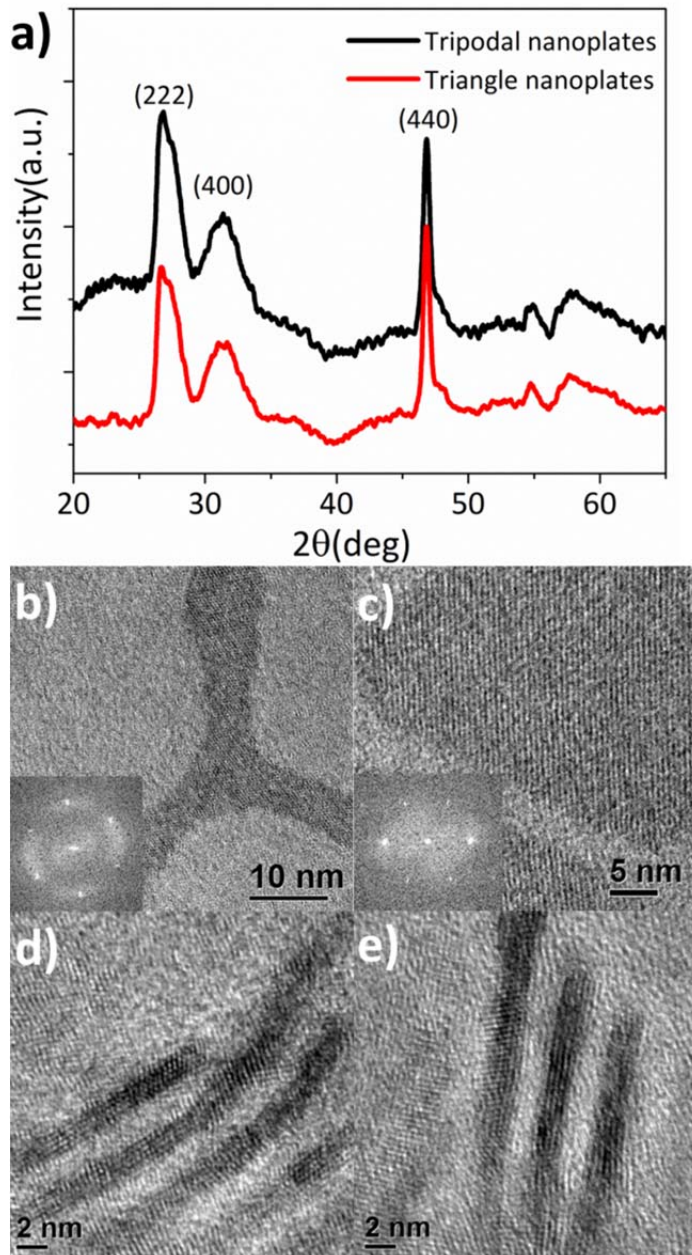
Figure 2.13. a) Powder X-ray patterns of tripodal and triangular Gd_2O_3 nanoplates. High resolution transmission electron microscopy (HRTEM) images of b, d) tripodal and c, e) triangular nanoplate. Insets are fast-Fourier transforms of HRTEM images.

Reflections of Gd_2O_3 nanoplates in PXRD patterns show deviations from the bulk peak positions. Measurement patterns show that the expansion of inter-planar distance along the (222) and (400) planes is more distorted than in the (440) reflection peak. Size-dependent lattice expansion of metal oxide structures at the nanoscale is often observed with decreasing crystalline domain size smaller than 10 nm.[144] Our nanoplates are confined by the (222) plane, which means that a large portion of atoms in the (222) plane is located on the surface. Different atomic coordination of the surface atoms may induce a change in atomic bond length, which modifies the inter-planar distance. In addition, due to the small size of the lithium ion, we anticipate that lithium may be doped into the Gd_2O_3 lattice inducing lattice expansion, as similar results with sodium doping in rare earth oxysulfide nanocrystals have been reported.[127]

A series of reactions conducted at a fixed reaction time but systematically varied reaction temperatures provide insight on the growth mechanism for tripodal and triangular nanoplates. At 280°C and a 30 min reaction time, a mixture of nanorods and small round shape disks are observed, with a small portion of tripodal nanoplates (Figure 2.14a). After 1 hour at 280°C, a large portion of disks and rods are transformed into the tripod shape (Figure 2.14b). Careful inspection of nanoplates in the reaction at 280°C reveals the formation of rod shaped nanoplates with arrow-headed tips, which suggests that coalescence between small crystals may contribute to the growth in this early reaction. This is further supported by the observation of branched nanoplates in which additional

branches grow from the center of the arms.(Figure 2.15). Tripod nanoplates of high uniformity are the exclusive product when the reaction temperature is increased to 290°C and 300°C after a one hour reaction time (Figure 2.14c, d). When the reaction temperature is increased to 310°C, the aspect ratio of each arm decreases, forming a more triangular shape (Figure 2.14e). Triangular plates are exclusively observed after a 1 hr reaction at 320°C (Figure 2.14f).
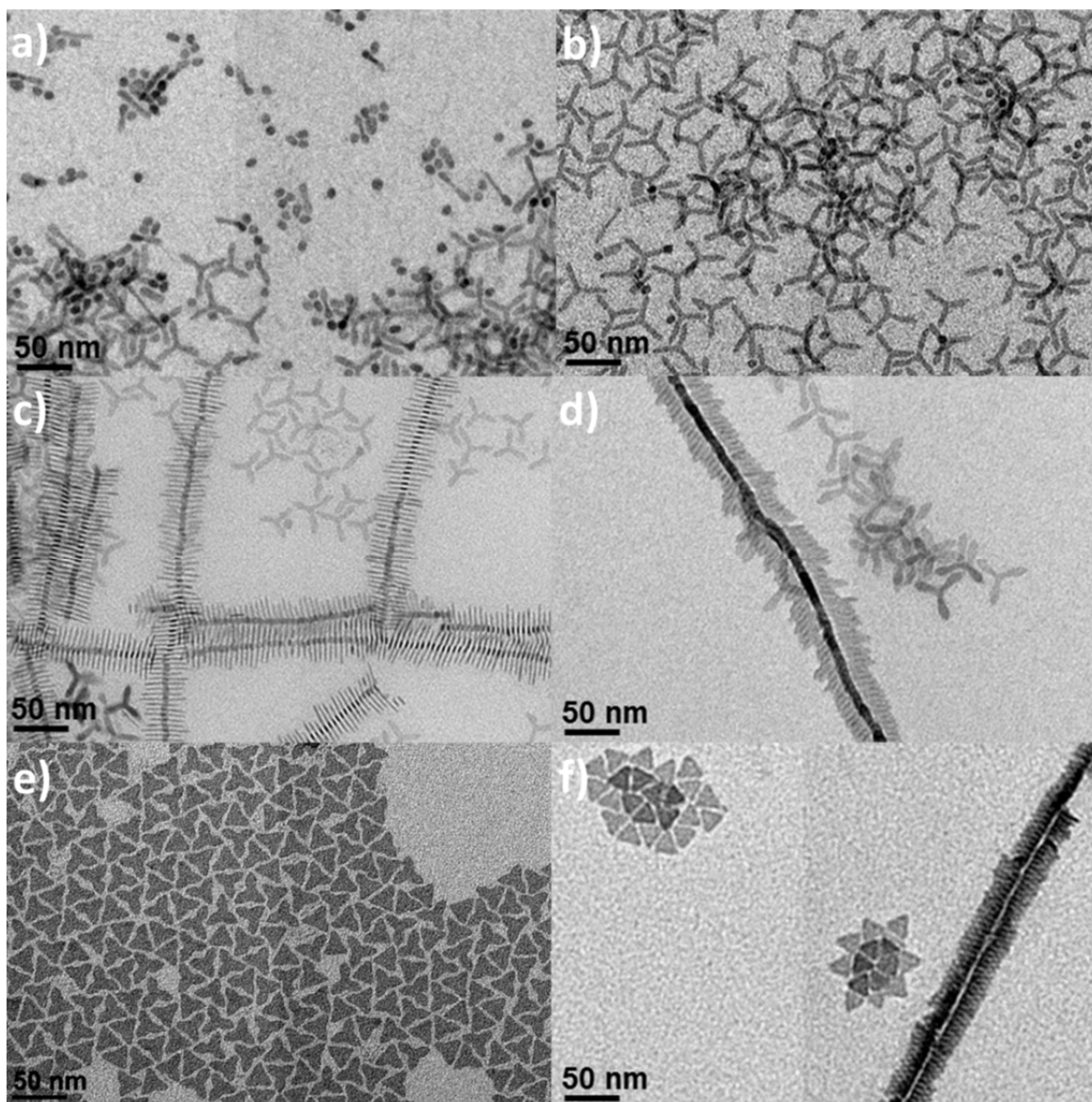
Figure 2.14. Temperature dependent shape transformation. TEM images of nanoplates synthesized at a) 280°C for 30min, b) 280°C, c) 290°C, d) 300°C, e) 310°C, f) 320°C for 1 hr.
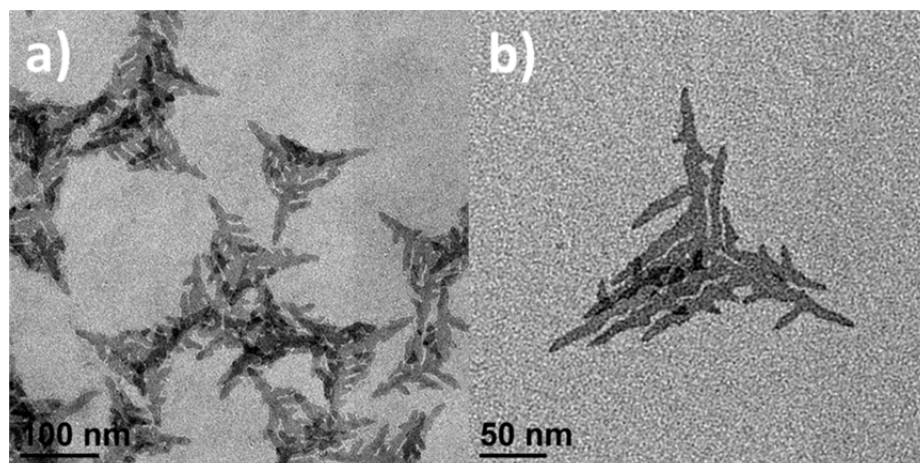
Figure 2.15. a), b) Branched Gd_2O_3 nanoplates

To investigate the shape evolution of nanoplates, aliquots were taken during a single reaction and analyzed by TEM. Figure 2.16a-e represents TEM images of nanoplates taken at increasing time intervals for a 300 $^{\circ}$C reaction temperature. Tripodal nanoplates are first formed after one hour with a tip-to-tip distance of 34 nm and a 2 nm thickness (Figure 2.16a, 2.13d). After aging at the same temperature, ripening occurs, which induces a shape transformation in which the arm length decreases and the arm width increases. After 4 hours, the morphology is completely transformed to a triangular shape with a 26 nm edge length and a 2 nm thickness (Figure 2.16b, 2.13e). The edge length of the triangular plates is always smaller than the arm-to-arm length of the tripodal plates, suggesting that this structural transformation is induced by atomic rearrangement of surface atoms to reduce the surface energy in the nanoplates, as illustrated in Figure 2.16f. All of the data indicate that branched nanoplates form at an early stage in the reaction and the thermodynamically stable triangular

shape results when sufficient energy is supplied to the reaction by increasing the

reaction temperature or extending the reaction time. It is notable that the size and

shape uniformity is maintained throughout the whole shape transformation.
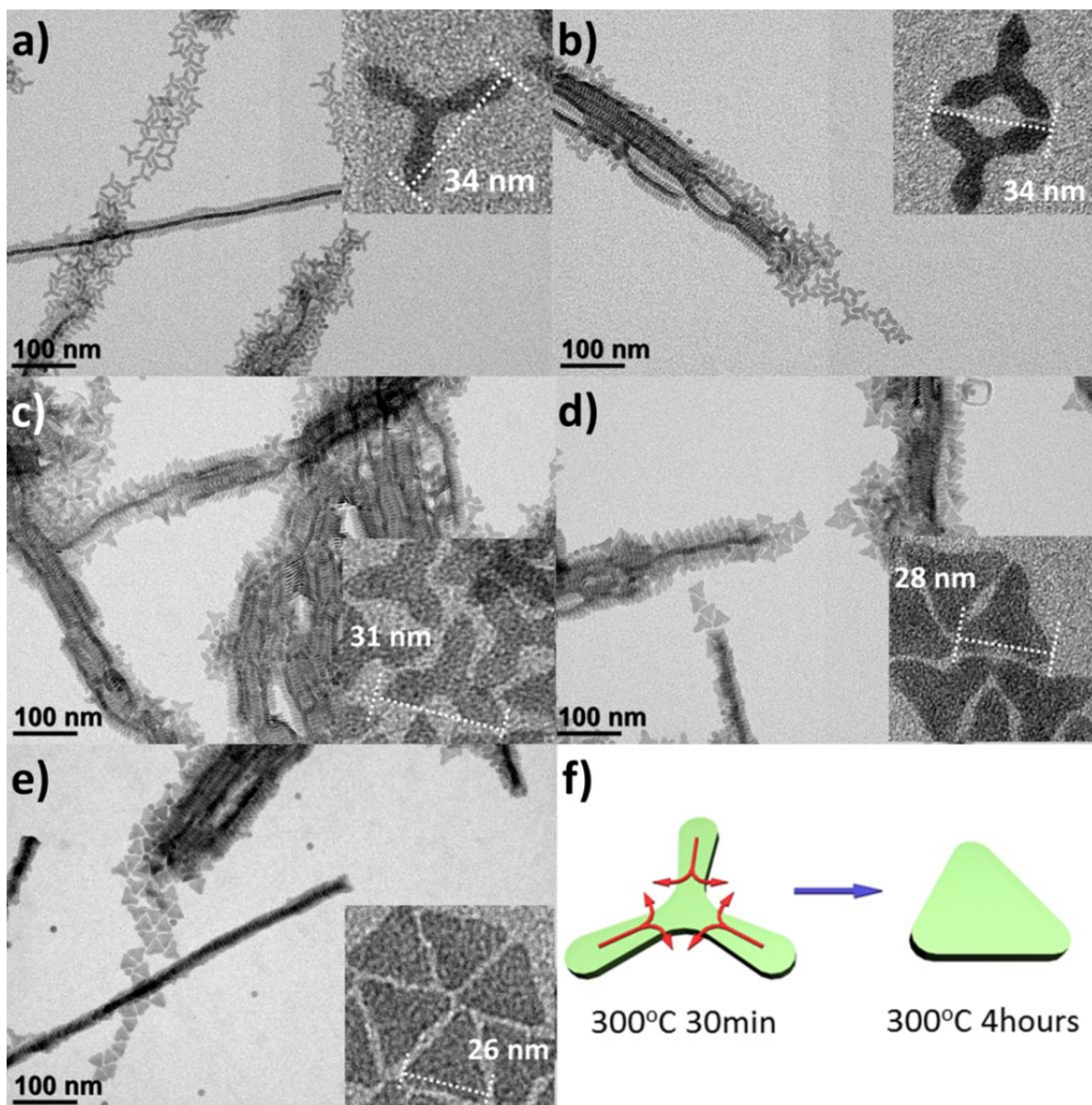
Figure 2.16. Reaction time dependent shape transformation. TEM images of nanoplates synthesized at a) 300°C for a) 30 min, b) 1 hour, c) 2 hours, and d) 3 hours e) 4 hours. f) Schematic of the nanoplate shape transformation.

Through proper selection of optically active dopants, tripodal Gd_2O_3 nanoplates with minimal change in particle morphology can fluoresce under excitation by a variety of external energy sources, offering an optical imaging modality. Upconverting Gd_2O_3 tripodal nanoplates are synthesized through an addition of erbium (Er^{3+}) and ytterbium (Yb^{3+}) co-dopants. This tripodal upconverter shows near-IR to visible upconversion luminescence. Figure 2.17a shows upconversion luminescence spectra of 2% Er^{3+}, 20% Yb^{3+} co-doped Gd_2O_3 nanoplates under 980nm irradiation. Characteristic green and red emission peaks are observed under near-IR excitation, located at 522 nm, 542 nm, and 656 nm, corresponding to $^2H_{11/2}{\rightarrow}^4I_{15/2}$, $^4S_{3/2}{\rightarrow}^4I_{15/2}$, and $^4F_9{\rightarrow}^4I_{15/2}$ transitions of Er^{3+} respectively. Upon introduction of europium (Eu^{3+}) or terbium (Tb^{3+}) dopants, Gd_2O_3 tripodal nanoplates can also exhibit an X-ray excited optical luminescence (XEOL) signature. To characterize the emission properties under high-energy excitation, emission spectra were collected with an X-ray diffractometer using an optical fiber coupled to CCD camera from a sample under Cu Kα X-ray excitation (λ =1.5416Å). Figure 2.17b displays emission spectra of Tb^{3+} and Eu^{3+}-doped Gd_2O_3 nanoplates under X-ray excitation. Depending on the dopant type, green and red emission peaks corresponding *f-f* transitions of Tb^{3+} and Eu^{3+}, respectively, are observed, confirming that Tb^{3+} or Eu^{3+}-doped Gd_2O_3 tripodal nanoplates can convert X-ray energy into visible light. Near-IR and X-ray photons show superb penetration into biological media, suggesting the

possibility of utilizing these nanocrystals as efficient energy converters for *in-vivo* applications.
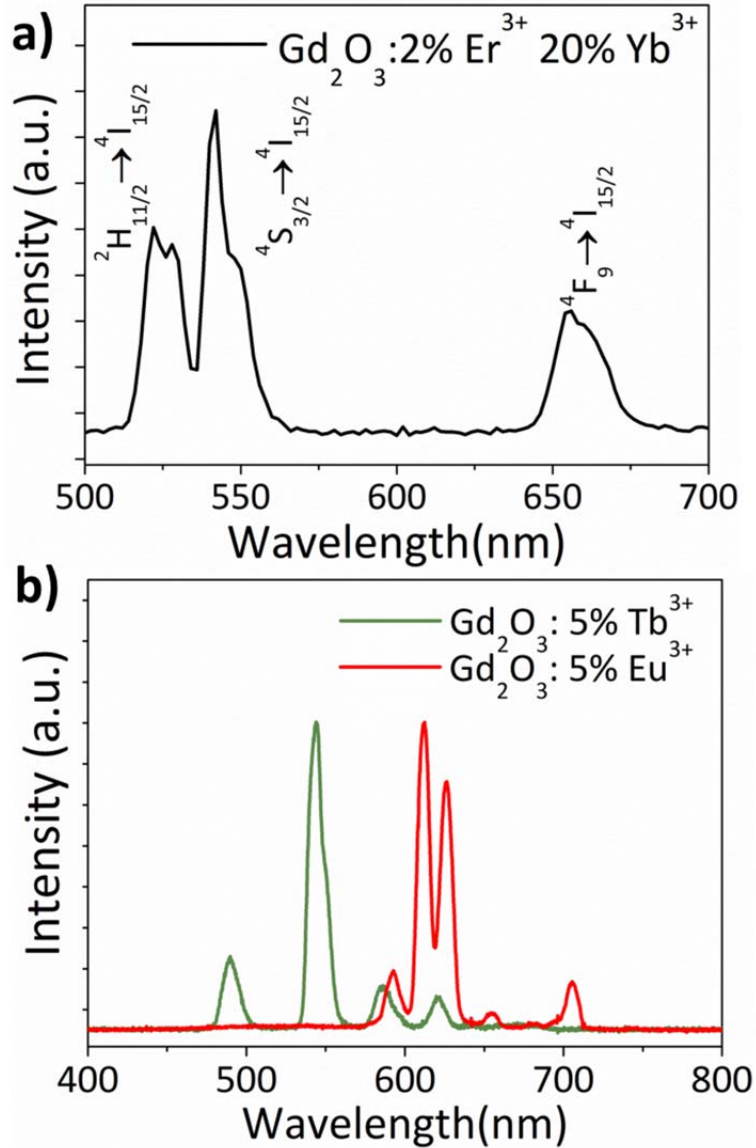
Figure 2.17. a) Upconversion luminescence spectra of Er^{3+}, Yb^{3+} co-doped Gd_2O_3 nanoplates under 980nm excitation. b) X-ray excited optical luminescence spectra of Eu^{3+} and Tb^{3+} doped Gd_2O_3 nanoplates excited by Cu Kα X-ray irradiation.

To demonstrate the capability of Gd_2O_3 nanoplates to provide MR contrast in aqueous media, we performed a ligand exchange reaction because the as-synthesized hydrophobic nanoplates are stabilized by long alkyl chain surfactants. Water-soluble PEI-coated Gd_2O_3 nanoplates are prepared using a two-step ligand exchange process in which the tetrafluoroborate anion (BF_4^-) acts as an intermediate capping group. Figure 2.18 presents Fourier transform infrared (FT-IR) spectra of untreated, BF_4^- treated, and PEI treated Gd_2O_3 nanoplates. After the first ligand exchange process with $NOBF_4$, the C-H stretching vibrations at 2800-3000cm^{-1} are completely removed, indicating that the original surfactants are efficiently exchanged with BF_4^- ligand. The weak binding affinity of BF_4^- ligands to the nanocrystal surface allows for efficient secondary surface modification using the PEI ligand. The occurrence of C-H vibrations after the second ligand exchange process with PEI indicates that the surface of nanoplates are over-coated by PEI ligands due to the C-H moiety in PEI molecules. PEI-capped Gd_2O_3 are highly transparent and show long-term colloidal stability without any noticeable precipitation in water.
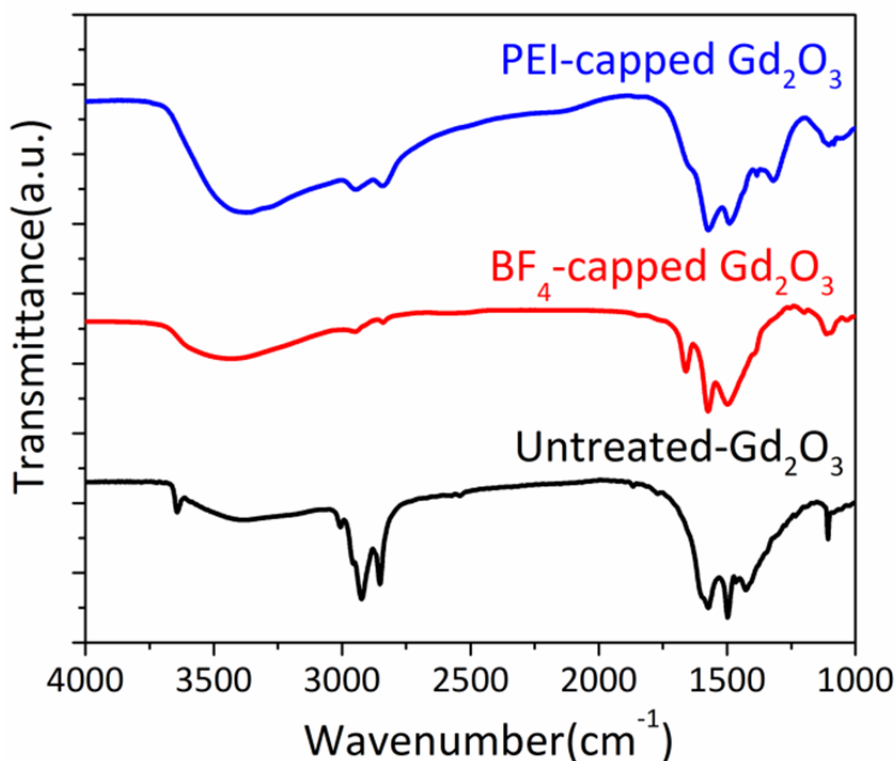
Figure 2.18. FT-IR spectra of Gd_2O_3 tripodal nanoplates before and after ligand exchange with BF_4^- and PEI.

The ionic relaxivity plots of PEI-capped Gd_2O_3 tripodal nanoplates at 9.4 T and 14.1 T magnet are shown in Figure 2.19. The calculated longitudinal relaxivity (r_1) decreases from 1.41 $mM^{-1}s^{-1}$ to 0.89 $mM^{-1}s^{-1}$ and the transverse relaxivity (r_2) increases from 140 $mM^{-1}s^{-1}$ to 193 $mM^{-1}s^{-1}$ with an increase in magnetic field strength (Table 2.1), which is consistent with a previous report.[145] Reduced spectral density at higher magnetic field strengths results in less efficient dipole-dipole relaxation and a corresponding decrease in r_1. The transverse relaxivity, r_2, increases as the magnetic field strength goes from 9.4 T to 14.1 T due to more effective dephasing of the transverse magnetization as a

result of larger local magnetic fields, which are proportional to the magnetic moment of the paramagnetic nanoparticles. As a result, the r_2/r_1 value increases from 99.3 at 9.4 T to 217 at 14.1 T, which makes Gd_2O_3 tripodal nanoplates promising candidates for increasing the detection sensitivity of various pathologies in T_2- and T_2*-weighted images collected at higher magnetic fields now available for preclinical and clinical MRI.
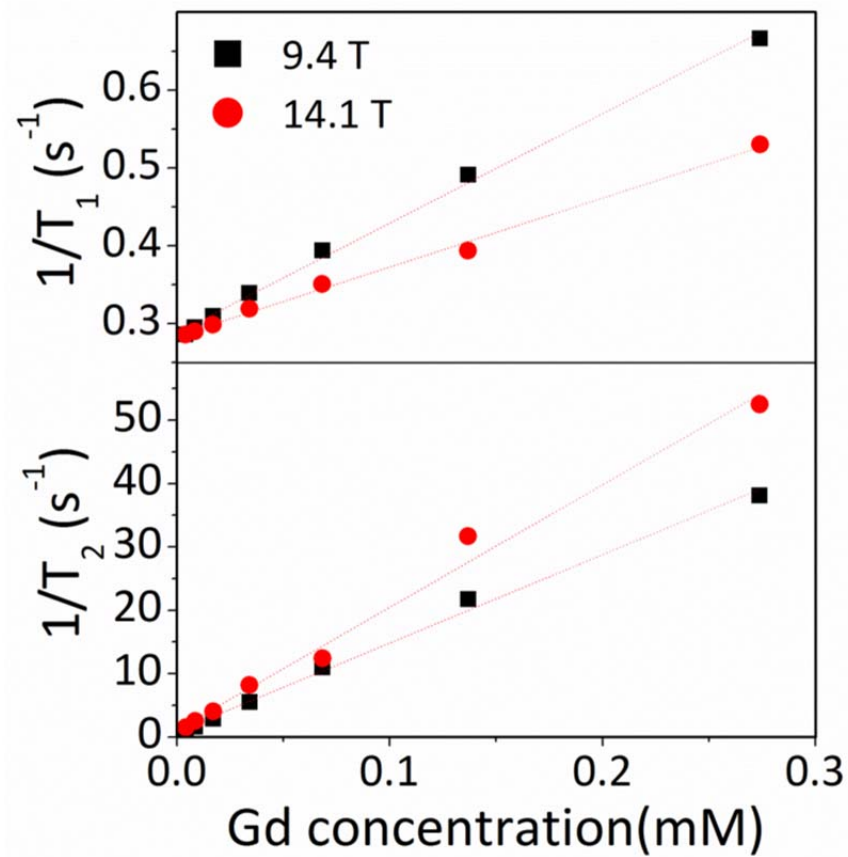
Figure 2.19. Longitudinal (top) and transverse (bottom) relaxivity curves of tripodal nanoplates

	r_1 (mM^{-1}s^{-1})	r_2 (mM^{-1}s^{-1})	r_2/r_1
9.4T	1.41	140	99.3
14.1T	0.89	193	217

Table 2.1. Relaxivites r_1 and r_2 of Gd$_2$O$_3$ tripodal nanoplate at 9.4 T and 14.1 T magnetic field.

2.4. Conclusion

In this section, we demonstrate the shape-controlled synthesis of fluoride and oxide-based Gd nanocrystals with high size and shape uniformity. Through the addition of alkali metal salts, typically NaF, LiF, LiOH, and NaOH, the morphology can span from nanospheres to nanorods, hexagons, and nanoplates including ellipsoidal, rhombic, tripodal, and triangular shapes based on the host materials. We observe that the sizes and shapes of these nanocrystals are precisely controlled by reaction parameters such as the reaction temperature, reaction time, and the amount of salts added into the reaction and that the shape transformation is governed by coarsening or Ostwald ripening. By controlled doping, synthesized nanocrystals could exhibit two-photon upconversion luminescence when doped with Er^{3+} and Yb^{3+}. When doped with Eu^{3+} or Tb^{3+}, characteristic visible emission is observed under X-ray excitation, allowing this material to also function as a nano-scintillator which converts high-energy radiation into visible light. We also investigate the MR relaxometry of of Gd-

based nanocrystals with varying the magnetic field. Taken together Gd based inorganic nanocrystals are a promising platform for multimodal imaging and therapeutic applications. Further, this could be a platform to understand shape dependent transport phenomena, and longitudinal tracking and assessment of environmental health impacts of these novel materials.

2.5.   Experimental Section

Materials. All chemicals are used as purchased without any further purification. Gadolinium(III) oxide (99.99%), erbium (III) oxide (99.9%), terbium(III) oxide (99.9%), europium(III) oxide (99.9%), ytterbium(III) oxide (99.99%), oleic acid (technical grade, 90%), oleylamine (technical grade, 70%), 1-octadecene (technical grade, 90%), lithium hydroxide monohydrate (99.95%) are purchased from Sigma Aldrich. Lanthanide acetate precursors are prepared by refluxing lanthanide oxide in acetic acid/water mixture (50 vol%).

Synthesis of GdF$_3$ nanoplates. 2 mmol of gadolinium trifluoroacetate and 6 mmol of lithium fluoride are added to a 125ml three-neck flask containing 30ml of oleic acid and 30ml of 1-octadecene. This solution is degassed at 125°C for 1hr. Then, the solution is heated to 290°C under N$_2$ environment at a rate of 10°C/min and maintained at this temperature for an hour (ellipsoidal plate) or for 4 hours (rhombic plate). Lithium ions are not incorporated into the nanoplates, but the amount of lithium fluoride added is adjusted to control the morphology and size of nanoplates. Purification is conducted by adding excess ethanol and

centrifugation. GdF_3 nanoplates are redissolved in hexane, chloroform, or toluene. Residual lithium fluoride, which is insoluble in non-polar solvents, is simply removed by centrifugation.

Synthesis of β-NaGdF₄ nanoparticle. The synthetic procedure is the same as the method used for GdF_3 nanoplates, except that sodium fluoride are used instead of lithium fluoride. The reaction is taken at 290^oC for 5 hours.

Synthesis of Gd₂O₃ nanoplates Six mmol of lithium hydroxide is added into a mixture of 12 mL of oleic acid, 18 mL of oleylamine, and 30 mL of 1-octadecene solvent and is heated to 110 ^oC. After evacuation at 110^oC for one hour to remove water, 3 mmol of gadolinium acetate is added and the solution is evacuated for an extra hour at the same temperature. Then, the reaction solution is heated to between 300^oC and 320^oC for 1 hour under high N_2 pressure, resulting in the formation of the nanoplates. The reaction solution is cooled to room temperature through addition of toluene. Purification is conducted through addition of excess methanol and centrifuging at 3000 rpm for 2 minutes.

Preparation of water-soluble nanocrystals Water-soluble Gd_2O_3 nanoplates are prepared through sequential ligand exchange process using BF_4^- as an intermediate ligand. First, ligand exchange with $NOBF_4$ is performed, as described previously.[146] The resulting nanocrystals are soluble in polar solvent such as dimethyl formamide (DMF) or dimethyl sulfoxide (DMSO). Secondary ligand exchange process is conducted with polyethyleneimine as a water-soluble ligand. Other water-soluble polymers such as polyvinylpyrrolidone (PVP) and

polyacrylic acid (PAA) can be used instead. 2 mL of nanocrystal solution in DMSO (0.1 mg nanocrystals/mL) is slowly added over 5 minutes into 2 mL of polyethyleneimine solution in DMSO (0.5 mg/mL concentration) and is stirred for an hour. 1 mL of toluene is added to induce flocculation and the particles are collected by centrifugation at 3000 rpm for 1 minute. Diluted HCl solution is added into the nanocrystal solution to increase the colloidal stability.

Structure characterization. TEM images and electron diffraction patterns are collected using JEM-1400 microscope equipped with a SC1000 ORIUS CCD camera operating at 120 kV. Powder X-ray diffraction is measured using a Rigaku Smartlab high-resolution diffractometer with Cu Kα radiation (λ=1.5416Å). X-ray excited optical luminescence is recorded using a fiber-optically coupled CCD (Ocean Optics USB-2000) using Cu Kα radiation (8.04KeV) generated from a 2.2 kW sealed tube generator. Upconversion luminescence is collected with Jovin Yvon Fluorolog-3 spectrofluorometer using a 980 nm diode laser (1.06 W power and a 0.05W/mm^2 power density) as an excitation source.

X-ray diffraction simulation. Atomistic models of GdF$_3$ nanocrystals are first constructed using Materials Studio 4.4.[140] The X-ray diffraction intensity, I (q), is calculated using Debye equations[1];

$$I(q) = I_0 \sum_m \sum_n F_m F_n \frac{\sin(qr_{mn})}{qr_{mn}}$$

where I$_0$ is the incident intensity, q=4πsinθ/λ is the scattering parameter for X-rays of wavelength λ, diffracted through the angle θ, r$_{mn}$ is the distance between

atoms m and n, with atomic form factors F_m and F_n, respectively. Atomic form factors are calculated from tabulated Cromer-Mann coefficients. The Debye equation is discretized by binning identical distances to give the following equation to reduce calculation time[147] :

$$I(q) = \frac{I_0}{q} \sum_m \sum_n F_m F_n \frac{\rho(r_{mn})}{r_{mn}} \sin(q r_{mn})$$

where $\rho(r_{mn})$ is the multiplicity of each unique distance (r_{mn}) in the structure.

Magnetic resonance measurements. Samples at different gadolinium concentrations were prepared in phosphate buffered saline containing 10% deuterium oxide. An inversion recovery pulse sequence modified to account for radiation damping[148] and a Carr-Purcell-Meiboon-Gill pulse sequence were used to determine the T_1 and T_2 relaxation times at 9.4 T and 14.1 T using a mono-exponential fit of the signal intensities. The r_1 and r_2 relaxivites were calculated from a linear fit of the relaxation rate constant as a function of gadolinium concentration.[149]

CHAPTER 3. SHAPE-CONTOLLED SYNTHESIS OF YTTRIUM-90 RADIOLABELED RARE EARTH FLUORIDE NANOCRYSTALS

3.1. Introduction

Nanocarrier platforms designed as imaging agents serve an important role in biomedical research for the study of biological processes and transport mechanisms.[150-152] They are also important in clinical medicine for early and accurate disease detection.[117,153-155] A variety of imaging modalities such as optical, magnetic, and nuclear have been utilized in different applications according to sensitivity and contrast, depth of signal penetration, as well as spatial and temporal resolution.[156] Among them, imaging with radiolabeled probes has attracted much attention due to high sensitivity and non-invasive detection of sub-picomolar concentrations of radionuclides.[157] Radiolabeled probes offer information on pharmacokinetics, probe distribution and localization, *in vitro* and *in vivo* transport mechanisms, and medical diagnosis supported by quantitative information calculated from radioactivity levels. Nanocrystal-based inorganic materials offer a great opportunity for designing multimodal imaging probes implementing complementary detection capabilities into a single material.[158] Properties of highly uniform nanocrystals are easily tailored by

customizing elemental composition among noble metals,[159] magnetic materials,[30] semiconductors,[113] phosphors,[160] and radioactive dopants, such as ^{64}Cu,[161] ^{59}Fe,[162] ^{56}Co,[163] ^{153}Sm,[164] ^{198}Au,[165] ^{125}I,[127] and ^{18}F.[166]

Among the different radioisotopes, ^{90}Y is particularly interesting as a nanocrystal dopant due to its unique properties. ^{90}Y is a pure β-emitter that yields one very high energy β-particle (E_{max} = 2.27 MeV, E_{mean} = 939 keV) with each decay.[167] At high doses, ^{90}Y-labeled materials are most often utilized as therapeutic agents with high energy emissions that travel a limited distance *in vivo,* which limits off-target effects (the maximum range in soft tissue is about 11 mm).[168] The half-life of ^{90}Y is 2.67 days, and is sufficient for tracing biological processes over several days while still having sufficiently rapid decay to prevent protracted toxicity. Even as a pure β-emitter, the low yield Bremsstrahlung photons and annihilation photon pairs from ^{90}Y decay are detectable by nuclear imaging using SPECT and PET, respectively, albeit with low sensitivity.[169,170] However, another interesting property of ^{90}Y is its optical imaging capability; ^{90}Y is one of the most efficient radionuclides for stimulating Cerenkov luminescence.[171] In this section, we report the shape-controlled synthesis and characterization of rare earth fluoride nanocrystals doped with ^{90}Y designed for *in vitro* and *ex vivo* radioisotopic detection, as well as non-invasive nuclear, optical radioluminescence and magnetic resonance imaging (MRI).

3.2. Shape-Controlled Synthesis of Isotopic Yttrium-90 Labeled Rare Earth Fluoride Nanocrystals.

Anisotropic rare earth fluoride nanocrystals are synthesized *via* high temperature thermal decomposition of rare earth chloride precursors in the presence of lithium fluoride (LiF) and various dopants depending on the intended application. $^{90}YCl_3$, when added as a radio-lanthanide dopant, incorporates inside the nanocrystal host preventing radioisotope leakage from nanocrystals during *in vitro* and *in vivo* applications. In our studies, gadolinium chloride ($GdCl_3$) and yttrium chloride (YCl_3) are used as host material precursors in the nucleation and growth reaction. These precursors are fluorinated using an excess amount of LiF resulting in fluoride-based nanocrystals (GdF_3 and $LiYF_4$, respectively).

Nanocrystal synthesis begins by heating LiF and $GdCl_3$ or YCl_3 precursors to 125 °C under high vacuum in oleic acid/1-octadecene solvent system (50:50 vol %) to remove excess water. The doping solution is prepared by mixing radioactive $^{90}YCl_3$ with non-radioactive YCl_3, to ensure that the total quantity of isotopic yttrium (i.e. ^{90}Y + Y) added in the dopant solution is 0.2% of total $GdCl_3/YCl_3$ host precursor. This solution is next added to the reaction mixture. The reaction is heated for another 30 min at 125°C under vacuum in order to remove water introduced with HCl in the doping solution. Nanocrystal formation (GdF_3:^{90}Y/Y or $LiYF_4$:^{90}Y) is initiated when the reaction is heated between 290°C and 320°C. Higher temperature reaction conditions permit the rapid nucleation and growth of nanocrystals. This helps reduce reaction times and allows for the

synthesis of monodisperse nanocrystals while minimizing the loss of radioactivity due to physical decay.

Radioactive thin layer chromatography (RadioTLC) confirms that ^{90}Y is successfully incorporated into the nanocrystal in near-quantitative yield, with no "free" or non-associated ^{90}Y-labeled species identified in the crude reaction mixture. We can easily control the specific activity of the ^{90}Y-doped nanocrystals (i.e., radioactivity (µCi)/nanocrystal mass (mg)) by varying the initial amount of ^{90}YCl$_3$ added into the reaction system. Note that the amount of ^{90}Y added (1 – 4 mCi) translates to 0.003 – 0.01% of total host material added. Thus, following full radioactive decay of ^{90}Y, the nanocrystal structure should remain intact since the majority of the nonradioactive Y-dopant is still present.

Nanocrystal size and shape are readily controlled by the modification of reaction time and temperature. Nanocrystal morphology is also tunable by changing the type of host material. With GdCl$_3$ precursors, ellipsoidal GdF$_3$:^{90}Y/Y nanoplates are formed at 290°C after a 20 min reaction (Figure 3.1a). Energy-dispersive X-ray spectroscopy (EDS) measurement reveals that nanocrystals are mainly composed of Gd and F elements.(Figure 3. 1d) Wide angle selected-area electron diffraction (SAED) patterns show the crystalline diffraction features of orthorhombic GdF$_3$.(JCPDS 49-1804) At an increased reaction temperature (Figure 3.1b) or increased reaction time (Figure 3.1c), rhombic GdF$_3$:^{90}Y/Y nanoplates are obtained as final products. This trend is consistent with results previously reported without the addition of radioisotopes, even though GdCl$_3$ is used as a precursor in this study instead of standard gadolinium trifluoroacetate

salts.[172] Using YCl_3 precursors instead of $GdCl_3$ and heating at 320°C for 20 min results in the major $LiYF_4$:^{90}Y product having nanowire morphology, with a small quantity of YF_3 rhombic nanoplates (Figure 3.1e, f). Nanowires reach several microns in length, but the width of an individual nanowire is approximately 4 nm on average. Increasing the reaction time to 40 min at the same temperature results in bullet-shaped $LiYF_4$: ^{90}Y nanocrystals approximately 250 nm long and 90 nm wide on average (Figure 3.1g, h).
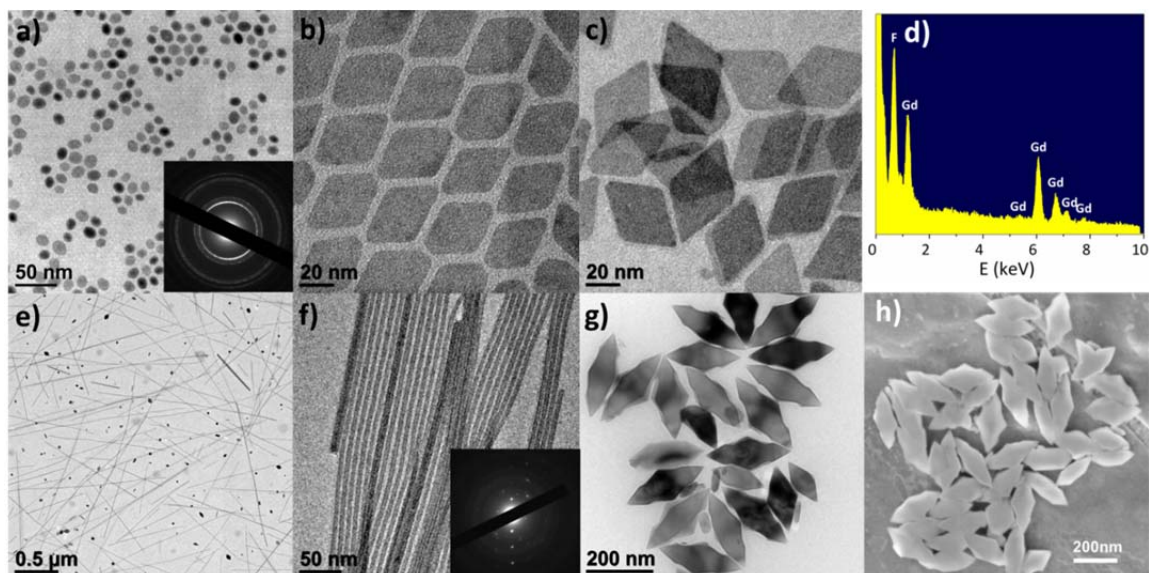
Figure 3.1. Characterization of Y-doped nanocrystals following full decay of ^{90}Y. (a-c) TEM images of GdF$_3$:Y nanoplates formed under different reaction conditions: (a) ellipsoidal nanoplates (290°C, 20 min), and rhombic nanoplates obtained at (b) 300°C for 20 min, or (c) 290°C for 4 h. (d) EDS spectrum of GdF$_3$:Y nanoplates. (e-h) When YCl$_3$ is used as the precursor, LiYF$_4$ nanowires are obtained at 320°C after 30 min (e, f), or bullet-shaped LiYF$_4$ nanocrystals are synthesized at 320°C for 40 min, as confirmed by (g) TEM and (h) SEM, respectively.

As synthesized, radiolabeled nanocrystals are only soluble in nonpolar solvents such as hexanes, toluene, and chloroform due to the long alkyl-chain ligands on the surface. For biological compatibility, water soluble ^{90}Y-doped nanocrystals are prepared *via* a two-step ligand exchange process using

tetrafluoroborate anions (BF_4^-) as an intermediate ligand and water-soluble polymers as the final stabilizer.[146,173] Nitrosonium tetrafluoroborate ($NOBF_4$) is used to prepare BF_4^--capped GdF_3:[90]Y/Y nanocrystals. Nitrosonium cations are known as strong oxidants and vigorously react with the nanocrystal surface stripping the original oleate ligands from the nanocrystal surface. We observed no loss of radioactivity from sample preparations following exposure to the highly chemically reactive environment of the $NOBF_4$ treatment, suggesting that ^{90}Y is strongly bound to the nanocrystal. Water-soluble polymers, polyethyleneimine (PEI), polyacrylic acid (PAA), and polyvinylpyrollidone (PVP), are used for secondary ligand exchange. Secondary ligand exchange with acidic and basic polymers did not result in any radioactivity lost, again suggesting stable ^{90}Y-doping within the nanocrystal host.

Oleate-capped and PVP-capped GdF_3:[90]Y/Y nanoplates are analyzed by radioTLC to confirm the identity and purity of radioactive species within the nanocrystal preparations. Figure 3. 2 shows that for surface coated GdF_3:[90]Y/Y nanoplates, intense radioactive signals are detected only at the TLC origin, whereas the presence of free ^{90}Y would have been detected at the TLC solvent front. This confirms that the ^{90}Y-doped GdF_3 nanoplates can be purified and samples in high radiochemical purity (>99%) are used for subsequent studies. Taken together, these studies demonstrate that this rare earth fluoride-based nanocrystal platform allows robust surface modification without loss of

radioactive dopants, and suggests the flexibility of this platform in various biomedical research and clinical therapy applications.
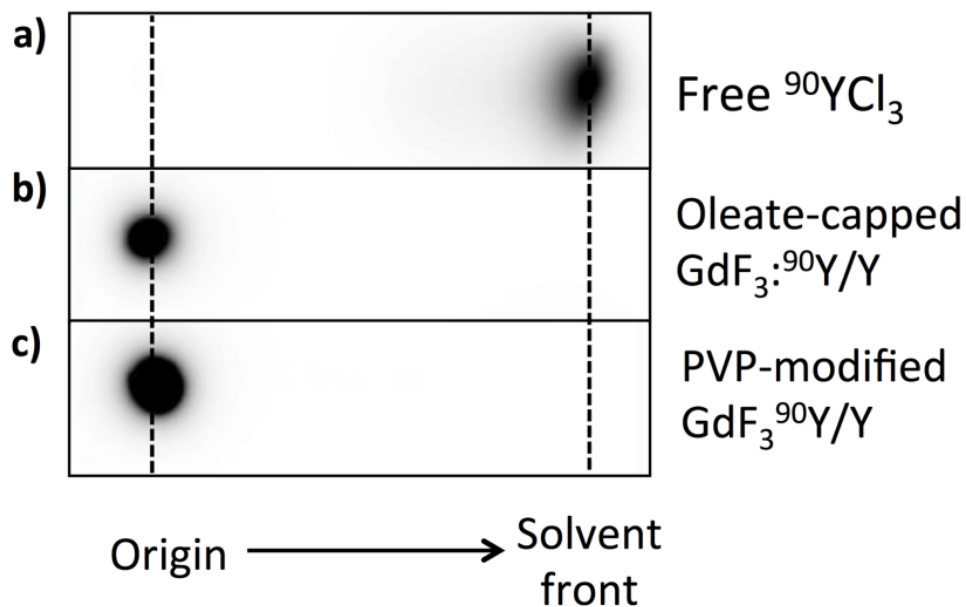
Figure 3.2. RadioTLC autoradiography images of (a) ^{90}YCl$_3$ compared to (b) oleate-capped, and (c) PVP-modified GdF$_3$:^{90}Y/Y, where free (i.e. non-bound) ^{90}Y is detected at the solvent front and ^{90}Y bound to nanocrystal formulations remains at the TLC origin.

Radioisotopic labeling of ligands and probes allows for quantitative tracing of these agents and enables the study of cellular interactions with high sensitivity. Owing to the robustness of ligand exchange and radiolabel stability toward

surface modification, we are able to examine charge-dependent cellular binding of ^{90}Y-doped anisotropic GdF$_3$ nanoplates, surface modified with differentially charged polymeric ligands (PEI and PAA). The size and size distribution of ligand-exchanged nanoplates is determined by dynamic light scattering (DLS) measurements. Although DLS defines the size of materials based on the assumption that the object has spherical morphology, DLS measurements provide a good indication of relative size and the dispersion state of anisotropic nanocrystals.[68] DLS data shows that PEI- and PAA-modified GdF$_3$:^{90}Y/Y nanoplates used for *in vitro* studies are estimated as 32.4 nm and 33.9 nm in size, respectively, forming a stable dispersion in aqueous media without any aggregation (Figure 3.3a). Zeta potential measurements of PEI- and PAA-modified nanocrystals show positive and negative net charge in deionized water solution, respectively, due to the amine (basic) and carboxylic acid (acidic) groups on the polymeric ligands (Figure 3.3b). To assess the interaction of the differentially charged nanoplates with biological membranes, a confluent monolayer of human umbilical vein endothelial cells (HUVECs) is used to model the systemic vasculature. ^{90}Y-doped nanoplates are formulated in serum-containing medium and the amount of nanocrystals binding to cells is measured over time by gamma counting. Non-bound nanocrystals are washed away and cell-bound radioactivity is normalized to the total radioactivity added (binding efficiency), as shown in Figure 3.3c. The amount of nanocrystals bound to cells is higher with positively charged PEI-modified nanocrystals than negatively charged PAA-coated ones. This result is likely due to the electrostatic attraction of

positively-charged PEI-modified particles to the negatively charged cell membrane, which is consistent with previously reported results.[174,175] However, the cellular binding and internalization of negatively-charged particles is strongly inhibited by serum opsonization.[176] With the assay having been conducted in serum-containing medium, the small difference in PAA- and PEI-coated nanoplate binding is perhaps due to particle-protein interactions in the medium prior to cellular interactions.
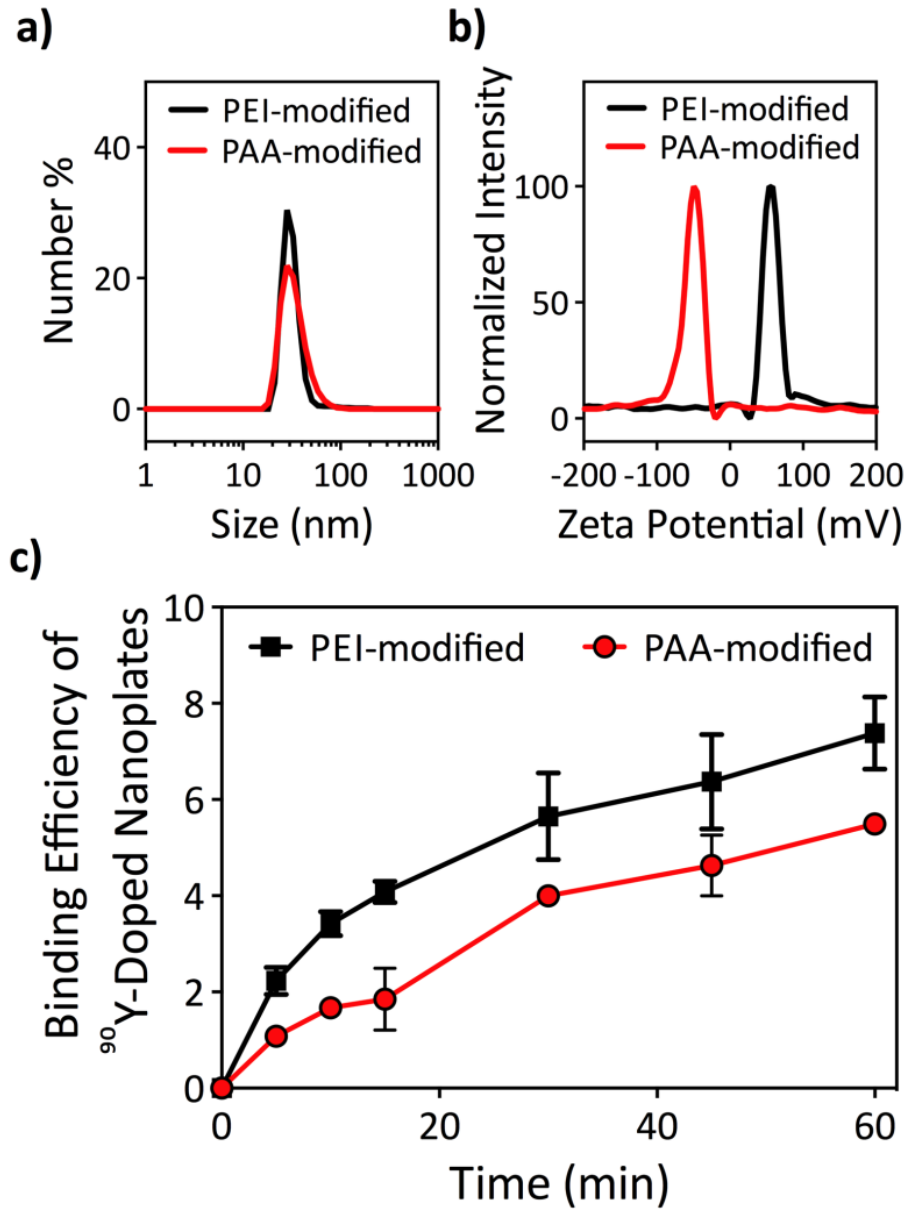
Figure 3.3. a) DLS and b) zeta-potential measurements of PEI-and PAA-modified ^{90}Y-doped GdF$_3$ nanoplates. c) *In-vitro* tracing of time-dependent binding of GdF$_3$:^{90}Y/Y nanoplates to HUVEC cells, with each time point run in quadruplicate. Black squares and red circles indicate binding efficiency of PEI and PAA-modified GdF$_3$ nanoplates, respectively.

Next, we investigated the potential of GdF_3:^{90}Y/Y nanocrystals as optical imaging agents. The charged particle emitted from a radionuclide induces local polarization along its path through medium emitting continuous optical spectra from near ultraviolet to visible and near-infrared, known as Cerenkov radiation.[177] A variety of radionuclides, including β^+, β^- and γ emitters, have been demonstrated as *in vivo* real-time optical imaging agents.[171] Even though the amount of light emitted from the radionuclides is lower than that of bioluminescence and fluorescence, lack of excitation reduces autoflurorescence from background fluorophores resulting in a significant increase in the signal-to-background ratios.[178] In addition, it has also been demonstrated that optical luminescence from radionuclides can excite other fluorophores such as quantum dots.[179,180] Careful design of nanocrystal-based probes can alter the luminescence spectrum in a manner more compatible for biological imaging and preclinical research. Aqueous dilutions of ^{90}Y-doped nanocrystals with radioactivity ranging from 0.55 μCi to 17.5 μCi per well are placed in a black-walled 96 well plate and ^{90}Y radioluminescence is investigated using an IVIS Lumina II optical imaging system. Since the average energy of β-particles emitted from ^{90}Y (E = 0.939 MeV) is higher than the threshold kinetic energy to produce Cerenkov radiation (E = 0.26 MeV in tissue), radioluminescence is detected from GdF_3:^{90}Y/Y nanoplates. Figure 3.4 depicts the linear relationship between total radiance and radioactivity. This relationship suggests that our ^{90}Y-doped nanocrystals are applicable for quantitative optical imaging studies as

reported for other radiolabeled nanocrystal probes, such as [198]Au-doped Au nanocages.[165]
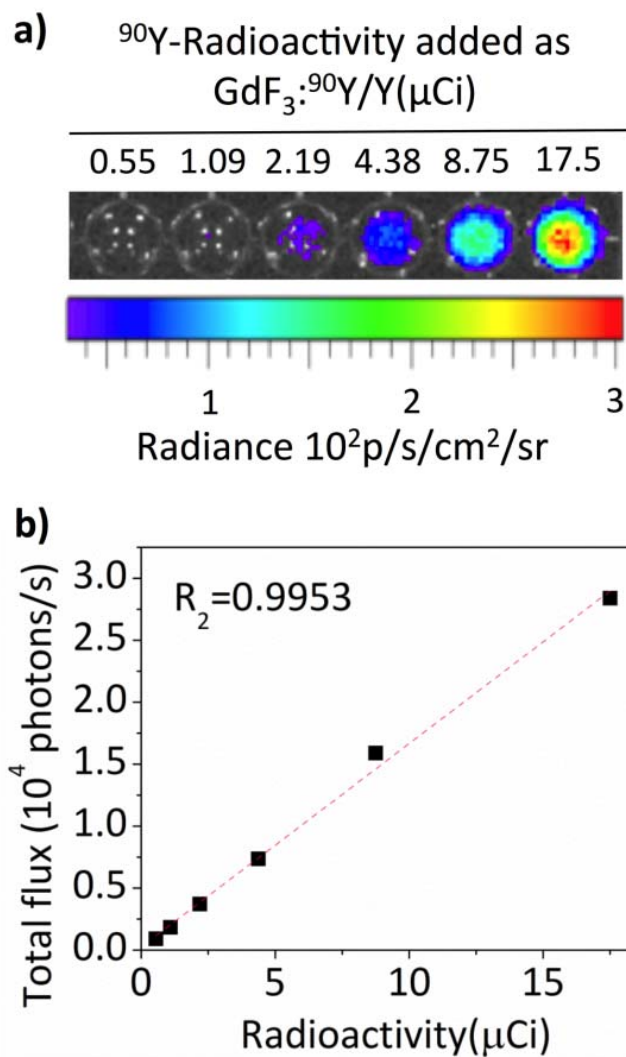
Figure 3.4. a) Optical images of aqueous suspensions of GdF_3:^{90}Y/Y nanoplates with varying amounts of radioactivity per well (0.55 to 17.5 µCi). b) Dose-dependent quantification of radioluminescence of GdF_3:^{90}Y/Y nanoplates dispersed in water.

Although nuclear and optical imaging techniques provide high sensitivity and quantification, these methods suffer from poor *in vivo* resolution. Magnetic resonance imaging (MRI) provides anatomical and functional information with high resolution of probe distribution.[181] This complementary imaging technique could be co-registered with nuclear and optical imaging to provide more reliable and comprehensive information of biological systems, albeit with lower sensitivity than nuclear and optical techniques. Due to the paramagnetic properties of Gd ions, GdF_3:^{90}Y/Y can also be utilized as an MRI contrast agent. MR relaxivity measurements of PEI-coated GdF_3:^{90}Y/Y nanoplates were performed using 9.4 T and 14.1 T magnets. Ionic relaxivity plots of PEI-capped nanoplates are shown in Figure 3.5. The calculated longitudinal relaxivities (r_1) are 0.99 $mM^{-1}s^{-1}$ at 9.4 T and 1.0 $mM^{-1}s^{-1}$ at 14.1 T. The transverse relaxivities (r_2) are 20.3 $mM^{-1}s^{-1}$ at 9.4 T and 71.8 $mM^{-1}s^{-1}$ at 14.1 T, respectively. Calculated r_2/r_1 ratios are enhanced from 20.5 to 71.8 with an increase of field strength. For the next generation of MRI, higher magnetic fields (> 7 T) are desirable to improve the signal to noise ratio a and enhance spatial resolution, shorten scan times, and reduce concentrations of contrast dosage.[182,183] High r_2 relaxivity and an enhanced r_2/r_1 ratio in increasing field strength make GdF_3 nanoplates promising T_2 contrast agents for high field MRI, currently utilized for preclinical and biomedical research.
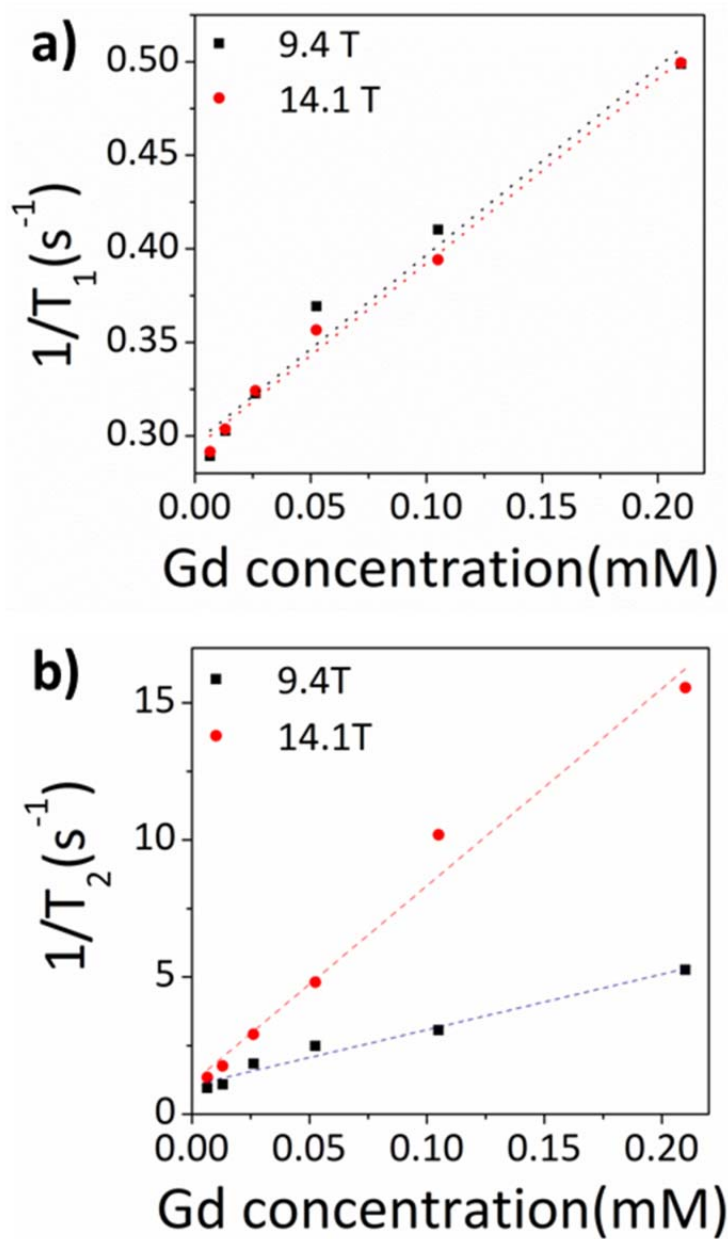
Figure 3.5. MR relaxivity measurements of PEI-modified ^{90}Y-doped GdF$_3$ nanoplates. a) Longitudinal (r_1 = 0.99 mM^{-1}s^{-1} at 9.4 T and 1.0 mM^{-1}s^{-1} at 14.1 T) and b) transverse relaxivity (r_2 = 20.3 mM^{-1}s^{-1} at 9.4 T and 71.8 mM^{-1}s^{-1} at 14.1 T) curves of PEI-modified GdF$_3$:[90]Y/Y nanoplates.

3.3. Conclusion

In this section, we demonstrate the size and shape controlled synthesis of ^{90}Y-doped lanthanide fluoride nanocrystals. In addition, radiolabeling with ^{90}Y and the versatility of surface modification allows rapid and quantitative analysis of physiological interactions between engineered nanocrystals and biological systems. Through Cerenkov emissions, radioluminescence of ^{90}Y-doped rare earth lanthanide fluoride nanocrystals can be investigated without an external excitation source. When combined with a paramagnetic gadolinium host, this nanocrystal can also be utilized as an MR contrast agent. Taken together ^{90}Y-labeled inorganic nanocrystals are a promising platform for multimodal imaging and therapeutic applications. Further, we have a platform that allows longitudinal tracking and assessment of environmental health impacts of these novel materials.

3.4. Experimental Section

Materials. All chemicals are used as purchased without any further purification. Gadolinium(III) chloride hexahydrate (99.999%), yttrium(III) chloride hexahydrate (99.99%), lithium fluoride (99.99%), oleic acid (technical grade, 90%), and 1-octadecene (technical grade, 90%) are purchased from Sigma Aldrich. ^{90}YCl$_3$ solution (0.05M HCl, ~500 Ci/mg) is purchased from Perkin Elmer.

Synthesis of ^{90}Y/Y-doped rare earth fluoride nanocrystals. ^{90}Y/Y-doped nanoplates (GdF$_3$:^{90}Y/Y or LiYF$_4$:^{90}Y) are synthesized according to the procedure previously reported with slight modification.[172] Briefly, LiF (7.7 mmol) and GdCl$_3$ (0.7 mmol) or LiF (6.1 mmol) and YCl$_3$ (0.66 mmol) are added to a 125 mL three-neck flask containing oleic acid and 1-octadecene mixture (50/50 vol%, 20 mL for GdCl$_3$ and 10 mL for YCl$_3$). This solution is degassed at 125°C for 1 h. Then, a solution of ^{90}YCl$_3$ (1-4 mCi, 22-89 nmol ^{90}Y in 0.05 M HCl) mixed with YCl$_3$ (0.2625mL, 1.4 μmol in 0.05 M HCl) is added into the reaction mixture and degassed for an extra 30 min. Next, the solution is heated to 290°C – 320°C under Ar environment at a rate of 10°C /min and maintained at this temperature for 20 min to an hour. Purification is conducted by precipitating nanocrystals in excess ethanol and centrifugation at 4000 RPM for 2 min. ^{90}Y-doped nanocrystals are re-dissolved in hexane. Residual lithium fluoride, which is insoluble in nonpolar solvents, is removed by centrifugation at 3000 RPM for 2 min. Radiochemical purity was assessed via digital autoradiography (FLA-7000, GE) of silica (SiO$_2$) TLC plates run in 0.1M ammonium acetate/ 50 mm EDTA. Radiolabeled nanocrystals remain at the origin while unbound ^{90}Y travels to the solvent front.

Preparation of water-soluble GdF$_3$:^{90}Y/Y nanoplates Water-soluble GdF$_3$:^{90}Y/Y nanoplates are prepared through a sequential ligand exchange process using BF$_4^-$ as an intermediate ligand. First, ligand exchange with NOBF$_4$ is performed, as described previously.[146,173] The resulting nanocrystals are

dissolved in dimethyl formamide (DMF). Secondary ligand exchange is conducted with polyethyleneimine (PEI), polyvinylpyrollidone (PVP), and polyacrylic acid (PAA) as water-soluble ligands. 2 mL of nanocrystal solution in DMF is slowly added to 2 ml of polymer solution over 5 minutes and stirred for 30 min. Polymer concentrations are 0.3 mg/ml PEI in dimethylsulfoxide, 0.3 mg/ml PAA in DMF, and 0.25 mg/ml PVP in DMF. Purification was conducted by adding non-solvent in the nanocrystal solution, specifically toluene for PEI, acetonitrile and toluene mixture (9:1) for PAA, and hexanes for PVP, to induce flocculation. The particles are collected by centrifugation at 3000 RPM for 1 min. Non-solvent is added until the solution becomes slightly opaque. Too much non-solvent results in the precipitation of polymers and is difficult to remove them from the pure particles. Diluted HCl solution for PEI-capped and diluted NaOH for PAA-capped nanocrystals is added into the nanocrystal solution to increase colloidal stability. Confirmation of radiolabel stability performed as described above.

Characterization. TEM images and electron diffraction patterns are recorded using a JEM-1400 microscope equipped with a SC1000 ORIUS CCD camera operating at 120 kV. Scanning electron microscopy (SEM) is performed on a JEOL 7500F HRSEM. Dynamic light scattering (DLS) measurement is performed on a Zetasizer NanoS (Malvern). Zeta-potential data is collected on a Beckman Coulter Delsa Nano-C system. ^{90}Y radio-luminescence was investigated using an IVIS Lumina II optical imaging system. Aqueous dilutions of PAA-modified

GdF$_3$:^{90}Y/Y nanocrystals with radioactivity ranging from 0.55 μCi to 17.5 μCi were placed in a black-walled 96 well plate and used for optical imaging.

Magnetic resonance measurements. MR measurements are performed by the method previously reported.[184,185] Briefly, PEI-GdF$_3$:^{90}Y/Y nanoplates with varying gadolinium concentration are prepared in a phosphate buffered saline and 10% deuterium oxide mixture. T$_1$ and T$_2$ relaxivities are collected in a Bruker AVIII 400 (9.4T) and Bruker DRX 600 (14.1T). An inversion recovery pulse sequence modified to account for radiation damping and a Carr-Purcell-Meiboon-Gill pulse sequence are used to determine the T$_1$ and T$_2$ relaxation times at 9.4 T and 14.1 T using a mono-exponential fit of the signal intensities. The r$_1$ and r$_2$ relaxivities are calculated from a linear fit of the relaxation rate constant as a function of gadolinium concentration.

Cellular binding tests. Cellular binding tests of GdF$_3$:^{90}Y/Y nanoplates are performed with PEI or PAA-coated nanoplates prepared in assay buffer (cell media with 10% FBS diluted 1:1 with PBS). HUVEC cells are grown to confluence in a 1% gelatin coated 96-well plate. Triplicate samples of ^{90}Y-doped nanoplates are incubated with cells at 37°C for up to 1 h. Cells are washed three times with 3% BSA/PBS and the radioactivity bound to cells was determined by a gamma counter (Wizard^2 2470, Perkin Elmer) in an open window using a standard for calibration.

CHAPTER 4. SHAPE DIRECTED SELF-ASSEMBLY OF ANISOTROPIC NANOCRYSTALS

4.1. Introduction

Assembled nanocrystal superlattices composed of one or more types of nanocrystals have been shown to have novel collective properties.[2,186-188] Single or multicomponent nanocrystal self-assembly enables the integration of nanocrystal building blocks with unique properties into periodic arrays through a bottom-up approach.[71,72] Control over nanocrystal superlattice structure is exerted through a variety of factors contributing to an emerging set of design rules which incorporate the type of nanocrystal,[74,75] the particle size and relative size ratio,[75,76] and the self-assembly conditions.[77,78] The interactions between nanocrystals in assembled structures may be precisely controlled by the symmetry and stoichiometry of the superlattices, resulting in structure-dependent collective properties.[189-193] This allows for the design of novel functional metamaterials by tailoring superlattice structures and the choice of nanocrystal building blocks.

Isotropic, spherical nanocrystals have been extensively studied as building blocks for single and multicomponent self-assembly. However, a more extended phase diagram is predicted by theoretical simulation,[81-87] and has been demonstrated experimentally through the use of anisotropic building blocks, in

which complex shapes are organized into ordered superlattices.[88-96] These superstructures are particularly interesting, because they resemble a variety of biological structures which are created by the directed self-assembly of small molecules or a hierarchical co-assembly of ordered structures. For example, the unidirectional self-assembly of anisotropic nanocrystals is reminiscent of the formation of fibrils, which are a major structural building block of biomaterials such as skin, tendon, bone, and other connective tissues.[194,195] Self-assembled superlattices can mimic complex biomaterials, acting as models to understand the process by which biomaterials self-organize and the structure-property relationships.[196]

Anisotropic nanocrystals offer a new design criterion for tuning assemblies, allowing the formation of liquid crystalline phases with differing orientational and positional order.[79,80] For example, nanorods and nanoplates are well-known anisotropic building blocks which form oriented liquid crystalline superlattices with differing orientational and positional order.[23,40,99,101,102,197,198] Anisotropic superstructures are previously fabricated by drying-mediated self-assembly,[97] electric-field-assisted assembly,[98] depletion attraction,[99] the Langmuir-Blodgett technique,[100] and destabilization by slow diffusion of a nonsolvent.[107] Recently, Manna *et al.* demonstrated that more complex anisotropic shapes such as CdSe/CdS octapods can also self-assemble into the hierarchically ordered three dimensional superlattices.[199,200] In addition, anisotropic nanocrystals often show unique shape-dependent physical and chemical properties, providing an

additional degree of freedom through which the collective properties of superlattices may be tailored.[80,201,202] There are a few examples of multicomponent self-assembly of anisotropic colloidal nanocrystals, such as the binary assembly of nanoplates with spherical nanocrystals[71,172] and Au nanowires or Au nanorods with Au nanospheres.[201,203,204] However, systematic control of the superlattice structures containing single or two anisotropic nanocrystals over a large area has remained a challenge.

In this chapter, we show the directed liquid crystalline self-assembly of anisotropic nanoplates by liquid interfacial assembly.[205] Liquid interfacial assembly is a simple, robust, and reproducible method to fabricate single or multicomponent nanocrystal superlattices.[206] In section 4.1, we show that anisotropic GdF_3 nanoplates self-assemble to form uniform liquid crystalline superlattices with long range orientational and positional order and demonstrate that macroscopic orientation of liquid crystalline superlattices is controlled by changing the sub-phase during the process. In section 4.2, liquid crystalline superlattices are characterized by novel X-ray based characterization techniques, such as out-of-plane and in-plane small-angle X-ray scattering with a laboratory X-ray diffractometer. In section 4.3, we represent that 1-dimensional nanofibril superlattices and 3-dimensional hierarchical superstructures can be formed with highly uniform tripodal Gd_2O_3 nanoplates. In section 4.4, we extend the concept of liquid crystalline self-assembly to the multicomponent system demonstting the

binary superlattices which are self-assembled from two different anisotropic nanocrystal building blocks.

4.2. Liquid Crystalline Self-Assembly of GdF$_3$ Nanoplates

GdF$_3$ nanoplates are chosen as the nanocrystal building blocks for the liquid crystalline self-assembly because the nanoplates are monodisperse and tunable in size and shape. Ellipsoidal and rhombic GdF$_3$ nanoplates are synthesized *via* high temperature colloidal synthesis, as described at chapter 2. Transmission electron microscopy [140] images indicate that ellipsoidal nanoplates are 16 nm along the long axis and 10 nm along the short axis (Figure 4.1a) and rhombic nanoplates are 35 nm along the long axis and 25 nm along short axis (Figure 4.1b).
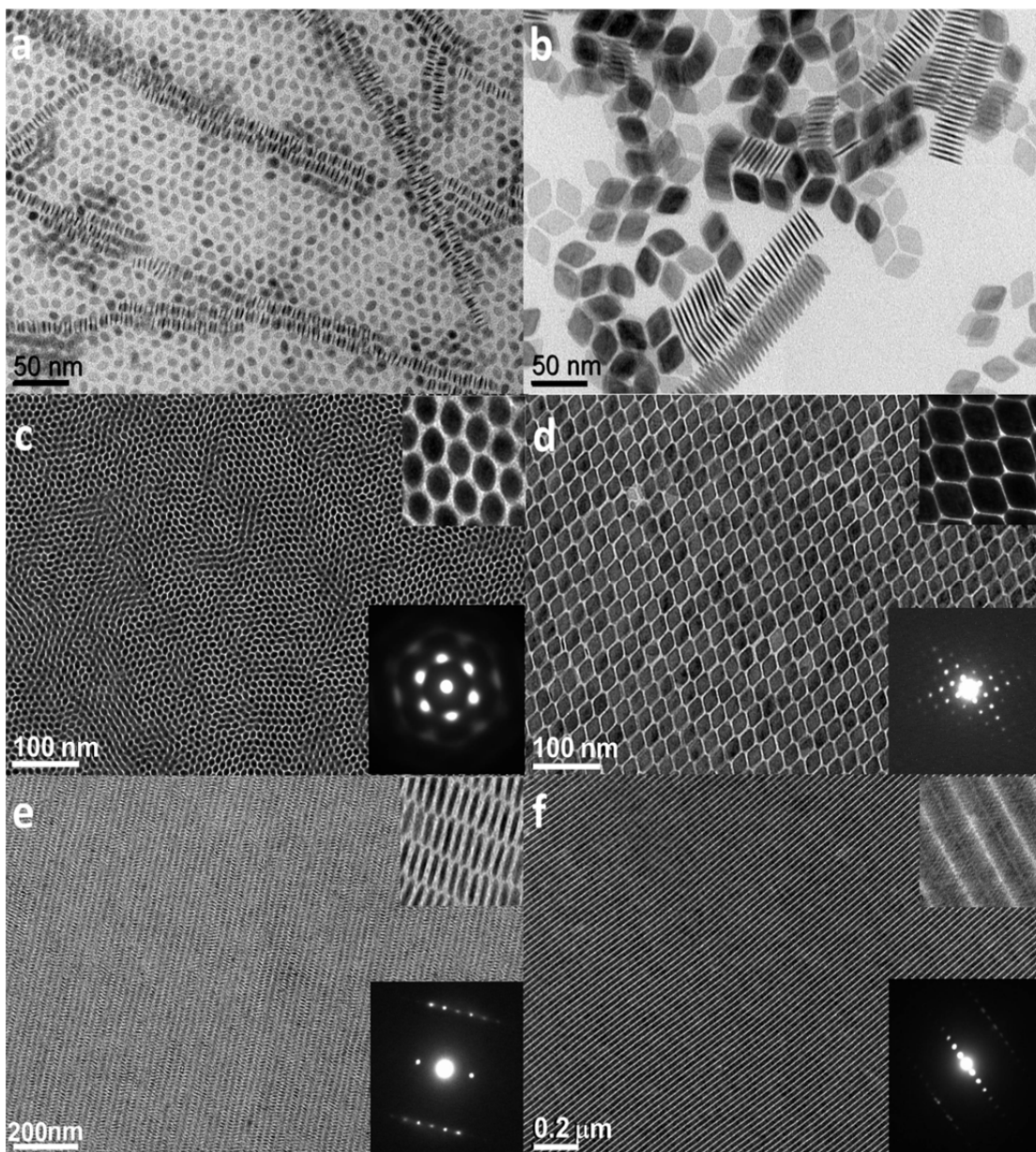
Figure 4.1. TEM images of a) ellipsoidal, b) rhombic nanoplates assembled into c, d) columnar and e, f) lamellar liquid crystalline superlattices through a liquid interfacial assembly technique. The upper inset is high magnification TEM image and the lower inset is small-angle electron diffraction pattern.

Liquid crystalline superlattices are formed using a liquid interfacial assembly and transfer technique in which a drop of nanocrystal suspension in a volatile solvent is slowly dried on glycol-type polar sub-phases on the Teflon well covering with glass slide and transferred to a substrate. Both ellipsoidal and rhombic nanoplates are observed to stack preferentially face-to-face, forming 1-D ordered assemblies (Figure 4.1a, 4.1b). Upon liquid interfacial assembly, edge-to-edge interactions also affect ordering simultaneously, building 3-D close-packed superlattices. Two different liquid crystalline structures are observed in films assembled on the surface of diethylene glycol. In some regions of the superlattice film, nanoplates assemble into columnar liquid crystalline structures, wherein the plates lie flat on the sub-phase and stack to form columns oriented out-of-plane (Figure 4.1c for ellipsoidal plate, figure 4.1d for rhombic plates). In other regions, ordered lamellar structures are observed, in which the nanoplates assemble by standing edge-on, forming a lamellar liquid crystalline structure parallel to the liquid interface (Figure 4.1e for ellipsoidal plate, figure 4.1f for rhombic plates).

The columnar assembly of ellipsoidal nanoplates shows short-range positional order with quasi-long range orientational order (see figure 4.1c). A hexagonal small-angle electron diffraction pattern indicates that the phase of the columnar assembly of ellipsoidal nanoplates is hexatic.[207] Locally, long axes of plates are oriented in the same direction, forming a centered rectangular columnar phase (see Figure 4.1c inset). Each column reflects the shape of an

isolated nanoplate, which indicates that the nanoplates within each column perfectly overlap to maximize the face-to-face interaction. The electron diffraction patterns of columnar assemblies of rhombic nanoplates show 2-fold symmetry representing rectangular columnar liquid crystalline phase (see Figure 4.1d inset). Electron diffraction patterns for lamellar superlattices of both ellipsoidal and rhombic nanoplates also have 2-fold symmetry (see Figure 4.1e, 4.1f inset). This is due to the periodicity of the nanoplates stacking face-to-face and the layering of each stack orthogonal to the stacking direction, indicating a smectic liquid crystalline phase. Only two sets of diffraction spots are observed even in multilayer superlattices, meaning that all nanoplates are oriented identically in the plane of the substrate.

Liquid crystalline structures with long range orientational and positional order are observed over large areas (Figure 4.2). Figure 4.3 displays TEM images of columnar superlattices of rhombic nanoplates at increasing magnifications. The low magnification image in Figure 4.3a shows that the domain size ranges between $1\mu m^2$ and $10\mu m^2$. The flat edges of rhombic plates enable the nanoplates to be crystallographically oriented as reflected in the wide-angle single crystalline electron diffraction pattern (inset Figure 4.3d). Diffraction spots were indexed as the {101}, {301}, {002} and {200} families of planes, which is consistent with the Fast Fourier transform (FFT) of the high-resolution TEM (HRTEM) image of an isolated nanoplate (Figure 4.4). In addition, rhombic nanoplates are observed to pack efficiently by perfect space filling analogous to

tiling of building blocks, leaving minimal space except for the ligand bound to the

surface.
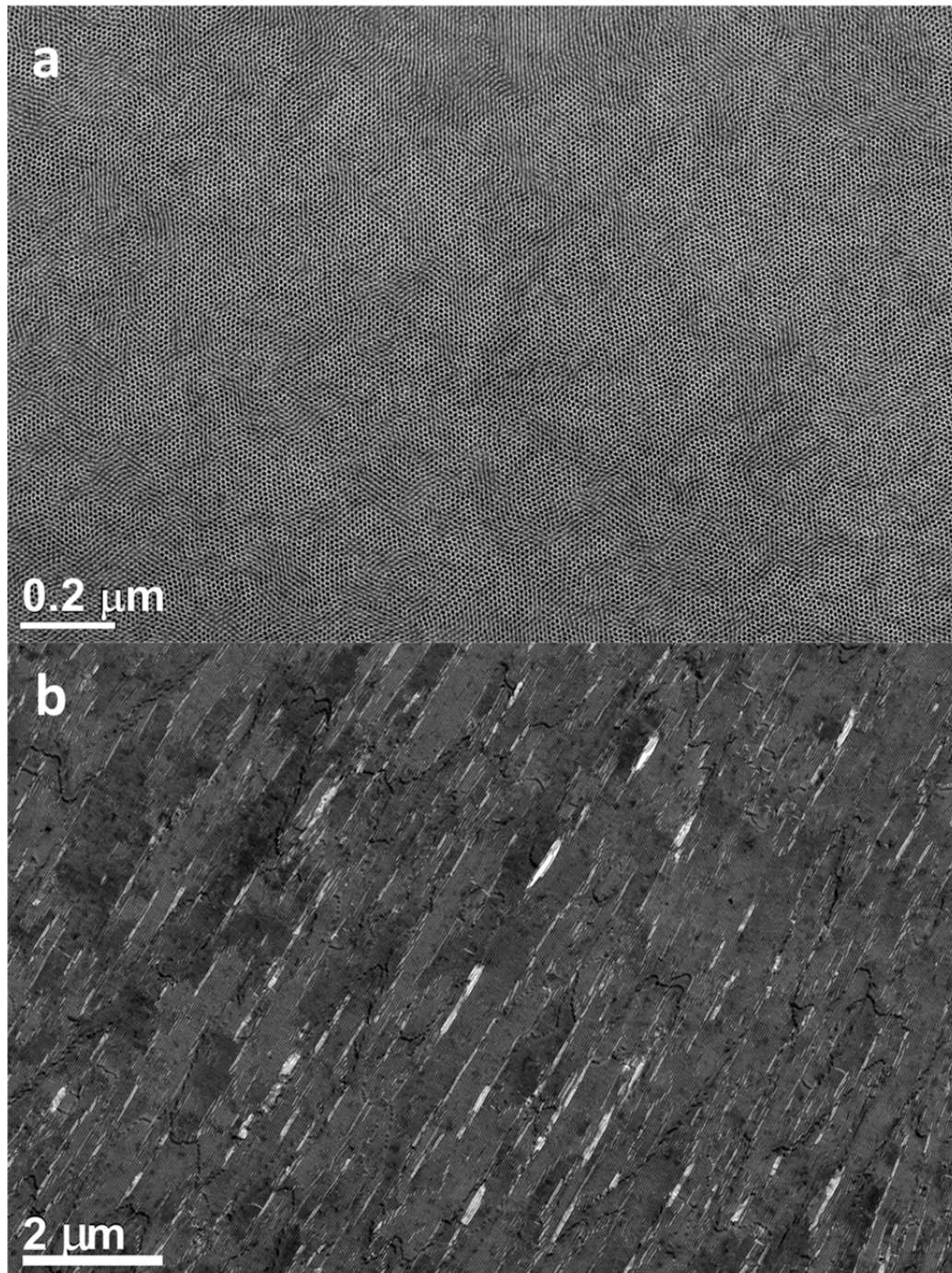
Figure 4.2. Large area TEM image of a) columnar liquid crystalline assembly of ellipsoidal GdF$_3$ nanoplates and b) Large area TEM image of lamellar liquid crystalline assembly of rhombic GdF$_3$ nanoplates.

.
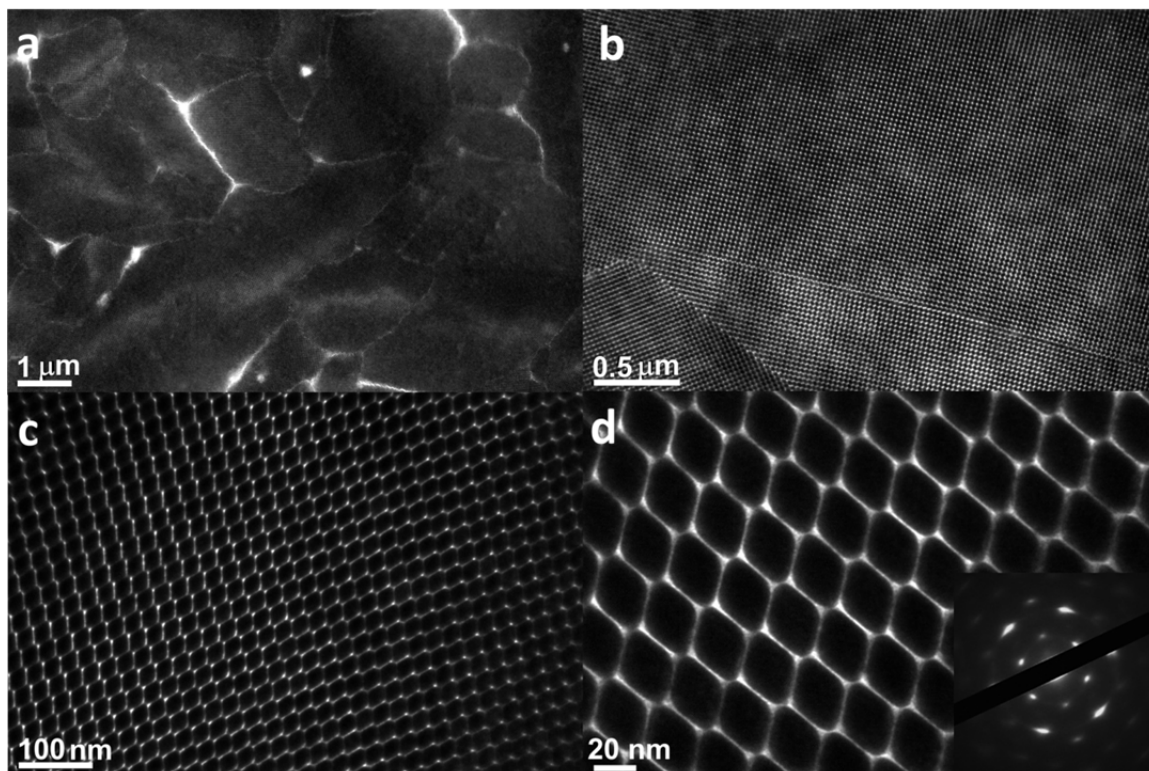
Figure 4.3. Series of TEM images of columnar liquid crystalline phase domains of rhombic GdF$_3$ nanoplates from low magnification to high magnification. Lower inset is a wide angle electron diffraction pattern.
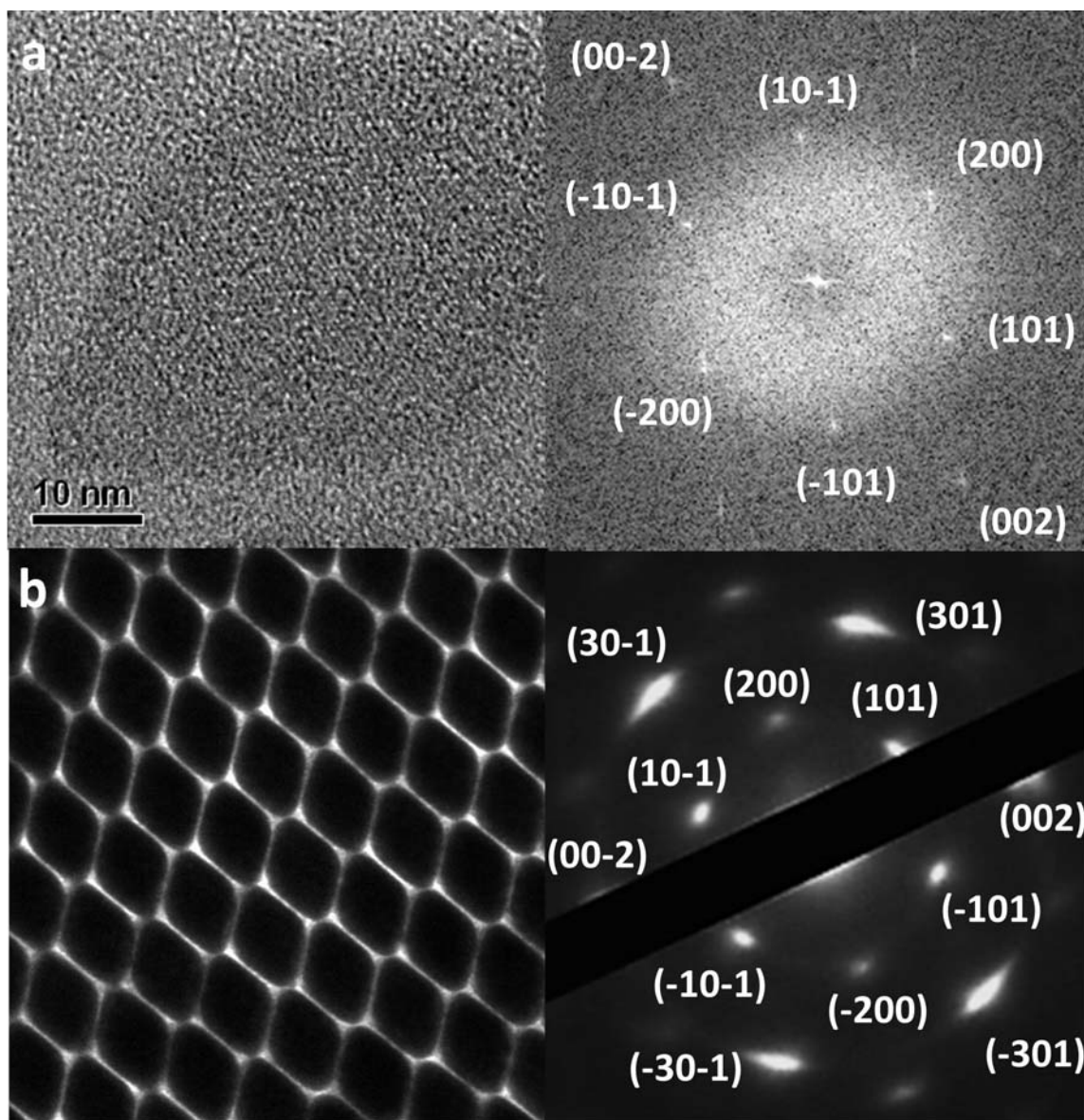
Figure 4.4. a) HRTEM image and FFT pattern of rhombic GdF$_3$ nanoplate. b) TEM image of columnar superlattice and SAED pattern.

The lamellar liquid crystalline structures of rhombic nanoplates also exhibit long-range order and characteristic single crystalline electron diffraction patterns

(Figure 4.5 and 4.6a). Due to the fact that these films form multilayered structures, scanning electron microscopy [142] images are preferential to visualize the surface structure of the nanoplates assembled edge-on (Figure 4.6b). We observe that the nanoplates are not oriented perpendicular to the substrate, but are tilted with respect to the substrate. TEM tilt analysis shows that the nanoplates in the lamellar structure also preserve translational order along the nanoplate stacks (Figure 4.6c, d). In addition to single component superlattices, binary superlattices in which plates are co-assembled with spherical nanocrystals may be formed in the lamellar liquid crystalline structure (Figure 4.6e, f). TEM images show that the long axis of each nanoplates aligns parallel to the substrate (Figure 4.6e) and that the spherical 9nm hexagonal phase sodium gadolinium tetrafluoride (β-NaGdF$_4$) nanocrystals locate in the void between the plate stacks (Figure 4.6f). This result demonstrates that the long-range order lamellar structure of rhombic nanoplates may be used as a dielectric template directing nanocrystals into periodic one-dimensional arrays.
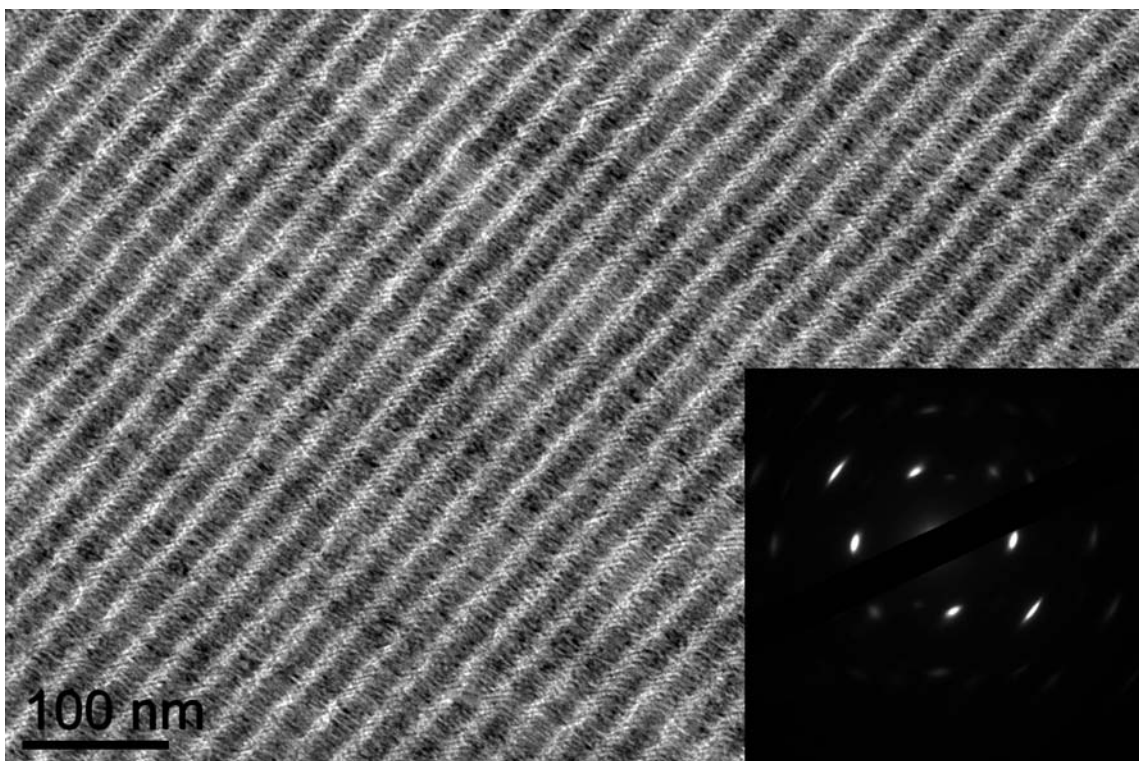
Figure 4.5. TEM image of lamellar superlattice of rhombic GdF$_3$ nanoplates. The inset shows the wide angle selected area diffraction pattern.
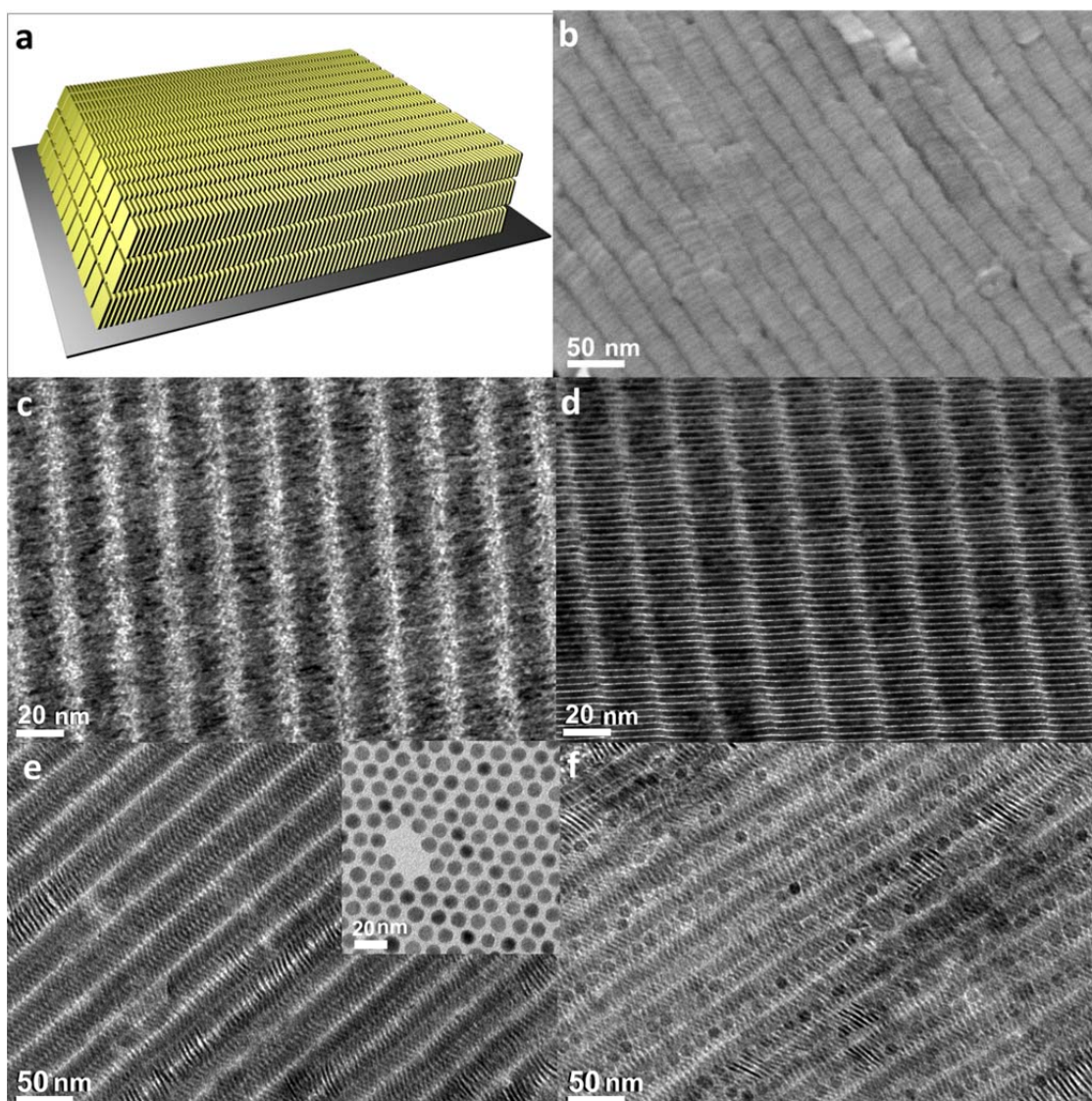
Figure 4.6. a) Schematic and b) SEM image of lamellar liquid crystalline structure of rhombic nanoplates. TEM images of laterally assembled GdF$_3$ nanoplates collected by tilting TEM holder from c) 0° to d) 53°. TEM images of e) lamellar liquid crystalline structure and f) binary superlattices with β-NaGdF$_4$ spherical nanoparticles. e inset) TEM image of β-NaGdF$_4$ spherical nanocrystals.

Sub-phases selected for liquid interfacial assembly play an important role in controlling macroscopic orientation of superlattices. To confirm a sub-phase effect, assemblies are produced with samples that have been extensively purified to remove any additional surfactant, avoiding the effects of depletion attraction or change in the surface wetting properties. Four different glycol-type sub-phases having different dielectric constant are tested to reveal the sub-phase effect. We observed that the less polar sub-phases predominantly form columnar superlattices, while more polar sub-phases tend to form lamellar superlattice structures.

The sub-phase effect suggests the assembly in this study is occurring at the liquid-liquid interface rather than the liquid-air interface as has been reported for other systems.[208-211] The sub-phase effect may suggest that the sub-phase affects the orientation of liquid crystalline superlattices due to the change of dielectric constants, because the sub-phases used for assemblies have similar values of surface tensions but vary in dielectric constant. In TEM image of columnar assembly, we observed that the superlattice is assembled from the first monolayer and extended to multilayers (Figure 4.7). Facets of nanoplates are covered by oleic acid, which makes the facets hydrophobic. Therefore, nanoplates on the first layer, which directly contact the sub-phase, could tend to stand edge-on relative to the polar sub-phase. On less polar sub-phases such as tri- and tetraethylene glycol, the nanoplates lie flat with their faces directly in contact with the sub-phase. This is similar to previously reported trends of

nanorod alignment in formation of liquid crystalline superlattices.[97,212] After formation of the first layer on the sub-phase, strong face-to-face interaction between nanoplates can induce self-ordering to overlap facets and build 3-D liquid crystalline superlattices by matching orientation of plates,[213] as displayed in Figure 4.7.

50 nm
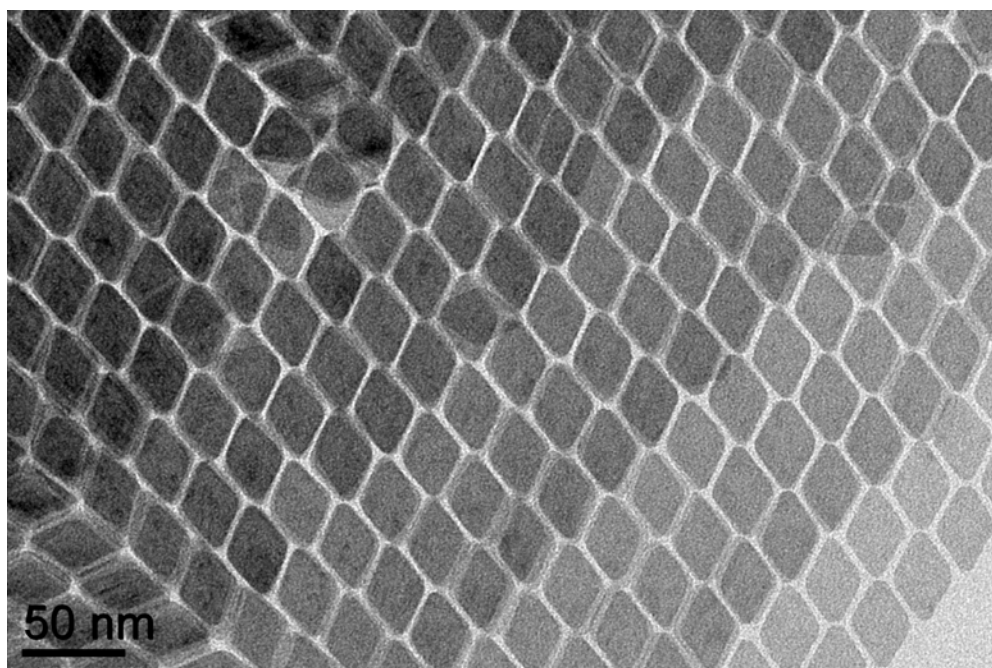
Figure 4.7. TEM image of columnar liquid crystalline assembly of rhombic GdF_3 nanoplates. Superlattice structure is extended from monolayer to multilayers.

To further understand the influence of sub-phase on superlattice formation, we perform the nanoplates assemblies without covering the solution container to

facilitate faster drying of hexane. It is known that assemblies occur on liquid-air interface rather than on liquid-liquid interface under fast drying condition.[208,209] Therefore, assemblies would not be affected by the sub-phase. We observe that domain orientations in assembled films are independent on variation of sub-phases and that the nanoplates lay flat to the substrate. This result supports that the liquid crystalline structure formed by liquid interfacial assembly can be directed by sub-phases when assemblies occurs on the sub-phases.

Phosphorescent assemblies can be fabricated by using europium (Eu^{3+}) doped GdF_3 nanoplates. A lanthanide element has a partially filled f electron inner shell that is responsible for its characteristic optical properties. Europium dopant is known as highly efficient red emitter.[33] We observed that the emission spectra of europium doped GdF_3 nanoplates are perturbed depending on the structure of the liquid crystalline superlattice films (See Table 4.1). Figure 4 shows the excitation and emission spectrum of 1% Eu^{3+} doped GdF_3 nanoplates suspended in hexanes, drop-casted onto films, and assembled into the two liquid crystalline superlattices. Characteristic Eu^{3+} red emission which is corresponding to $^5D_0 \rightarrow {}^7F_J$ line emissions (J=0, 1, 2, 3, 4) are observed in all samples. Emission spectra obtained from solution and drop-casted films are nearly identical. However, the relative intensities of the peaks contributing to the $^5D_0 \rightarrow {}^7F_1$ transition, which is a known as magnetic dipole transition, are varied depending on the structure of the assembly. The reason for structure dependent emission remains unclear. However, the effect of assembly on the optical

properties of the film indicates the importance of controlling the formation and precisely characterizing the structure of superlattices, allowing structure-property relationships to be understood and the properties of superlattices to be controlled.
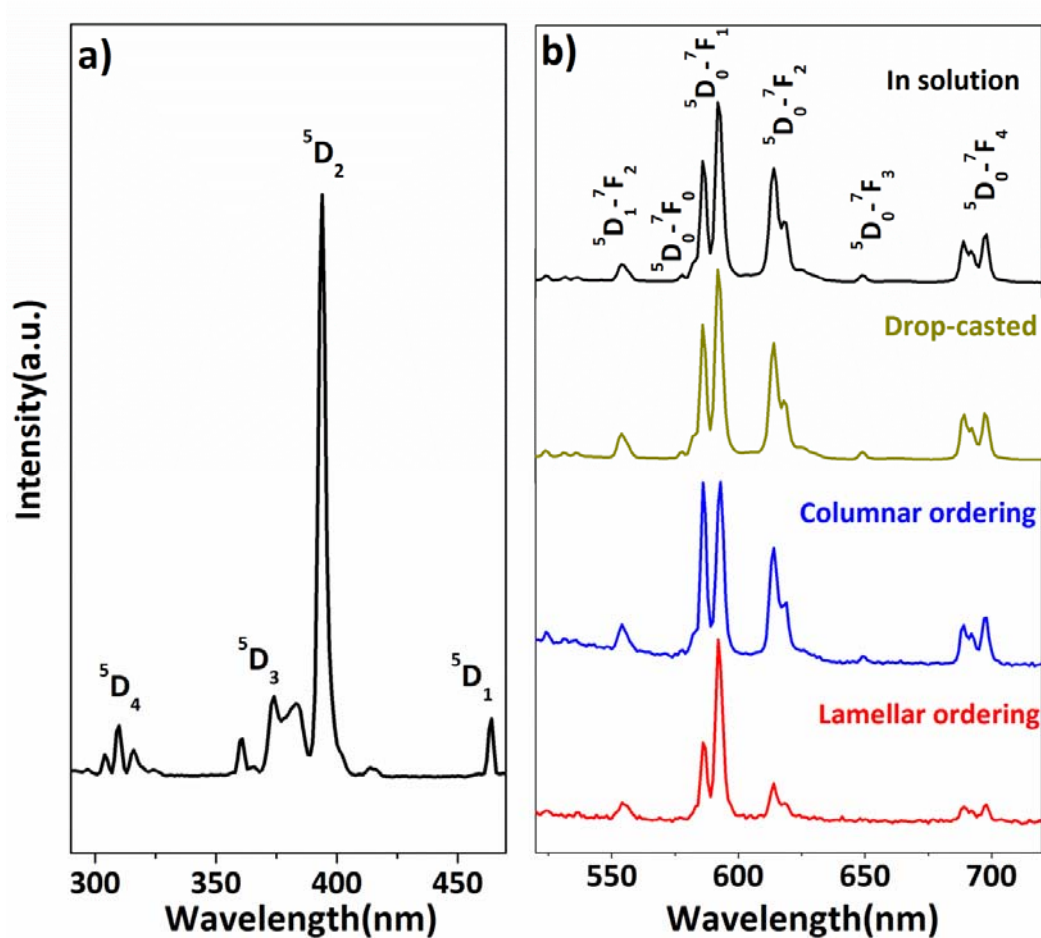
Figure 4.8. a) Excitation and b) emission spectra of 1% Eu^{3+} doped rhombic GdF_3 nanoplate in solution, in drop cast film, and liquid crystalline superlattice films measured at room temperature. Excitation wavelength is set as 394nm and emission spectra are collected at 90° with a 30° angle between light source and the sample plane (emission spectra are found to be independent of this angle). Excitation spectrum is recorded by monitoring the emission at 592nm.

	I_{554nm}/I_{586nm}	I_{586nm}/I_{586nm}	I_{592nm}/I_{586nm}	I_{614nm}/I_{586nm}
Solution	0.14	1	1.49	0.94
Drop-casted Film	0.18	1	1.58	0.80
Columnar assembly	0.15	1	0.96	0.63
Lamellar assembly	0.22	1	2.34	0.47

Table 4.1. Intensity ratio between emission peaks of 1% Eu^{3+} doped GdF_3 nanoplates in defined structures. Intensity ratio is normalized by the emission intensity at 586nm.

4.3. Characterization of Liquid Crystalline Self-Assembly of GdF_3 Nanoplates by In-plane and Out-of-plane SAXS

In this section, we introduce novel technique to characterize liquid crystalline superlattices with X-ray based measurements with a laboratory X-ray diffractometer, and analyze the sub-phase effects which directs the macroscopic orientation of liquid crystalline self-assemblies. 3-D liquid crystalline superlattices are investigated using reflection small-angle X-ray scattering (RSAXS) and in-

plane small-angle X-ray scattering (in-plane SAXS) measurements on a laboratory X-ray diffractometer equipped with a graded multilayer mirror. The parabolically curved graded multilayer mirror converts the divergent X-ray beam generated from a point source into a parallel beam. This allows a laboratory diffractometers to be used in reflectometry, grazing-incidence, and high-resolution diffractometry with significant improvements in the X-ray intensity.[214] In the RSAXS measurement, X-ray beam scatters off the nanocrystal film on substrate as illustrated in Figure 4.9a and scattered beam is collected in theta/2-theta ($\theta/2\theta$) geometry. An off-set scan ($\theta+\delta\theta/2\theta$) is performed to avoid strong specular reflection.[215] Bragg diffraction patterns obtained from RSAXS measurements indicate out-of-plane ordering. On the other hand, in-plane SAXS measurements utilize a grazing incident geometry (α_i) and scattered beam is collected by a scanning detector in a plane parallel to the film surface, as described in Figure 4.9b. In-plane SAXS provides scattering information about in-plane ordering. Therefore, the two scattering measurements are complimentary and provide precise structural information to confirm the orientation of the liquid crystalline assemblies.
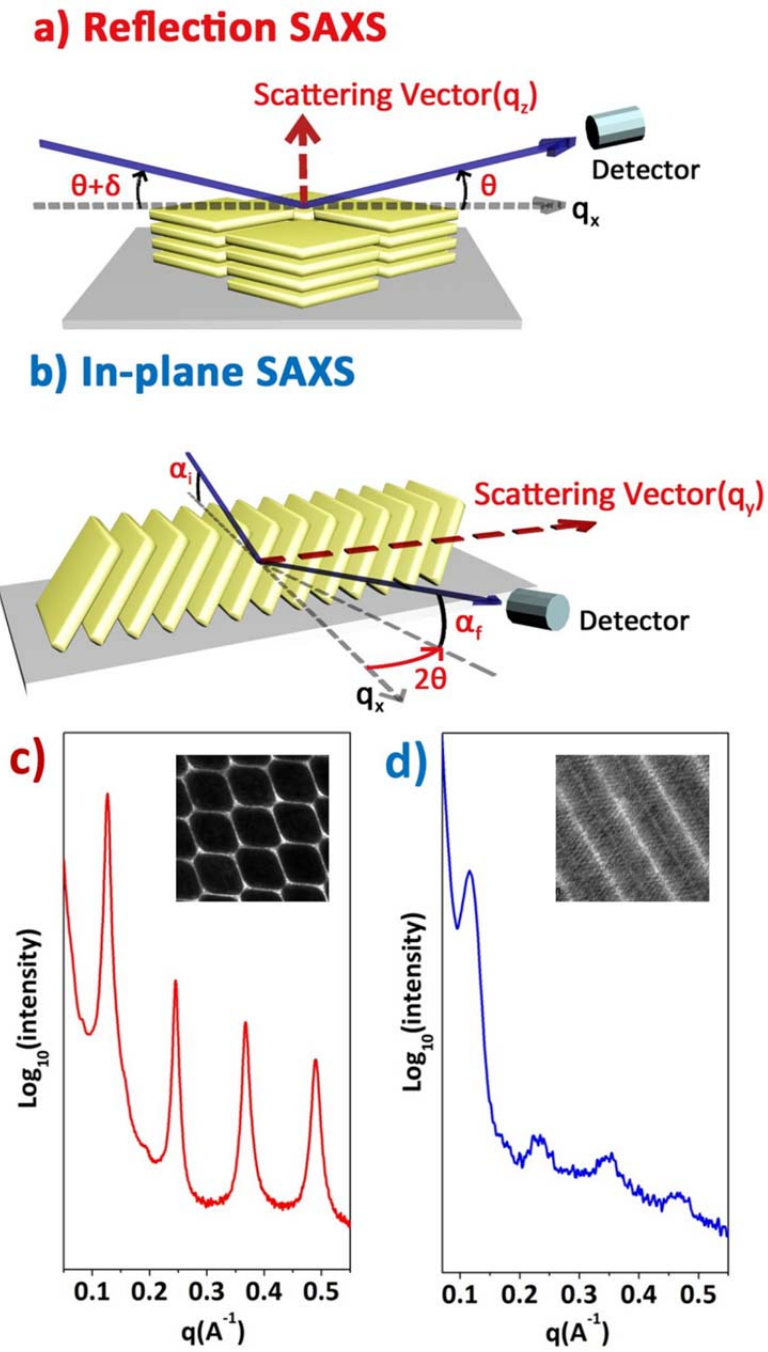
Figure 4.9. Schematics of a small-angle X-ray scattering experiment. a) RSAXS,

b) In-plane SAXS, and c) RSAXS patterns showing fringe patterns corresponding

to columnar assembly, d) In-plane SAXS result indicating to lamellar assembly.

Figure 4.9c and d show RSAXS and in-plane SAXS results for assemblies of rhombic nanoplates made by liquid interfacial assembly using diethylene glycol as the sub-phase. Periodicity in the RSAXS and in-plane SAXS patterns indicate that columnar and lamellar phases coexist in the assembled structure. In RSAXS measurements, up to 9th order of Bragg diffractions are observed with equal spacing that is the result of scattering from the face-to-face ordering of the nanoplates (Figure 4.10a). High order diffractions indicate that long-range translational order exists within the nanoplate stacks. Peak broadening in SAXS patterns reflects the average domain size of the assembled structure, and an average grain size is calculated using the Scherrer equation.[102,216] SAXS patterns of assembled films are much narrower than those of drop-cast films and are limited by instrumental broadening (Figure 4.9a and b), indicating that more extensive long range order is obtained from liquid interfacial assembly. The average domain size of out-of-plane ordering in columnar assemblies is approximately 0.1 μm, which corresponds to the assembly of 20 nanoplates.
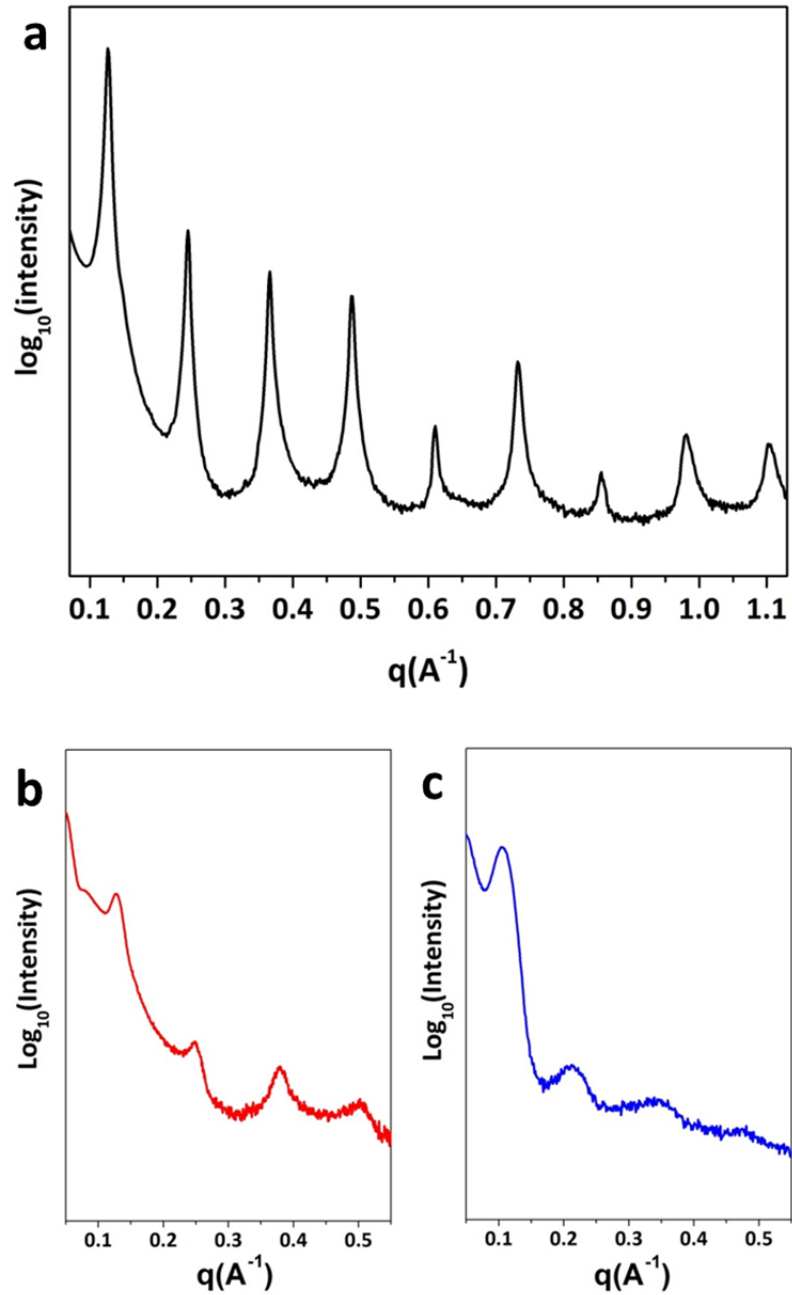
Figure 4.10. a) High order RSAXS patterns of columnar liquid crystalline superlattice on SiO₂/Si wafer. b) RSAXS and c) in-plane SAXS patterns of drop-casted films on SiO₂/Si wafer.

The scattering angles of the peaks in the SAXS pattern are used to determine the average inter-particle spacing, where the center-to-center distance between nearest neighbors in the nanoplate stacks is given by $d=2\pi/q$. In RSAXS, the position of first diffraction peak is $0.127(A^{-1})$ which corresponds to a 4.9nm of center-to-center distance. Average inter-particle spacing is obtained by subtracting the nanoplate thickness from center-to-center distance. The thickness of rhombic nanoplate as calculated by X-ray simulation is 2.4nm, therefore, the average inter-particle spacing in columnar assembled nanoplates is 2.5nm. Recently, Shevchenko *et al.* reported GISAXS results for 7nm PbS spherical nanocrystal superlattices.[217] The inter-particle spacing of the closed-packed structure was found to be 1.4 nm, which is shorter than those of our columnar assembly. It might be expected that edge of nanoplates in each columnar stack are intercalated into the void between nanoplates in next stacks and increase inter-particle spacing. On the other hand, the position of first diffraction peak from in-plane SAXS is $0.115(A^{-1})$ and the lattice spacing in lamellar ordering is 5.5 nm. As described earlier, nanoplates in lamellar assemblies do not lie perpendicular to the substrate, but are tilted at an angle of around 50° as measured by TEM tilting analysis (Figure 4.6c, d). Longer lattice spacing between nanoplates in the lamellar structure may be attributed to the tilt of the nanoplates.
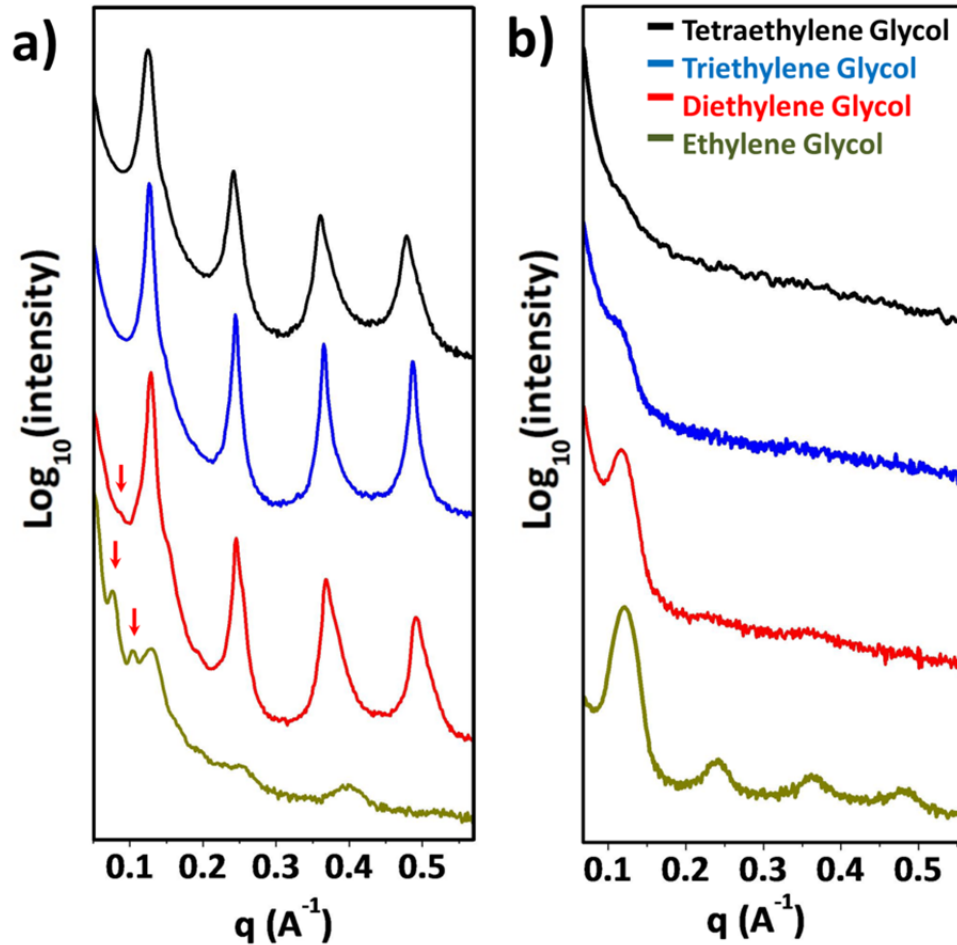
Figure 4.11. a) Reflection SAXS and b) in-plane SAXS measurements of rhombic GdF_3 nanoplate superlattices assembled by liquid interfacial assembly over different sub-phases. Red arrows indicate diffraction peaks corresponding to 2-D layers ordering of lamellar superlattices.

RSAXS and in-plane SAXS measurements confirm the trend observed with macroscopic orientation of superlattice (Figure 4.11) Periodic Bragg peaks in RSAXS are observed on films made over tetraethylene glycol and triethylene

glycol sub-phases. However, in-plane SAXS did not show any characteristic diffraction peaks. This suggests that tetraethylene glycol and triethylene glycol sub-phases selectively induce the formation of columnar liquid crystalline superlattices as was corroborated by our TEM studies. For ethylene glycol, which has higher dielectric constant than tri or tetra ethylene glycol, in-plane SAXS result shows Bragg peaks, while the intensities of Bragg reflections in RSAXS are weaker relative to those of films assembled over less polar sub-phases. Laterally ordered nanoplates are tilted with respect to the surface. Therefore, out-of-plane order of tilted nanoplate stacks could contribute to produce Bragg diffraction patterns in RSAXS measurement. Multi-layers of the 2-D lamellar structure also produce Bragg peaks in the region smaller than the first scattering peak of face-to-face ordering (Figure 4.11, red arrows). The RSAXS pattern of assembled films over ethylene glycol clearly shows the Bragg reflections due to layer by layer ordering. Results from both RSAXS and in-plane SAXS reveal that lamellar structure is predominant in films assembled over ethylene glycol sub-phase. Therefore, the less polar sub-phases predominantly form columnar superlattices, while more polar sub-phases tend to form lamellar superlattice structures.

4.4. Shape-Directed Hierarchical Self-Assembly of Gd_2O_3 Nanoplates

In this section, we present that highly uniform Gd_2O_3 nanoplates are self-assembled into nanofibril-like liquid crystalline superlattices with long range

orientational and positional order. In addition, shape-directed hierarchical self-assemblies are investigated by tailoring the aspect ratio of the arms of the Gd_2O_3 nanoplates. Due to the uniformity of the Gd_2O_3 nanoplates, self-assembly occurs to form 1-D nanofibril-like structures with long-range order (Figure 4.12). All of the tripodal nanoplates that assemble into 1-D superlattices sit with two arms toward the substrate and one arm directed away from the substrate. The arms of the tripods align in perfect registry, which maximizes the interaction between nanoplates and forms a 1-dimensional superlattice with an eclipsed conformation (Figure 4.12a). This structure is clearly visible in the scanning electron microscopy [142] images (Figure 4.12b).
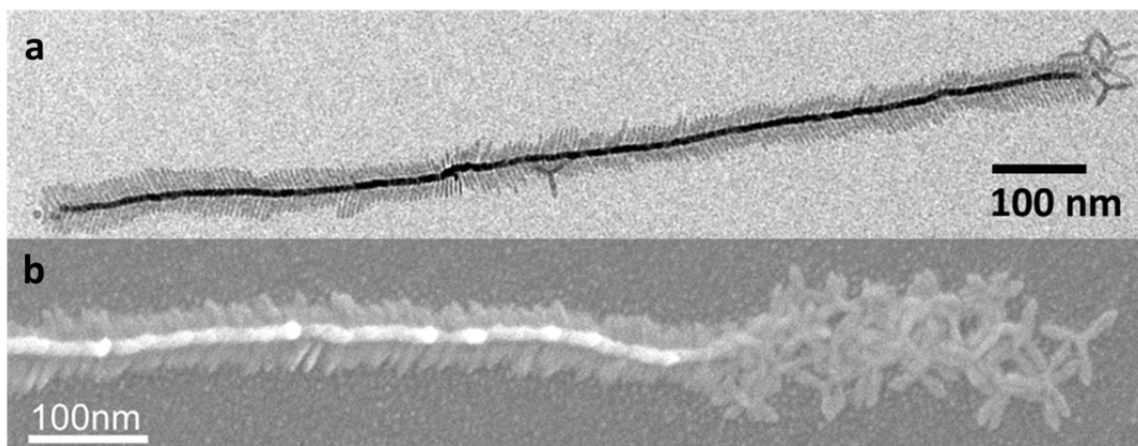
Figure 4.12. Microscopic images of shape-directed self-assembly of Gd$_2$O$_3$ nanoplates a) TEM and b) SEM of one-dimensional self-assembly of tripodal nanoplates with eclipsed conformation. Scale bar is 100 nm.

1-D nanofibril structures can be further aligned (bundled) together to form an extended ordered superstructure,(Figure 4.13a-c) which is commonly observed in the process of biomaterial formation. The size and shape uniformity of nanoplates allows us to demonstrate shape-directed, self-assembly by tailoring the aspect ratio of arms of Gd$_2$O$_3$ nanoplates. In the case of tripodal nanoplates, nanofibril superlattices are organized into hierarchical superstructures. Each 1-dimensional string (or nanofibril) is formed from the alignment of the constituent nanoplates and these strings are bundled alternately into a superstructure by forming one string with two arms laying on the substrate and the inverted string with one arm contacting the substrate (Figure 4.13c, inset). For the shape intermediate between the tripodal and triangular nanoplate with decreasing the

aspect ratio of arms, two 1-dimensional nanofibril structures tend to self-assemble through tip to tip contact of two arms (Figure 4.13d). Pure triangular nanoplates are ordered into columnar (Figure 4.13e) and lamellar (Figure 4.13f) liquid crystalline superlattices by tiling of the building blocks. Assembled superlattices of tripodal nanoplates contain free space between the two inverted nano-fibril structures, forming an open framework that is analogous to mesoporous structures. On the other hand, triangular nanoplates tend to be packed more efficiently, leaving minimal space except for the surface ligands.
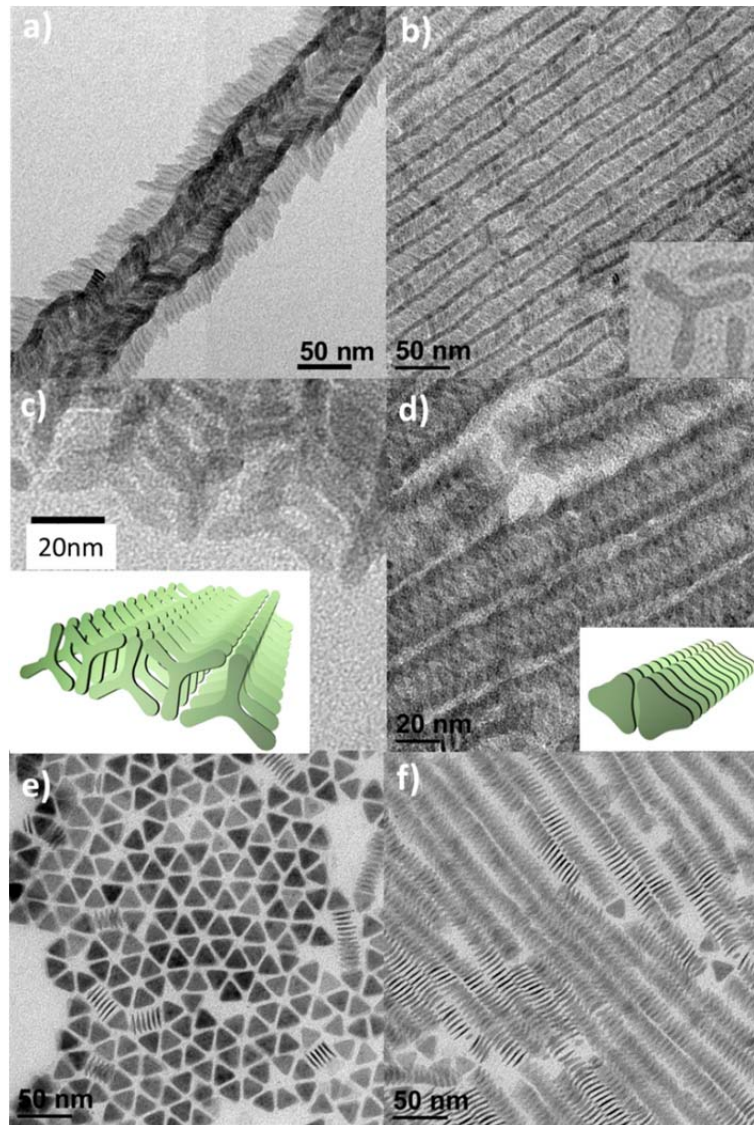
Figure 4.13. Microscopic images of a) Hierarchical self-assembled structure composed of three nanofibril structures, b) Two-dimensional self-assembly and c) high magnification TEM of two-dimensional self-assembly of tripodal nanoplate. Inset is a schematic model of the ordered structure. d) Liquid crystalline self-assembly of tripodal nanoplates of smaller aspect ratio. Inset is a schematic model of the ordered structure. Self-assemblies of triangular nanoplates into e) columnar, and f) lamellar liquid crystalline superlattices.

4.5. Shape-Directed Binary Assembly of Anisotropic Nanoplates: a Nanocrystal Puzzle with Shape-Complementary Building Blocks

Here, we present the binary self-assembly of highly uniform gadolinium trifluoride (GdF_3) rhombic nanoplates and gadolinium oxide (Gd_2O) tripodal nanoplates. These two anisotropic nanoplate building blocks were pre-designed to be complementary, such that they may be assembled into the predictable binary structures *via* a shape-specific directional interaction, similar to the tiling of puzzles. We observe grain sizes for these binary superlattices which extend over micrometer scales, while preserving long-range orientational and positional order.

Figure 4.14a and 4.14b shows transmission electron microscopy [140] images of GdF_3 and Gd_2O_3 nanoplate building blocks, respectively, synthesized by the previously reported methods.[172,173] GdF_3 forms rhombic nanoplates with an orthorhombic structure (JCPDS no. 49-1804). The nanoplates are enclosed by (010) plane with the b-axis as the direction of thickness and the side edges are assigned as the four (101) planes, as confirmed by the powder X-ray diffraction and the X-ray simulation conducted using the Debye formula.[172] The angle between the two (101) planes are calculated as 67.5^o and 112.5^o from the orthorhombic unit cell and lattice constants, which matches with the angles measured from the electron microscopy images.(Figure 4.14a) TEM images indicate that rhombic nanoplates are 24 nm along the base edge, 20 nm along

the height of rhombic plate, and 34 nm along the long axis.(Figure 4.15a) The other building block, a tripodal Gd_2O_3 nanoplate, shows three-fold symmetry, with 23 nm in arm length, 7 nm in the width of each arm, and a thickness of 2 nm on average.(Figure 4.14b, 4.15b) The tip to tip length is about 35 nm with 120° angle between arms. The dimensions of the tripodal nanoplates are optimumized for complementary assembly with rhombic nanoplates.
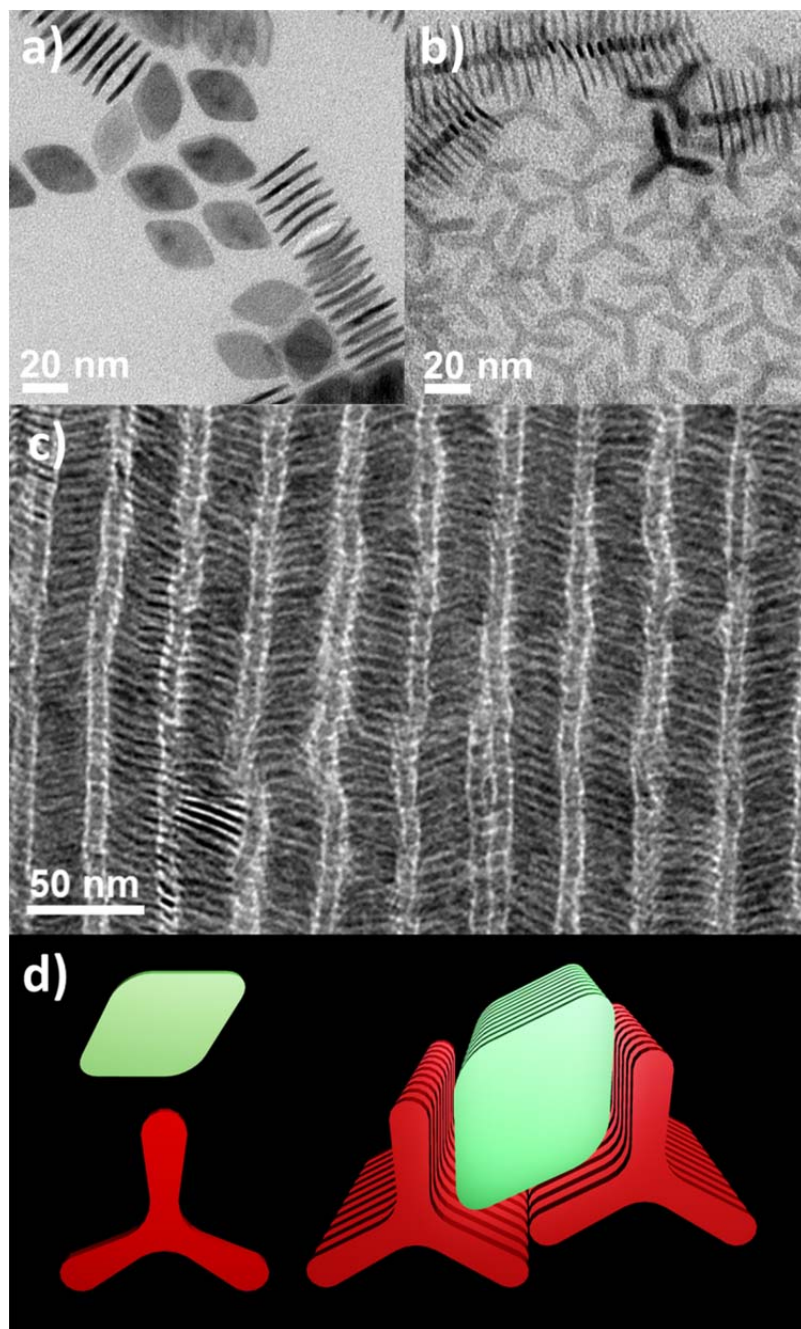
Figure 4.14. TEM images of nanoplate building blocks. a) Gd_2O_3 tripodal nanoplates, b) GdF_3 rhombic nanoplates, and c) a binary self-assembly of tripodal and rhomic nanoplates formed *via* complementary-shape interaction. d) Schematics of rhombic, tripodal nanoplates and binary assembly.
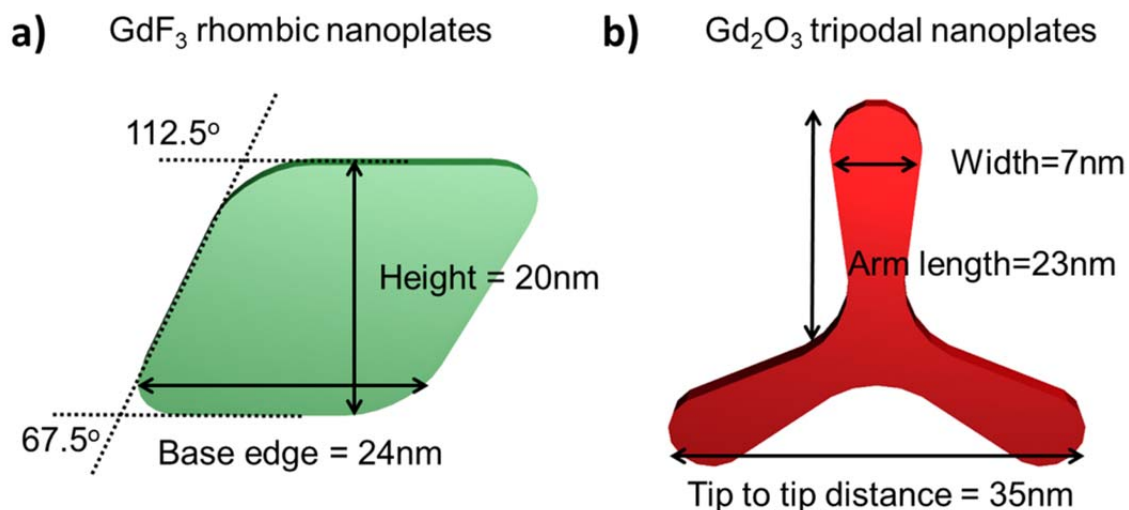
Figure 4.15. Schematics of a) GdF$_3$ rhombic nanoplate and b) Gd$_2$O$_3$ tripodal nanoplates.

Self-assembled structures are formed by liquid interfacial assembly technique using diethylene glycol as a sub-phase.[189] Figure 4.14c displays a TEM image of a binary superlattice in which rhombic nanoplates are co-assembled with tripodal nanoplates. Both nanoplates self-assemble into one-dimensional arrays by face to face stacking. The flat surface of the nanoplates enables maximizing the surface-surface interactions resulting in the preferential, unidirectional aggregation of nanoplates.[218] Unlike single component lamellar, liquid crystalline superlattices self-assembled with GdF$_3$ nanoplates, it is observed that another string of particles locates between the 1-D arrays of rhombic nanoplates in the binary superlattice.(Figure 4.14c) The width of this string of particles is about 7 nm on average, which is equivalent to the width of the arms of the self-assembled Gd$_2$O$_3$ tripodal nanoplates. The alternating

sequence of two different types of strings in the self-assembled structure extends in two-dimensions to form binary lamellar structures with hierarchical complexity. In some regions of the superlattice films, lamellar arrays of GdF_3 single component assemblies co-exist with binary superlattices.(Figure 4.16a) Center to center distances between rhombic nanoplates are about 25 nm in single component assembly and about 37 nm in binary superlattice, on average. An increase of inter-lamellar spacing in binary superlattices further confirms the periodic inclusion of one arm of the tripodal nanoplates between lamellar arrays of rhombic nanoplates.

Careful analysis of a fractured binary superlattice membrane allows for visualization of both nanoplate components and their self-assembled configuration.(Figure 4.16b) Tripodal and rhombic nanoplates in the fractured region lie flat on the substrate, enabling the possible configuration of two components to be imaged. Indeed, it is clearly observed that the clusters (groupings of nanocrystals) are co-assemblies of two tripodal nanoplates and one rhombic nanoplate *via* shape complementarity. (Figure 4.16b circles) In addition, the analysis of 1-D rhombic nanoplate arrays at the crack edge reveal that rhombic nanoplates in the assembled 1-D strings stand with one edge perpendicular to the substrate. The width of the 1-D arrays of GdF_3 assembly in the binary superlattices is about 20 nm, which is close to the edge to edge distance of the rhombic plates. This further indicates that the rhombic nanoplates stand upright between tripodal nanoplates, as depicted in figure 4.14d. Within

individual 1-D strings of rhombic and tripodal nanoplates, each of the building blocks is self-assembled exclusively into single component arrays through shape-segregated face to face interactions, without the observation of tripod-rhombus binding. This preferential alignment may suggest that the facet-specific interactions between identical types of nanoplates may play an important role in promoting the formation of self-assembled binary assemblies.
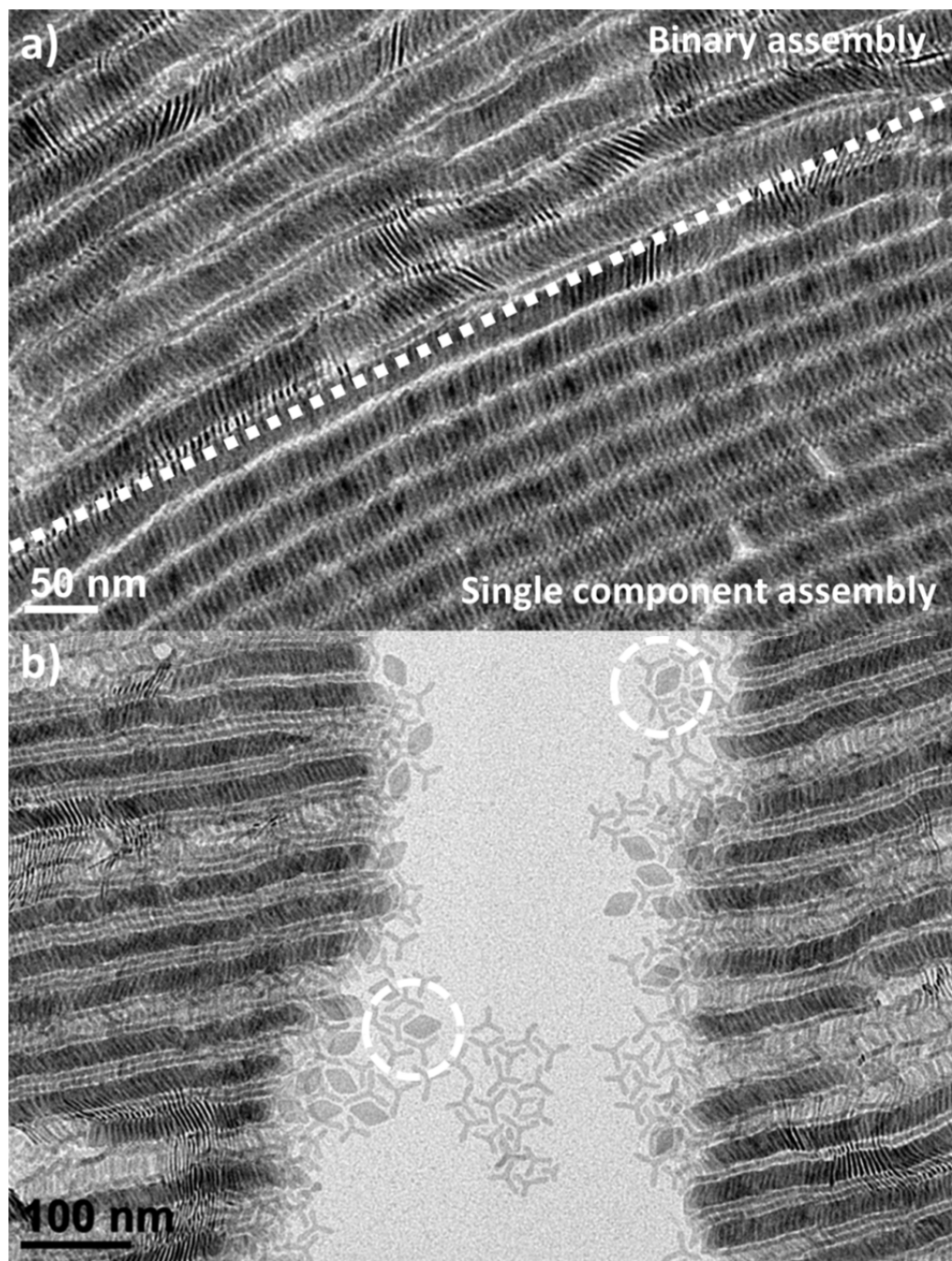
Figure 4.16. TEM images of a) a binary superlattice domain bordering a single component superlattice domain of rhombic nanoplates and b) a fractured binary superlattice consisting of co-assembled tripodal and rhombic nanoplates.

In order to further characterize the structure of the binary assemblies of nanoplates, we performed a TEM tilt-series analysis on single and binary superlattices using a dual-axis tomography TEM holder. Due to the fact that the nanoplates in assembled structures are tilted with respect to the substrate,[172] the thicknesses and edges of the stacked nanoplates in single and binary superlattices can be visualized by tilting the assembled films. Figure 3 displays TEM images taken at normal projection(Figure 4.17a-c) and tilted 55° in plane.(Figure 4.17d-f) The TEM tilting experiments reveal orientational and positional order in the binary assemblies of tripodal and rhombic nanoplates, close to the level observed in single component assemblies.

In the single component assemblies, all nanoplates are oriented into the same crystallographic direction due to the perfect shape registry between nanoplates, which is corroborated by single crystalline wide-angle selected area electron diffraction (SAED) patterns.(Figure 4.17, inset) In the binary superlattices, the diffraction peaks are more diffused than those of single component assemblies, which we attributed to the fact that the position and orientation of nanoplates are likely more relaxed in the complex binary structure than in single component superlattices. However, single crystal electron diffraction patterns of each component are still preserved in the wide-angle SAED pattern of binary superlattices, indicating that each nanoplate building block is crystallographically aligned into the same direction, even in the binary superlattices. Although it is hard to precisely define the zone axis due to the

anisotropic shape of nanocrystals and the complex architecture of superlattices, the electron diffraction patterns still provide additional structural information regarding the self-assembled membrane. In the SAED patterns of tilted binary superlattice presented in Figure 4.18f, diffraction spots were indexed as {020}, {131}, and {111} families of planes of GdF_3 nanoplates and {222} and {220} families of planes of Gd_2O_3 nanoplates. These indexes, d-spacing, and angles between planes are in reasonable agreement with the simulated single crystalline electron diffraction pattern generated from each single crystal which are oriented along the same crystallographic direction of nanoplates in the binary structure. This indicates that the crystallographic orientations of each unit cells are registered as the self-assembled conformation as depicted in Figure 4.14d.
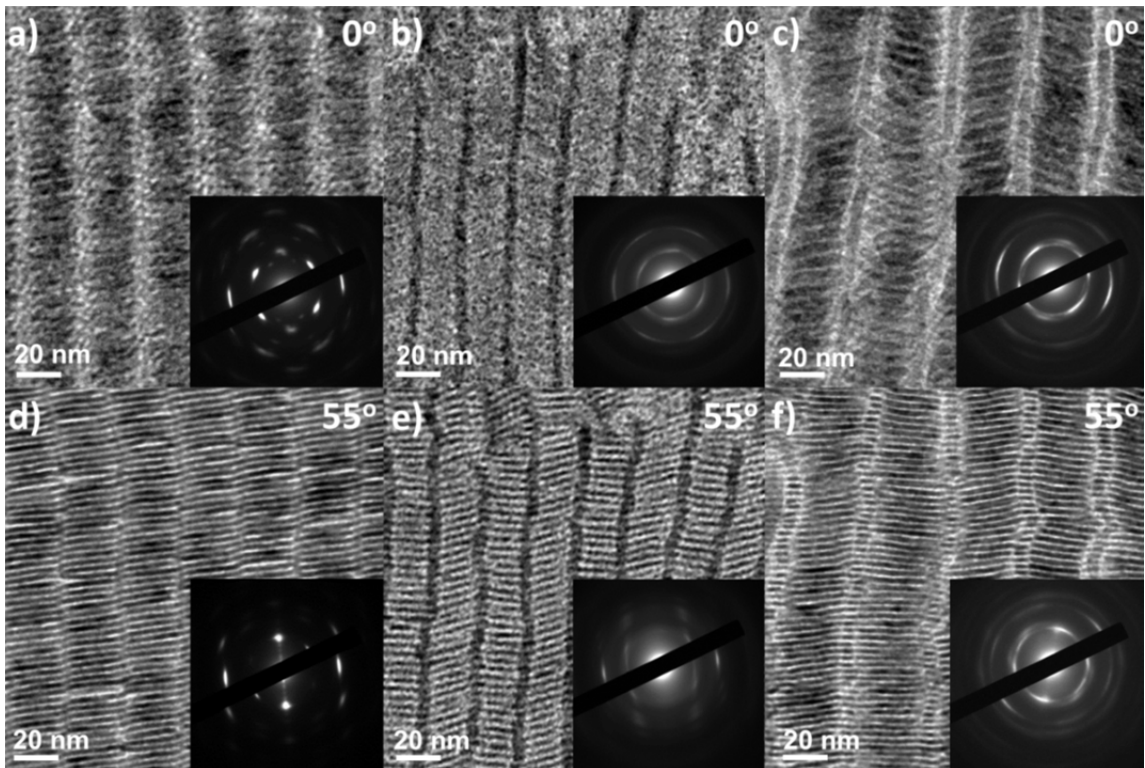
Figure 4.17. TEM images of the a) GdF_3, b) Gd_2O_3 single components, c) binary superlattices, and d, e, f) 55° tilted images respectively. Insets are wide-angle selected area electron diffraction patterns.

Binary superlattice structures with long range orientational and positional order are observed over large areas. Figure 4.18 shows low-magnification TEM and SEM images of the binary superlattices. The lengths of the assembled structures can reach the micrometer scale with preservation of the binary ordering, as shown in high magnification SEM image.(an inset of Figure 4.18) This indicates the potential of utilizing the shape-complementary interaction

between building blocks to fabricate large area self-assembled nanocrystal membranes.
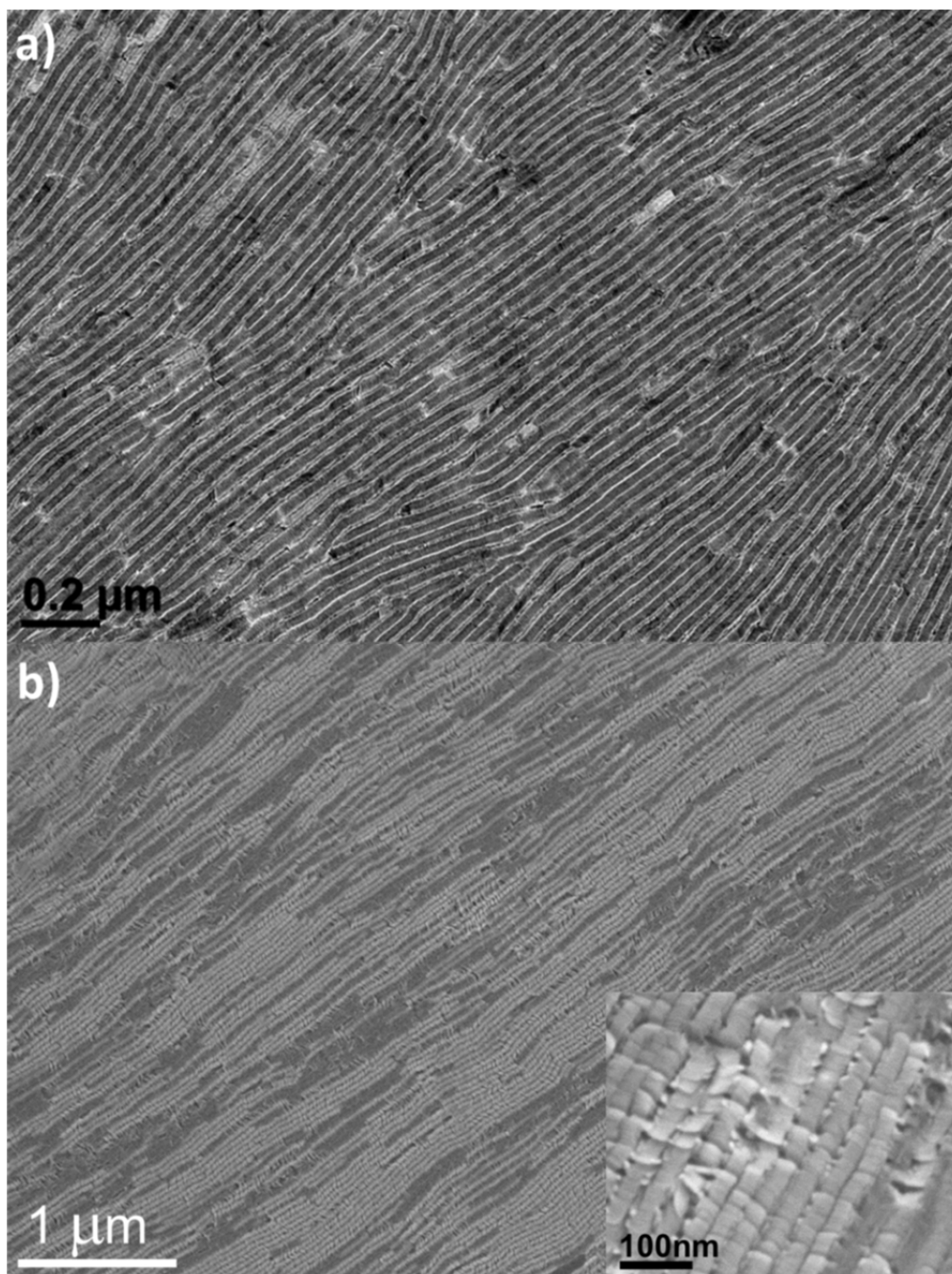
Figure 4.18. a) Low magnification TEM images and b) SEM image of binary superlattice co-assembled with tripodal and rhombic nanoplates. Inset is the high magnification SEM image.

4.6. Liquid Crystalline Binary Self-Assembly of Colloidal Nanorods and Nanoplates.

In this section, we present co-assembly of colloidal nanorods and nanoplates into binary liquid crystalline superlattices. Liquid crystalline self-assembly of anisotropic nanoplates is a promising template to control the orientation of other nanocrystal building blocks due to their long range orientational and positional order and potential to control the orientation. This work demonstrates that the liquid crystalline superlattice of nanoplates can be used to direct the position and orientation of colloidal one-dimensional nanorods with long range order when they are co-assembled *via* liquid interfacial assembly.

Colloidal lanthanum trifluoride (LaF_3) nanoplates are used as transparent dielectric nanocrystal building blocks for the self-assembly. LaF_3 nanoplates are synthesized by the same method to synthesize GdF_3 nanoplates. Figure 4.19a is TEM image of LaF_3 nanoplates. The diameter of nanoplates is about 23 nm with 2 nm of thickness. Nearly monodisperse nanoplates lay parallel to the substrates and self-assembled into 2-dimensional hexagonal array. Colloidal CdSe/CdS dot-in-rods is synthesized by seeded growth method reported previously.[219] The size of CdSe seeds is about 3nm with pseudo-spherical morphology. Upon shell formation, CdS preferentially along the *c*-axis of the hexagonal wurtzite CdS crystal, yielding a nanorod morphology. Figure 4.19b is a TEM image of the

CdSe/CdS nanorods. The length of nanorods is about 13nm with 3.5nm of diameter.
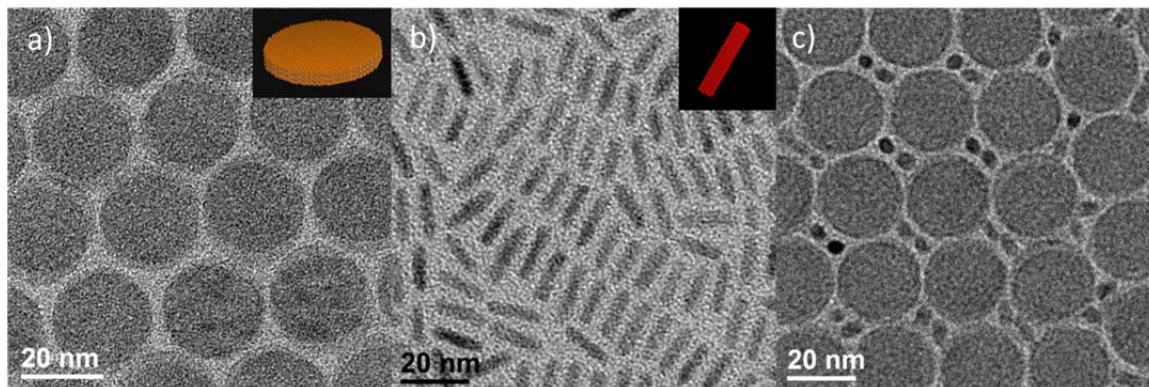
Figure 4.19. TEM and images of anisotropic nanocrystal building blocks used for self-assembly a) LaF$_3$ nanoplates and b) CdSe/CdS core-shell nanorods and c) binary superlattice self-assembled by liquid interfacial assembly.

Self-assembly of LaF$_3$ nanoplates and CdSe/CdS nanorods is performed by liquid interfacial assembly using glycol-type polar sub-phases. Figure 4.19c is a TEM image of a binary superlattice of the LaF$_3$ nanoplates. and the CdSe/CdS nanorods co-assembled on a diethylene glycol surface. The nanoplates are stacked along out-of-plane direction to form columns and two vertically aligned nanorods are located between stacked columns with long axis of the nanorods pointing upward. In most cases, two nanorods are included in four-fold symmetric vacancy positions of the nanoplate columns. Due to the inclusion, their 2-

dimensional symmetry of self-assembled LaF_3 nanoplates, which is hexagonal array in single component assemblies (Figure 4.19a), is elongated to tetragonal symmetry in the binary superlattice.(Figure 4.19c) Figure 4.21a displays the low magnification TEM image. It Most of nanorods are vertically aligned in the columnar liquid crystalline superlattice, although some form a close-packed nanoplates assembly
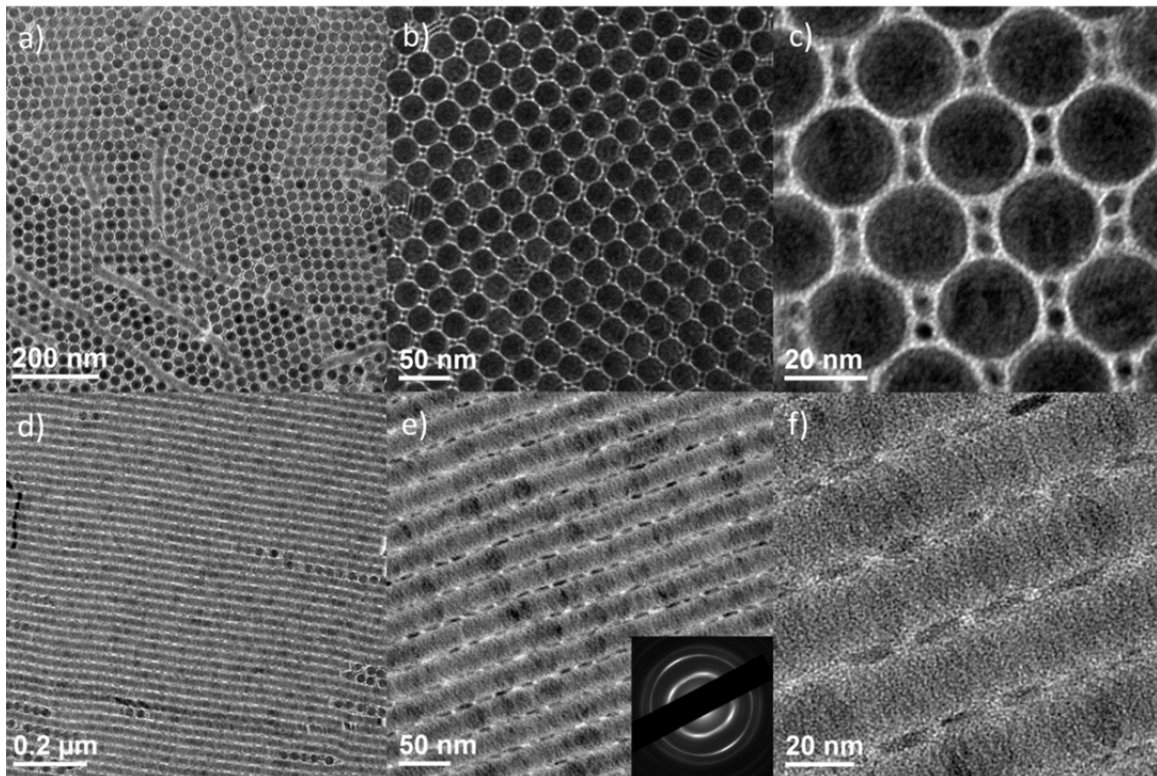
Figure 4.20. TEM images of binary superlattices of CdSe/CdS nanorods and LaF_3 nanoplates into a), b), c) columnar binary liquid crystalline structures d), e), f) lamellar binary liquid crystalline structures.

133

When ethylene glycol is used as a sub-phase for self-assembly, nanoplates stand edge-on on the substrates and stack to form one-dimensional strings by face-to-face interactions. These strings are simultaneously self-assembled into extended two-dimensional arrays to form smectic liquid crystalline structures.(Figure 4.20d-f) Colloidal nanorods are co-assembled into the liquid crystalline binary lattices with the nanorod long axes lying parallel to the substrates. The trench formed between the arrays of columnar nanoplate strings provides a free space to secure the nanorods and direct the orientation and position of the nanorods. The tip to tip distances between the nanorods in the trench are about 3nm,(Figure 4.20f) which indicates that the nanorods are highly close-packed into the one-dimensional arrays leaving a minimal space except for the surface ligands. In addition, long range positional and orientational order of smectic liquid crystalline structures allows the orientation of nanorods to be well controlled over 1 μm^2 areas.(Figure 4.20c) Since the size of LaF$_3$ nanoplates is nearly monodisperse, the distance between one-dimensionally aligned nanorods with neighboring nanorods are also uniformly controlled in the binary lattices.

4.7. Conclusion

In summary, we have demonstrated the formation of liquid crystalline superlattices consisting of one or two set of anisotropic building blocks. Columnar and lamellar liquid crystalline superlattices of GdF$_3$ nanoplates are achieved by liquid interfacial assembly with long range orientational and positional order. The

choice of sub-phase is found to be an important factor in directing the orientation of the superlattices, where more polar sub-phase favors lamellar liquid crystalline structure, and less-polar sub-phase favors columnar liquid crystalline assemblies of GdF_3 nanoplates. The structure was characterized by RSAXS and in-plane SAXS using a laboratory X-ray diffractometer. Characteristic fringe scattering patterns in RSAXS and in-plane SAXS confirms this sub-phases effect. Highly uniform tripodal Gd_2O_3 nanoplates self-assembled into 1-D nanofibril-like superlattices. In addition, the nanofibril structures can be further assembled into hierarchical liquid crystalline superstructures and shape-directed self-assemblies are investigated by tailoring the aspect ratio of the arms of the Gd_2O_3 nanoplates. At last, we present the formation of binary superlattices consisting of two anisotropic building blocks. We synthesized building blocks with complementary shape to guide the position of nanoplate building blocks, inducing the shape-directed self-assembly over micrometer scales. Many synthetic methods are available to tune the size and shape of anisotropic nanocrystals with a variety of compositions.[27,159,220] Shape directed self-assembly of anisotropic building blocks may provide a unique design rule to direct the formation of liquid crystalline single and binary nsuperlattices with high complexity in a predictable way.

4.8. Experimental Session

Materials. All chemicals are used as purchased without any further purification. Gadolinium(III) oxide (99.99%), lithium fluoride (99.99%), lithium hydroxide

monohydrate (99.95%), oleic acid (technical grade, 90%), oleylamine (technical grade, 70%), 1-octadecene (technical grade, 90%), are purchased from Sigma Aldrich. Gadolinium acetate and gadolinium trifluoroacetate precursors are prepared by refluxing gadolinium oxide in acetic acid/water and trifluoroacetic acid/water mixture (50 vol%), respectively.

Synthesis of GdF$_3$ Nanoplates. GdF$_3$ nanoplates were synthesized according to the procedure previously reported.[172] Briefly, gadolinium trifluoroacetate(2 mmol) and lithium fluoride(6 mmol) were added to a 125 mL three-neck flask containing 30 mL of oleic acid and 30 mL of 1-octadecene. This solution was degassed at 125°C for 1 h. Then, the solution was heated to 290°C under N$_2$ environment at a rate of 10°C/min and maintained at this temperature for 4 hours. Purification was conducted by adding excess ethanol and centrifugation at 4000rpm for 2 min. GdF$_3$ nanoplates were redissolved in hexane. Residual lithium fluoride, which is insoluble in nonpolar solvents, was simply removed by centrifugation at 3000 rpm for 2 min.

Synthesis of Gd$_2$O$_3$ nanoplates Gd$_2$O$_3$ nanoplates were synthesized according to the procedure previously reported.[173] Lithium hydroxide (6 mmol) is added into a mixture of 12 mL of oleic acid, 18 mL of oleylamine, and 30 mL of 1-octadecene solvent and is heated to 110 ^{o}C. After evacuation at 110°C for one hour to remove water, gadolinium acetate (3 mmol) is added and the solution is evacuated for an extra hour at the same temperature. Then, the reaction solution is heated to 300°C and maintain at this temperature for an hour under high N$_2$ blowing. Then, the reaction solution is cooled to room temperature through

addition of toluene. Purification is conducted through addition of excess methanol and centrifuging at 3000 rpm for 2 minutes.

Liquid crystalline assembly of binary superlattices. Liquid interfacial assembly is conducted according to the procedure previously reported.[189] Teflon well is filled with diethylene glycol sub-phases. Then, 30 L of the nanoplates solution (overall nanocrystal concentration is about 20mg/ml) is added on top of the surface of sub-phase. The Teflon well is covered with a glass slide to allow the slow drying of hexane. Once the nanoplate membrane is formed, films are transferred to carbon coated TEM grids for microscopic analysis

Structure characterization. TEM images and electron diffraction patterns are recorded using JEM-1400 microscope equipped with a SC1000 ORIUS CCD camera operating at 120 kV. Scanning electron microscopy [142] was performed on a JEOL 7500F HRSEM. The simulated diffraction patterns were obtained by generating the atomistic unit cell in CrystalMaker (CrystalMaker Software Ltd.), rotating the unit cell to be oriented corresponding to the crystallographic axis of each nanoplate in binary superlattice, and obtaining single crystalline electron diffraction patterns with Single Crystal software(CrystalMaker Software Ltd.).

Small-angle X-ray characterization RSAXS, in-plane SAXS, and powder X-ray diffraction are measured using a Rigaku Smartlab high resolution diffractometer equipped with a 2.2 kW sealed tube generator. The X-ray beam (Cu Kα radiation, λ=1.54056Å) is collimated as a parallel beam by parabolically curved multilayer mirrors placed in front of the sample. The beam dimension is 0.05 mm x 5 mm

(height x width) for both measurements. The offset angle is obtained by performing a series of omega scan while the detector is fixed in place. Three omega scans are performed by varying the 2-theta position (0.8^o, 1.2^o, 1.5^o) and the offset angle is determined from the collected profiles automatically by the software, which is about 0.1^o. For in-plane SAXS measurement, incident angle (α_i) of the X-ray beam is chosen as 0.3^o.

5. SHAPE-CONTROLLED SYNTHESIS OF TRANSITION METAL OXIDE NANOCRYSTALS

5.1. Introduction

Transition metal oxides are one of the most heavily studied and mass-produced materials in the world for many emerging applications such as catalysis,[221,222] cosmetics,[223] solar cells,[224] electronic devices,[225] batteries,[226] and so on. Significant improvement of materials properties can be achieved through the engineering of materials at the nanoscale. For example, large surface area and high surface to volume ratio allow nanocrystals to be highly active catalytic materials. In addition, the surfactant-assisted high temperature synthesis enables nanocrystals to exhibit excellent colloidal stability in solution, which offers the potential for low-cost, robust fabrication by highly reproducible solution-based processes.

The control of nanocrystal morphology is crucial since the size, shape, and composition significantly influence the properties of the transition metal oxide nanocrystals. The shape dependence of photocatalytic hydrogen evolution has been reported using highly monodisperse and shape controlled TiO_2 nanocrystals, revealing that {101} facets of anatase are more active than the {001} facets in the photoreforming of methanol by platinized TiO_2 under light illumination.[227] In addition, shape dependent optical response is also well-

documented, for instance, shape effects on the plasmonic response of transparent conducting oxide nanocrystals has been demonstrated by the systematic study of shape-controlled indium doped cadmium oxide nanocrystals.[228] In order to engineer the properties of nanomaterials by tailoring the size and shape, it is crucial to develop the colloidal synthetic methods to synthesize highly uniform transition metal oxide nanocrystals with controllable sizes and shapes. In this chapter, we introduce a generalized non-hydrolytic synthesis to control the shape of highly uniform transition metal oxide nanocrystals with metal halide precursors and 1-octadecanol, demonstrating that a wide range of compositions can be designed by this method.

5.1. Generalized Synthesis of Transition Metal Oxide Nanocrystals.

Scheme 5.1 is the generalized synthetic method for early transition metal oxide nanocrystals. Transition metal chloride, for example, $TiCl_4$, WCl_6, or $VOCl_3$ is used as a precursor for the reaction. In the presence of oleylamine and 1-octadecanol, the mixture is heated between 250^oC to 320^oC and kept at this temperature for a given time. The product is precipitated by adding excess methanol and collected by centrifugation.

$$M\text{-}X + \text{1-octadecanol} \xrightarrow[250^oC\text{-}320^oC]{\text{oleylamine}} \text{Metal Oxide Nanocrystals}$$

$$M\text{-}X : WCl_6, TiCl_4, VOCl_3$$
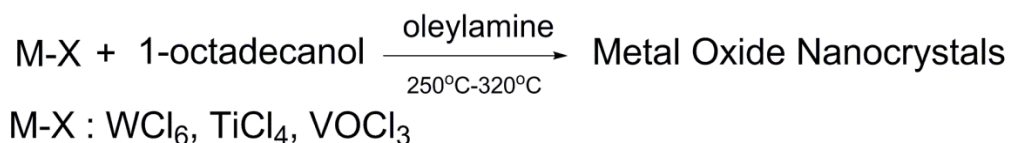
Scheme 5.1. Synthesis of metal oxide nanocrystals *via* non-hydrolytic reaction.

Colloidal tungsten oxide (WO_x) nanocrystals are synthesized using WCl_6 precursors. No reaction occurs in the absence of 1-octadecanol, which indicates that the formation of tungsten oxide occurs through the non-hydrolytic reaction between the metal halide and a primary alcohol.[229] Although the reaction occurs in the absence of oleylamine, it is observed that the use of oleylamine as reaction solvent allows the formation of nanocrystals with well-defined shape and size uniformity. In addition, oleylamine also acts as a surfactant enhancing the colloidal stability of nanocrystals in non-polar media. Figure 5.1a-c show TEM and SEM images of WO_x nanowires. The width of individual nanowires is less than 5 nm in average and reaches about 250nm in length. Longer nanowires, about 800nm in length, are obtained with when trioctylamine is used instead of oleylamine.(Figure 5.1e) Figure 5.1d represents the XRD pattern of WO_x nanowires. The diffraction peaks are matched to monoclinic WO_3 phase (JCPDS no. 5-0392). Relatively sharp peaks at (010) and (020) diffractions indicate that nanowires are growing along (010) direction, which is corroborated by HRTEM image.(Figure 5.1b inset) As-synthesized nanowires are dark blue in color due to the broad absorption from red to near-IR range (Figure 5.1f), which might be attributed to oxygen vacancies generated during the reaction, or the presence of W^{5+} from the reduction of W^{6+} in a reductive reaction condition from the presence of amine and alcohol.
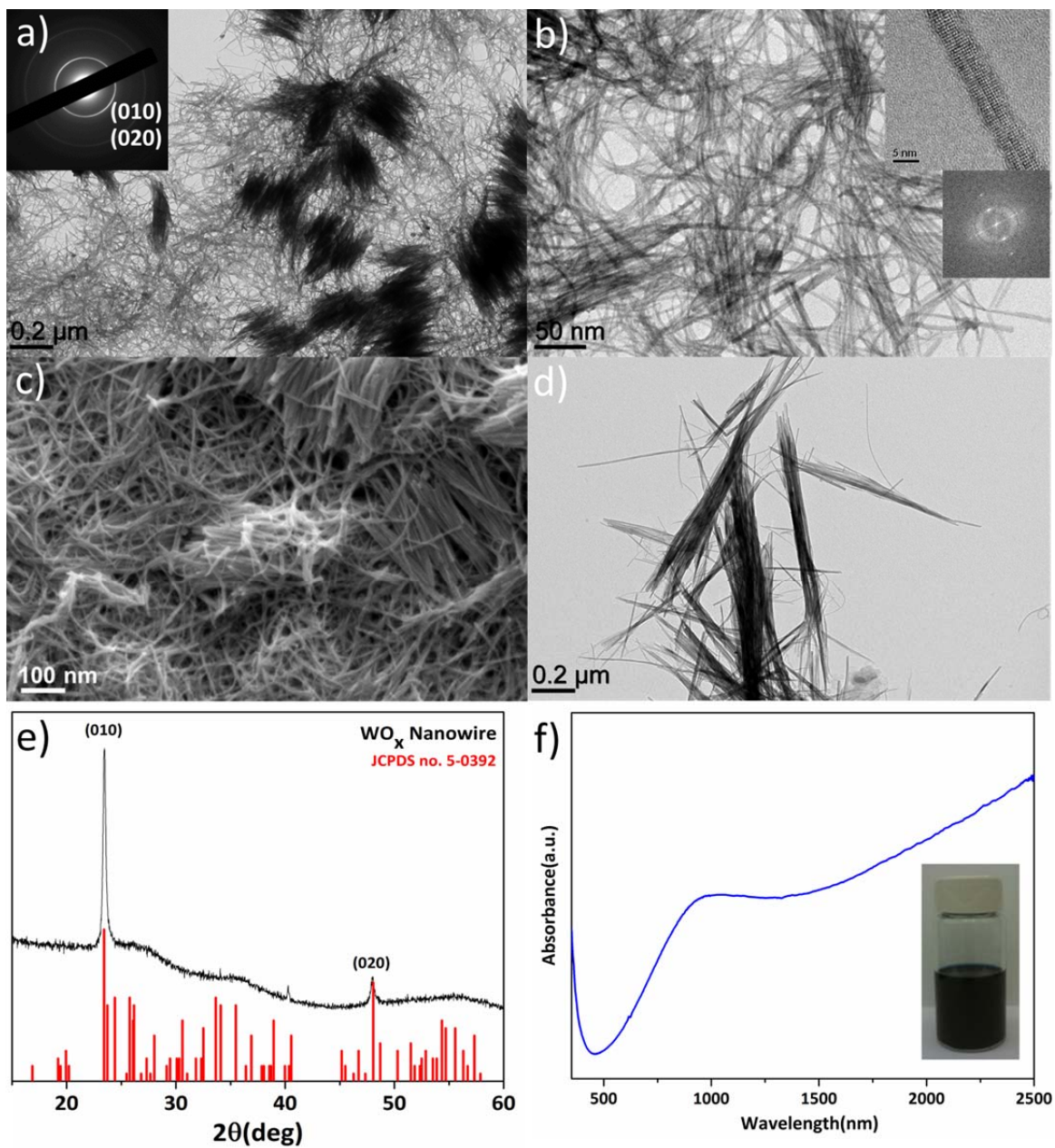
Figure 5.1. a) Low magnification, b) high magnification TEM images, and c) SEM image of WO$_x$ nanowires synthesized with oleylamine and 1-octadecanol surfactants. d) TEM image of WO$_x$ nanowire synthesized with trioctylamine and 1-octadecanol. e) PXRD pattern and f) optical absorption of WO$_x$ nanowires. Inset is an optical image of nanowires dispersed in hexane.

Titanium dioxide (TiO_2) nanowires are synthesized with an addition of $TiCl_4$ instead of WCl_3 under the same reaction conditions. Figure 5.2 displays a TEM image of TiO_2 nanowires. The width of nanowires is about 10nm and the length is about 50nm to 100nm. The SAED pattern reveals that as-synthesized nanowires are brookite phase.
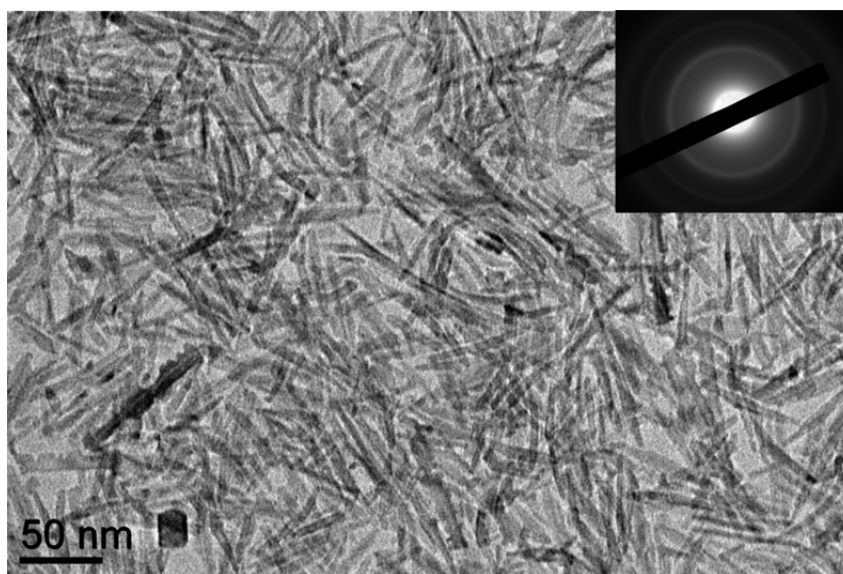
Figure 5.2. TEM image of TiO_2 nanowires synthesized in presence of 1-octadecanol and oleylamine. The inset is SAED pattern.

With $VOCl_3$ precursors, vanadium oxide nanocrystals are obtained as a final product. At $250^\circ C$ and 30min reaction time in the presence of oleylamine and 1-octadecanol, pseudo-spherical nanocrystals are formed with the average size of 4.3 ± 1.0 nm (Figure 5.2a,b). When the reaction temperature is increased to

143

270°C, disk-shape ultra-thin nanoplates are formed exclusively as displayed in Figure 5.2c and d. Disk-shaped nanoplates self-assemble into one-dimensional arrays by face-to-face stacking, resulting in the unidirectional aggregation of nanoplates. Figure 5.2c displays the nanofibril-like structures organized by the self-assembly of nanoplates. At high magnification, the edge of nanoplates is observed confirming the plate morphology of the nanocrystals.(Figure 5.2d) Since the size of the nanoplates is highly uniform, the width of the nanofibril structures is also almost identical.
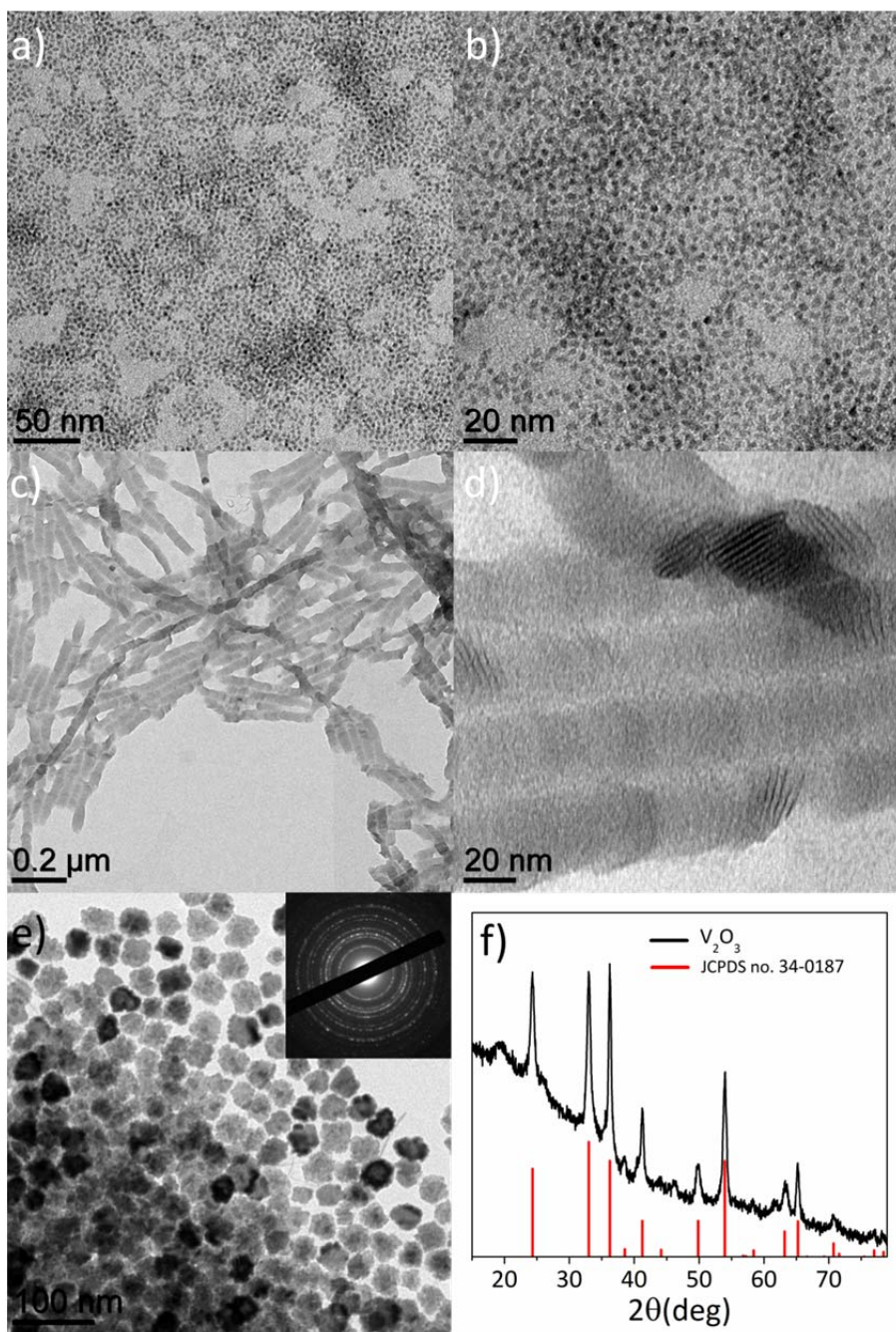
Figure 5.3. TEM images of VO$_x$ nanocrystals synthesized at a), b) 250°C and c), d) 270°C for 30min reaction condition with oleylamine and 1-octadecanol e) TEM image and f) PXRD pattern of V$_2$O$_3$ nanocrystals synthesized at 300°C.

At 300°C for 30 min reaction with VOCl$_3$, oleylamine, and 1-octadecanol, pseudo-spherical nanocrystals are obtained as a final product with the size of about 25nm and a rough surface morphology. The PXRD pattern shows that the crystal structure is the rhombohedral V$_2$O$_3$. Although the oxidation state of starting precursors is vanadium 5$^+$ in vanadium oxychloride (VOCl$_3$), the presence of primary alcohol and amine in the reaction mixture induce the reduction of oxidation state of vanadium from 5$^+$ to 3$^+$. When oleic acid is used instead of oleylamine, at 300°C for 30min reaction time, ellipsoidal nanoplates are synthesized as a final product with tip-to-tip distance of about 100nm.(Figure 5.4) Figure 5.4 inset shows the optical image of colloidal VO$_x$ nanoplates dispersed in hexane.
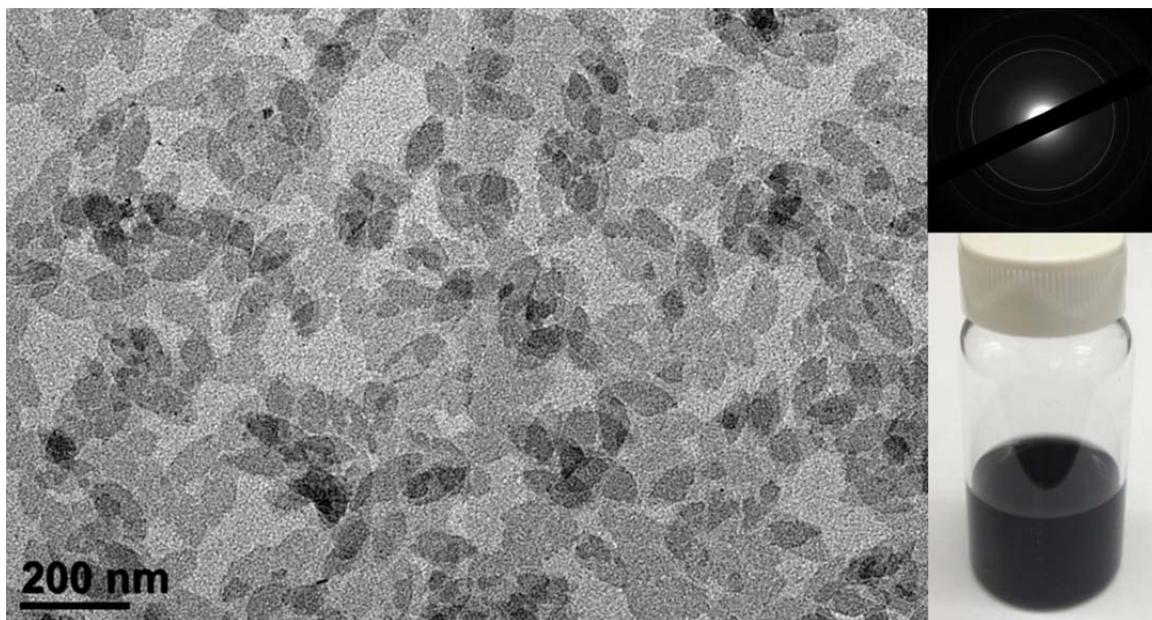
Figure 5.4. TEM images of VO$_x$ nanoplates synthesized in presence of oleic acid, 1-octadecanol, and 1-octadecene. The reaction is performed at 300°C for 30min.

5.3. Conclusion

In this section, we introduced a generalized method to synthesize transition metal oxide nanocrystals. In the presence of oleylamine and 1-octadecanol with metal halide precursors such as WCl$_6$, TiCl$_4$, and VOCl$_3$, highly uniform nanocrystals, WO$_x$, TiO$_2$, and VO$_x$ respectively, are synthesized with different morphologies such as nanosphere, nanoplates, and nanowires. The presence of primary alcohol is important indicating that the reaction may occur through non-hydrolytic reaction between the metal halide and a primary alcohol. We observe that the shapes of the nanocrystals are further tunable by changing the type of surfactants used for the reaction. Early transition metal oxides are widely used

for many emerging techniques. The shape-controlled metal oxide nanocrystals could be a promising platform to understand the shape-dependent physical properties of the metal oxide materials.

5.4. Experimental Section

Materials. All chemicals are used as purchased without any further purification. vanadium ocychloride (99%), oleic acid (technical grade, 90%), oleylamine (technical grade, 70%), 1-octadecene (technical grade, 90%) are purchased from Sigma Aldrich. Tungsten(VI) chloride (>99.9%), titanium(IV) chloride (>99.9%), are purchased from ACROS Organics. 1-octadecanol (97%) are purchased from Alfa Aesar.

Synthesis of WO_x nanowires. 1-octadecanol (9.72 g) and oleylamine (30 mL) are added to a 125 mL three-neck flask and degassed at 125 ^{o}C for 1 h. Then, 0.752g of tungsten(VI) chloride is added into the reaction mixtures and heated to 320 ^{o}C at a rate of 10 ^{o}C/min in N_2 environment. The temperature is maintained for 1 hour allowing for the nanocrystal growth. Purification is conducted by adding toluene and excess methanol followed by centrifugation at 6000 rpm for 2 min. Precipitated nanocrystals are redispersed in anhydrous hexane and stored under N_2 environment to prevent oxidation of nanocrystals.

Synthesis of TiO_2 nanowires. The synthetic procedure is the same as the method used for WO_3 nanowires, except that 4ml of $TiCl_4$ are used instead of WCl_6. The reaction is taken at 320°C for 1 hour.

Synthesis of VO$_x$ nanocrystals. The synthetic procedure is the same as the method used for WO$_3$ nanowires, except that 4ml of VOCl$_3$ are used instead of WCl$_6$. The reaction is taken at different temperatures, at 250°C, 270°C and 300°C for 30 mins.

Synthesis of VO$_x$ ellipsoidal nanoplates. 4 mL of VOCl$_3$ is added into a mixture of 1.4 mL of oleic acid, 9.72g of octadecanol, and 30 mL of 1-octadecene solvent and is heated to 110 ^{o}C. After evacuation at 110°C for one hour to remove water, the reaction solution is heated to 300°C for 1 hour under high N$_2$ pressure, resulting in the formation of the nanoplates. The reaction solution is cooled to room temperature through addition of toluene. Purification is conducted through addition of excess methanol and centrifuging at 3000 rpm for 2 minutes.

Structure characterization. TEM images and electron diffraction patterns are collected using JEM-1400 microscope equipped with a SC1000 ORIUS CCD camera operating at 120 kV. Powder X-ray diffraction is measured using a Rigaku Smartlab high-resolution diffractometer with Cu Kα radiation (λ=1.5416Å).

CHAPTER 6. SOLUTION-PROCESSED PHASE-CHANGE VO$_2$ METAMATERIALS FROM COLLOIDAL VANADIUM OXIDE (VO$_x$) NANOCRYSTALS

6.1. Introduction

Metamaterials are artificial materials rationally designed from sub-wavelength nanostructures to engineer novel optical properties and to control the interaction of electromagnetic radiation with matter.[230-232] They have been explored for various applications, including negative index metamaterials,[233-235] perfect lenses,[236,237] cloaking[238,239] and sensing devices.[240,241] In most cases, the optical responses of metamaterials are fixed by the structure and electronic properties of the constituent engineered building blocks. Increasingly there is a desire to realize dynamically tunable or switchable structures.[111,242-244] Phase change materials have been extensively studied to provide tuning/switching capabilities in optical systems and metamaterials.[245-248] The physical properties of phase change materials are switched in real-time during a structural phase transition (*e.g.* crystalline to amorphous,[249] or between two distinct crystalline forms[250]), which allows optical responses such as a resonance wavelength to be dynamically modulated by external stimuli.

Vanadium dioxide (VO$_2$) is a promising phase change material to use as a building block in reconfigurable metamaterials. In bulk, VO$_2$ exhibits at low

temperature (68°C) a reversible first-order metal-insulator phase transition,[251] from the semiconducting monoclinic (M1, space group $P2_1/c$) to metallic tetragonal (R, space group $P4_2/mmm$) structure, giving rise to a sharp change in optical and electrical properties. This phase transition can be triggered by many different types of stimuli such as heat,[252] mechanical strain,[253,254] and electric field[255-257] and has been applied in many emerging technologies, such as smart windows,[258,259] optical switches,[260,261] memory devices,[262,263] and Mott transistors.[264,265] Through micro- and nanofabrication methods, various tunable metamaterials have been demonstrated by the integration of phase change VO_2,[266-268] such as plasmonic modulators composed of gold or silver nano-antennae on VO_2 substrates[269,270] and as index modulators in plasmonic waveguides.[271] Phase-change VO_2 films are fabricated by a variety of techniques including the sol-gel method,[272,273] ion implantation,[274] magnetron sputtering,[275] chemical vapor deposition (CVD),[276] and pulsed laser deposition (PLD).[277] The properties of VO_2 are further tailored by chemical doping of the VO_2 matrix to modify the phase transition temperature (T_c),[278] offering an additional degree of freedom to engineer the optical responses of metamaterials. However, to expand the application of VO_2 in nanostructured devices, it is essential to develop simple, scalable, and reproducible techniques to incorporate phase change VO_2 into complex architectures and thus to allow precise engineering of the optical properties of large area surfaces.

In this chapter, we present a solution-based process to fabricate phase-change VO_2 thin films and nanostructures using colloidal vanadium oxide (VO_x) NCs. Solution-based processes utilizing NC precursors offer the potential for low-cost, robust fabrication of highly reproducible films by scalable deposition techniques such as spin-coating and dip-coating,[279,280] and patterning techniques such as ink-jet printing[281] or direct writing.[282] VO_x NCs are synthesized using solution-based colloidal synthesis. Stable suspensions of colloidal VO_x NCs are readily deposited on substrates and transformed into phase-change monoclinic VO_2 (M1, space group $P2_1/c$) through thermal annealing, resulting in high quality optical films over large areas. In addition, we investigate the effect of tungsten (W) doping on the phase transition behavior through systematic control of the dopant concentration during NC synthesis. Solution-based fabrication and controlled doping enables the integration of VO_2 building blocks into thermally responsive ("smart") optical materials and patterning into geometrically tailored, sub-wavelength nanostructured reconfigurable materials by nanoimprinting techniques.

6.2. Switchable Vanadium Dioxide (VO_2) Metamaterials Fabricated from Tungsten Doped Vanadia-based Colloidal Nanocrystals

Vanadium oxide (VO_x) NCs are synthesized through the high temperature thermal decomposition of vanadium oxychloride ($VOCl_3$) in the presence of the

solvent mixture 1-octadecanol and oleylamine. No reaction occurs in the absence of 1-octadecanol, which reveals that vanadium oxygen bonds form through the non-hydrolytic reaction between the metal halide and a primary alcohol.[229] Figure 6.1a display TEM images of synthesized VO_x NCs. VO_x NCs exhibit excellent colloidal stability in nonpolar solvents due to the oleylamine surfactants capping the NC surface (Figure 6.1b). Colloidal VO_x NC dispersions were deposited by spin-coating for structural, optical and electrical characterization. Since many different phases of vanadium oxide exist as stable polymorphs at room temperature and with various oxidation states, it is non-trivial to identify the crystal structure of the synthesized VO_x NCs.[283,284] However, the diffraction peaks observed by powder X-ray diffraction (PXRD) measurements indicate the VO_x NCs are crystalline (Figure 6.1c). This is also corroborated by selected-area electron diffraction (SAED) (Figure 6.1a, inset) and high-resolution transmission electron microscopy (Figure 6.2a, inset). The average NC size calculated from small angle X-ray scattering measurements is 4.3 $\pm$ 1.0 nm (Figure 6.3).
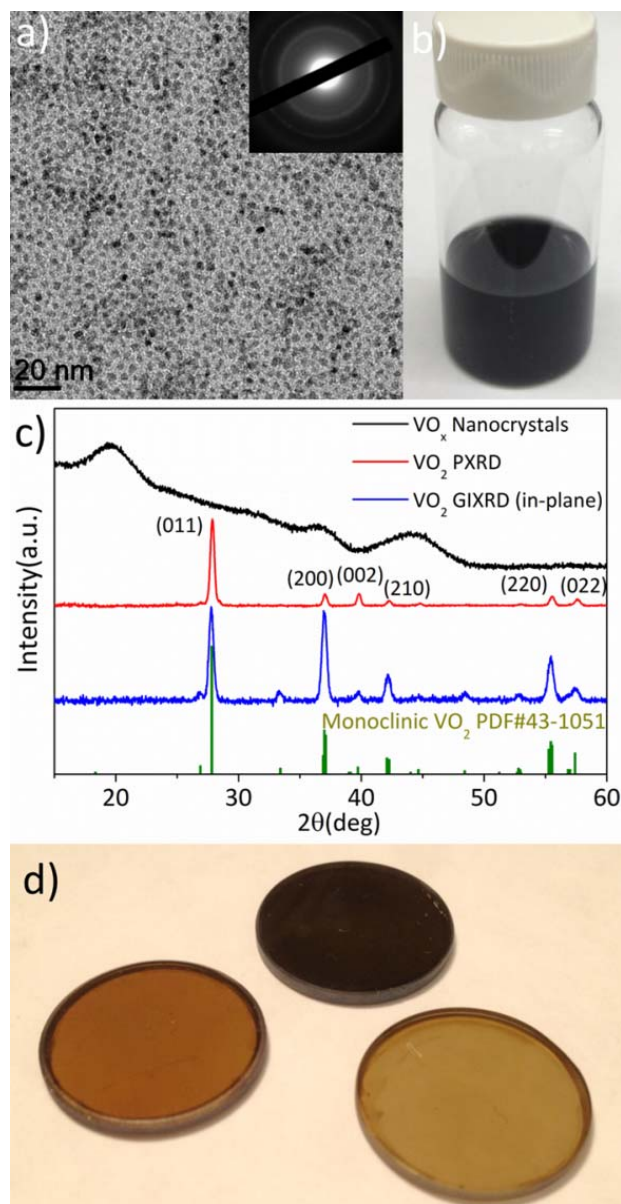
Figure 6.1. a) TEM image of vanadium oxide (VO_x) NCs. The inset shows selected area electron diffraction. b) Photograph of VO_x NCs dispersed in hexane. c) PXRD and in-plane XRD patterns before and after thermal annealing of VO_x NCs on SiO_2/Si wafer. d) Monoclinic VO_2 thin films obtained by rapid thermal annealing of VO_x NCs spin-coated on fused quartz substrates with varying thickness.
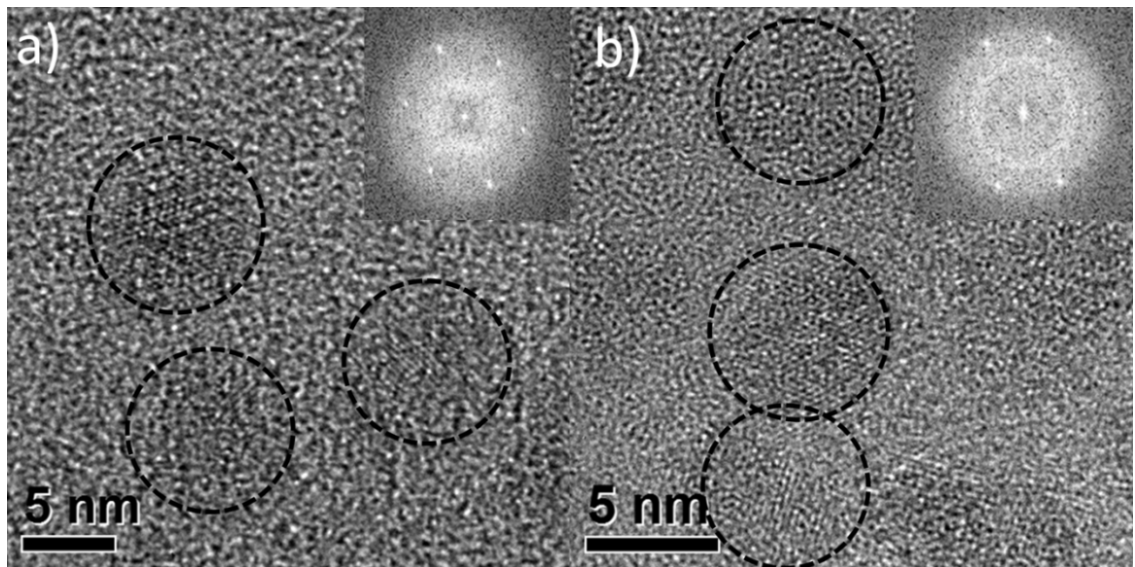
Figure 6.2. High resolution transmission electron microscopy (HRTEM) images of a) undoped VOx nanocystals and b) 1.9% W doped VOx nanocrystals. Insets are fast-Fourier transforms of a single nanocrystal in HRTEM images.
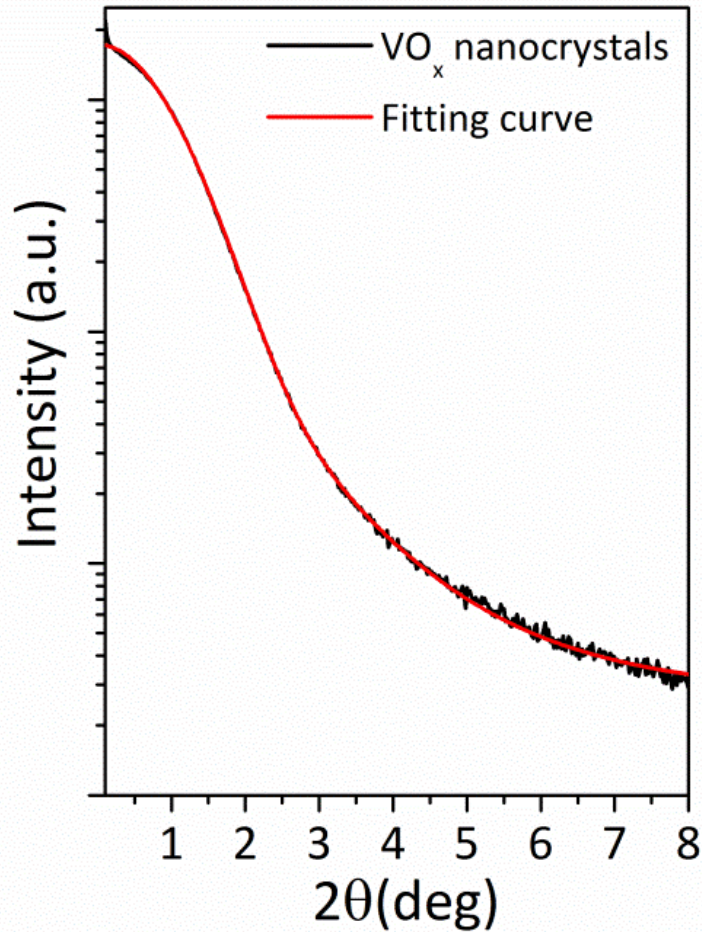
Figure 6.3. Small angle X-ray scattering pattern of VO_x nanocrystals. The average size of VO_x nanocrystals calculated by fitting is 4.3 ± 1.0 nm.

Since the crystal structure of colloidal VO_x NCs differs from the switchable, monoclinic phase VO_2, thermal annealing is used to transform the films. Phase-change monoclinic VO_2 (M1, space group $P2_1/c$) thin films are obtained from spin-coated colloidal VO_x NC films after rapid thermal annealing (RTA), typically at 500 °C for 5 minutes, 450°C for 30 min, and 400°C for an hour under a

reduced oxygen environment of 1 mmHg of air (Figure 6.1d). The presence of some oxygen is critical, not only to remove organic surfactants from the NC surface, but also to induce the structural transformation from VO_x into monoclinic VO_2. This suggests that the stoichiometry of as-synthesized NCs is a slightly oxygen-deficient VO_2. The approach utilizing colloidal NCs provides a potential for large-area, low-cost, and scalable processes on various substrates such as fused quartz, Si wafers, mica, and c-cut sapphire. In addition, the thickness of VO_2 thin films is readily and reproducibly controlled by changing the deposition conditions such as spin-coating rate or the concentration of NCs in the solution used for the deposition.

PXRD patterns, in Figure 6.1c, show that monoclinic VO_2 is obtained after RTA treatment of VO_x thin films. All diffraction peaks match the monoclinic VO_2 structure (M1, space group $P2_1/c$) without any noticeable minority phases or indications of an amorphous background. Preferred orientation of the VO_2 thin film is observed when deposited on SiO_2/Si wafers. Polycrystalline VO_2 thin films are characterized with conventional PXRD and in-plane X-ray diffraction (in-plane XRD) in order to probe the crystallographic orientation of VO_2 grains. Crystal planes aligned perpendicular to the substrate are monitored by PXRD while in-plane orientation is determined by in-plane XRD. From the two complementary measurements, preferred orientation is characterized by comparing the intensities of diffraction peaks from different crystal planes. The diffraction intensities of the (011) plane relative to the (200) plane in PXRD measurements

is much higher than in the in-plane XRD measurement, which suggests that VO_x NCs are transformed into monoclinic VO_2 with a preferred orientation of the VO_2 (011) zone axis aligned perpendicular to the substrate surface during thermal annealing. This preferential orientation is also observed in films deposited on fused quartz and c-cut sapphire (Figure 6.4, 6.5). The effect of the substrate on the epitaxial growth of VO_2 thin films has previously been reported with contrasting findings. For example, polycrystalline VO_2 thin films deposited on c-Al_2O_3 by pulsed laser deposition[285,286] and rf-sputtering[287] show growth of the VO_2 film normal to the substrate in the (002)/(020) direction. However, polycrystalline VO_2 thin films on fused quartz, Si wafers, and c-sapphire, which are prepared by rapid thermal annealing of colloidal NCs, show similar diffraction patterns suggesting that the crystal orientation may not be strongly affected by the substrate.
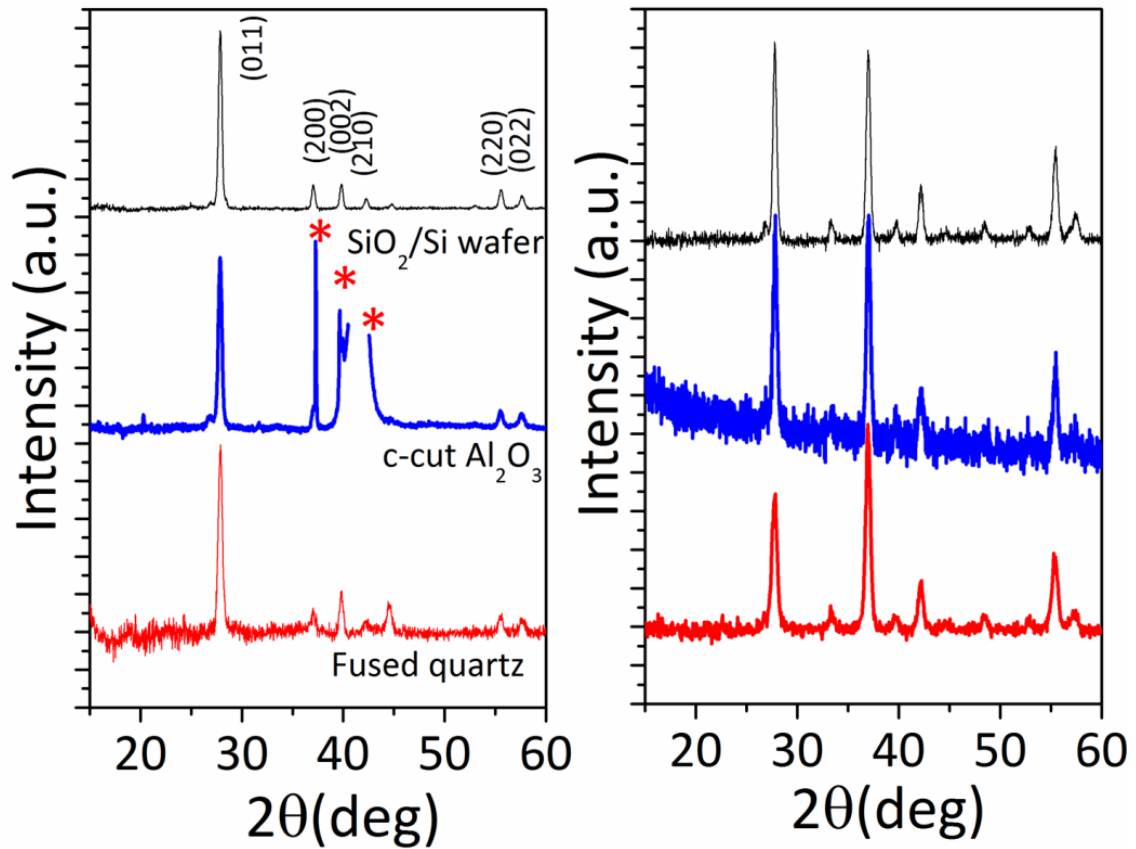
Figure 6.4. Powder XRD and in-plane XRD patterns of VO_2 thin-films on SiO_2/Si wafer, c-cut sapphire, and fused quartz. Asterisks (*) indicate diffraction peaks from the c-Al_2O_3 substrate.
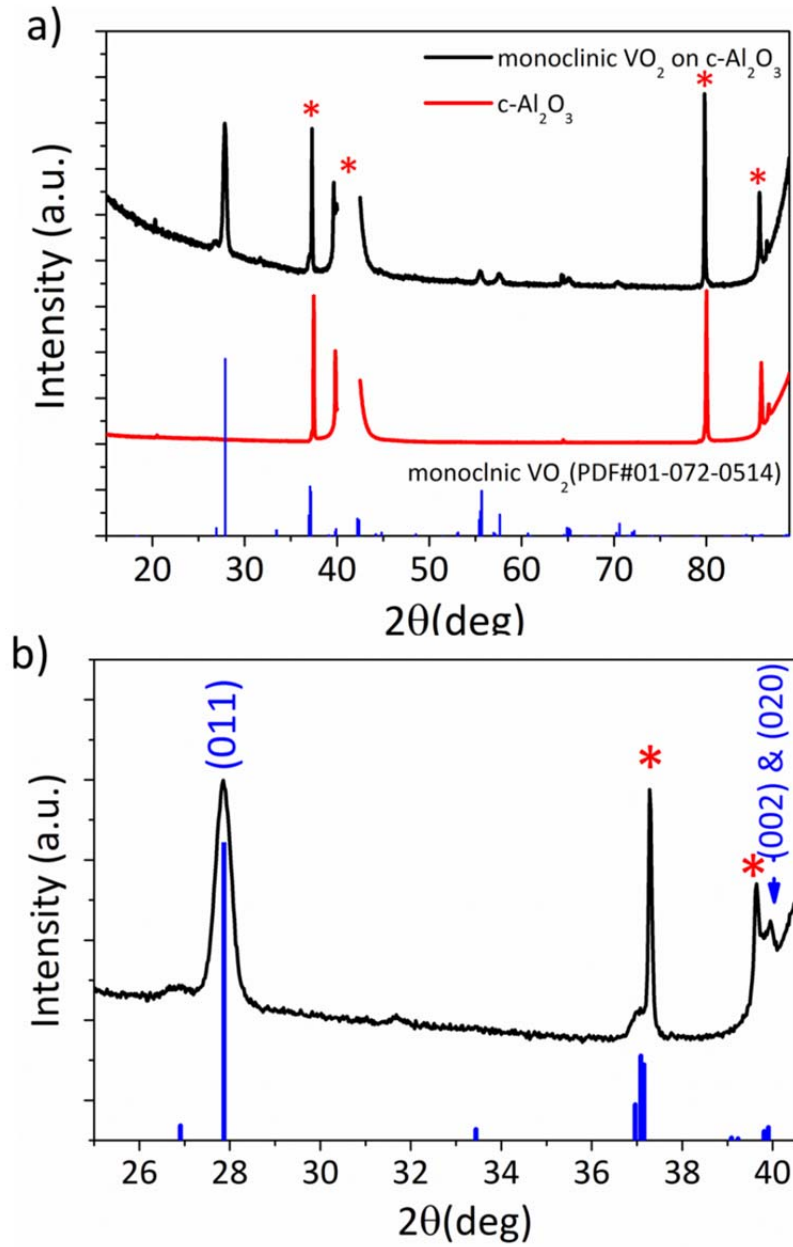
Figure 6.5. a) Powder XRD patterns of c-Al_2O_3 (red) and VO_2 thin-film on c-Al_2O_3 (black) and diffraction pattern of monoclinic VO_2. The intensity of (011) diffraction is much higher than that of (002) and (020). Asterisks (*) indicate diffraction peaks from the c-Al_2O_3 substrate.

The optical properties of the VO_2 thin films are investigated by variable temperature specular reflectance using a Fourier-transform infrared (FTIR) spectrometer. Reflectance spectra are collected in the specular reflection geometry with a 45° incident angle using a gold mirror as the reflectance standard. A thin graphite disk is placed between the sample and the aluminum heating stage in order to prevent back reflection while maintaining efficient heat transport from the heater to the sample. The temperature of the VO_2 films is monitored through a thermocouple attached directly to the VO_2 film surface. Figure 6.6 shows optical reflectance spectra of a VO_2 thin film deposited on a fused quartz substrate as the sample temperature is increased. At room temperature, a fringe pattern is observed with the peak and valley located at 1128 nm and 1732 nm respectively, which are caused by interference between light reflected from the top and bottom of thin films in the insulating phase.[286] At temperatures higher than T_c, the oscillatory interference pattern disappears as the reflectance in the IR region increases sharply due to strong reflectance from the metallic VO_2 phase.
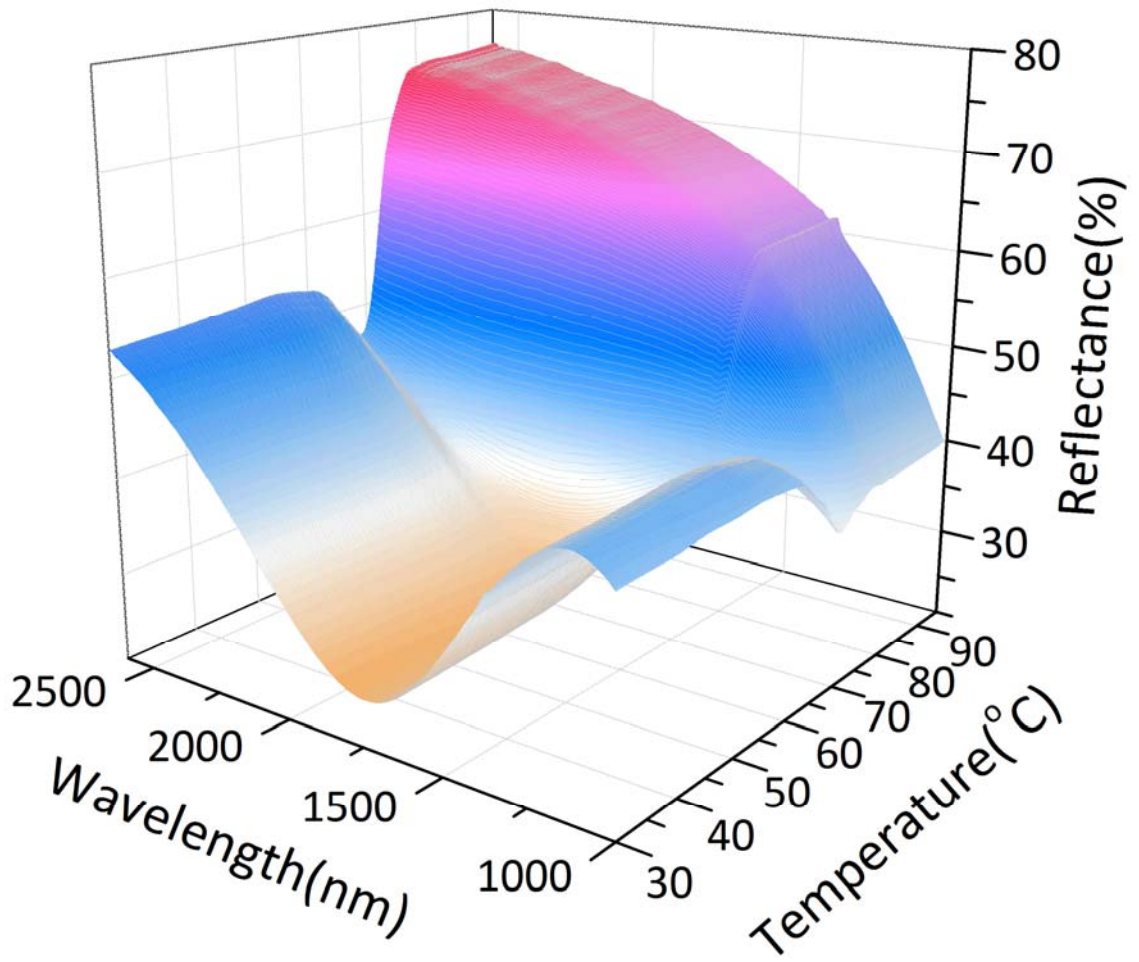
Figure 6.6. Temperature-dependent optical reflectance of a VO_2 thin film
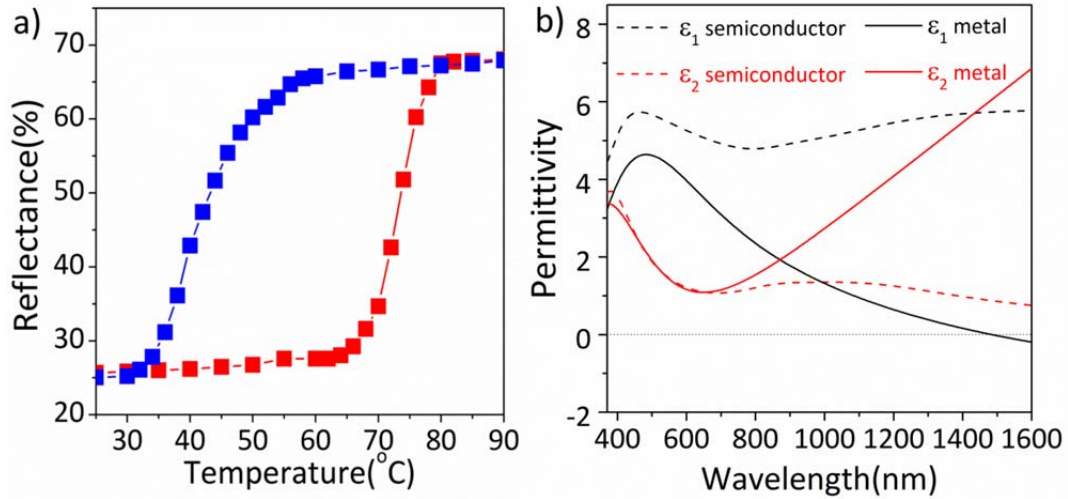
Figure 6.7. a) Hysteresis of optical reflectance recorded at 1550 nm. Reflectance spectra are measured in a specular reflection geometry at 45° to the normal direction. b) The dielectric constant ($\varepsilon = \varepsilon_1 + i\varepsilon_2$) of insulating and metallic VO_2 thin films, extracted from spectroscopic ellipsometry measurements.

When the optical properties of the VO_2 films are measured while the sample is cooling, a significantly lower transition temperature is observed upon switching from the metallic to the insulating phase, indicating a wide hysteresis in the phase change. The width of the hysteresis during the cooling and heating cycle is about 25-30 K in undoped VO_2 films (Figure 6.7a, 6.8). The hysteresis width is known to decrease with increasing grain size as defects and strain at grain boundaries contribute to the energy barrier for the phase transition.[288-290] Atomic force microscopy images reveal that the average grain size after 5 minutes of rapid thermal annealing is approximately 37 nm with a standard deviation of 8.7

nm (Figure 6.9). Although the growth in grain size is observed with longer annealing, RTA preserves the small grain size in the films annealed at even higher temperatures, for example 550 $^{\circ}$C for 5 minutes. The nano-sized grains that are still preserved in the thin-films may cause the large hysteresis between heating and cooling cycles. The large hysteresis could be useful in the design of an optical memory, allowing for non-volatile storage of optical information during the phase transition.[263]
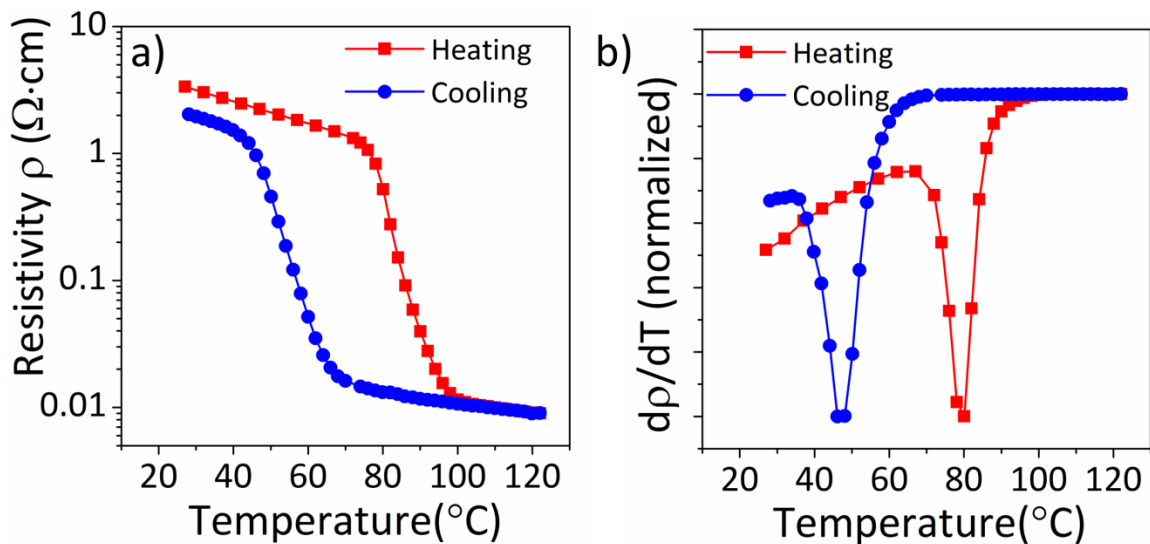
Figure 6.8. a) Temperature-dependent resistivity plot and b) first derivatives of resistivity of undoped VO$_2$ during heating and cooling cycle.
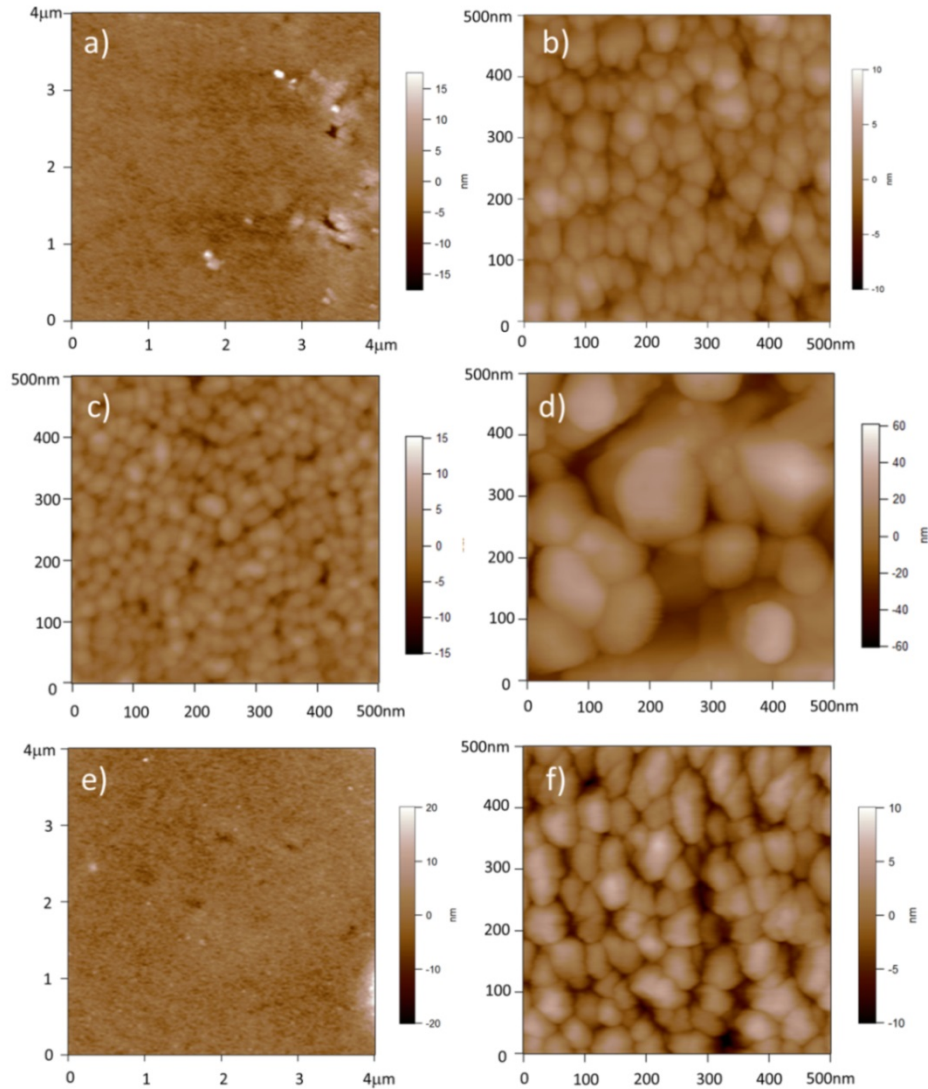
Figure 6.9. Atomic force microscopy images of undoped VO_2 thin-films after rapid thermal annealing a), b) at 500 °C for 5 min, c) at 550 °C for 5 min, and d) at 500 °C for 30 min. The thickness of the thin-films is about 140 nm. e), f) Atomic force microscopy images of 1.9% W-doped VO_2 thin films after rapid thermal annealing at 500 °C for 5 min. The thickness of 1.9% W-doped VO_2 films is about 210nm. All samples are deposited on fused quartz substrates.

The optical constants of both the insulating and metallic phases of VO_2 are extracted using spectroscopic ellipsometry (Figure 6.7b). The complex permittivity of the samples is extracted by fitting the optical response of thin films with a Lorentz-Lorentz model, in the case of the insulating phase, and a Drude-Lorentz model, in the case of the metallic phase. Below T_c, the real part of permittivity is positive over the entire spectral range measured from 400 nm to 1650 nm, indicating the dielectric response of the insulating, monoclinic VO_2 phase. At temperatures higher than T_c, the real part of the permittivity becomes negative in the near-IR region beyond the cross-over energy of 0.86 eV, confirming optically the metallic response of tetragonal $VO_2(R)$. The negative permittivity of our metallic phase VO_2 allows it to be incorporated as a switchable plasmonic building block in the near-IR and IR region.

Controlled doping into the VO_2 lattice is important not only to tailor T_c, but also because it modifies the optical and electrical properties of VO_2.[291,292] NC doping is a technique commonly used to tune electrical,[293,294] optical,[228,295,296] and magnetic properties.[297,298] Colloidal synthetic methods allow for the homogeneous incorporation of dopants or defects into the lattices of a single NC. Since we use VO_x NCs as precursors for the fabrication of VO_2 thin films, it is possible to systematically control the type and concentration of transition metal dopants by simply changing the concentration of metal precursors during NC synthesis. Tungsten (W) doped VO_x NCs are synthesized by the addition of tungsten hexachloride (WCl_6) as the W source for the reaction; otherwise the

conditions are identical to those used for undoped VO_x. Energy-dispersive X-ray spectroscopy (EDS) reveals that the ratio of W and V precursors is maintained after the formation of the NCs, and TEM images show that there is no discernible change in NC size and shape due to the addition of W into the matrix (Figure 6.10). W-doped VO_2 thin films after RTA treatment are of the same high surface uniformity with similar grain sizes as the undoped films (Figure 6.9, 6.11). The surface roughness as characterized by atomic force microscopy is about 2.7 nm for 1.9%W doped VO_2, which is similar to the 1.7 nm found for undoped VO_2 (Figure 5.9). Since W dopants are already distributed in the NC precursors with controlled stoichiometry, the transformed polycrystalline thin films may maintain a statistically uniform distribution of W dopants. In addition, high heating rates in RTA could help minimize thermal diffusion of W dopants, which can prevent phase segregation or local inhomogeneity of the W distribution in the VO_2 matrix.
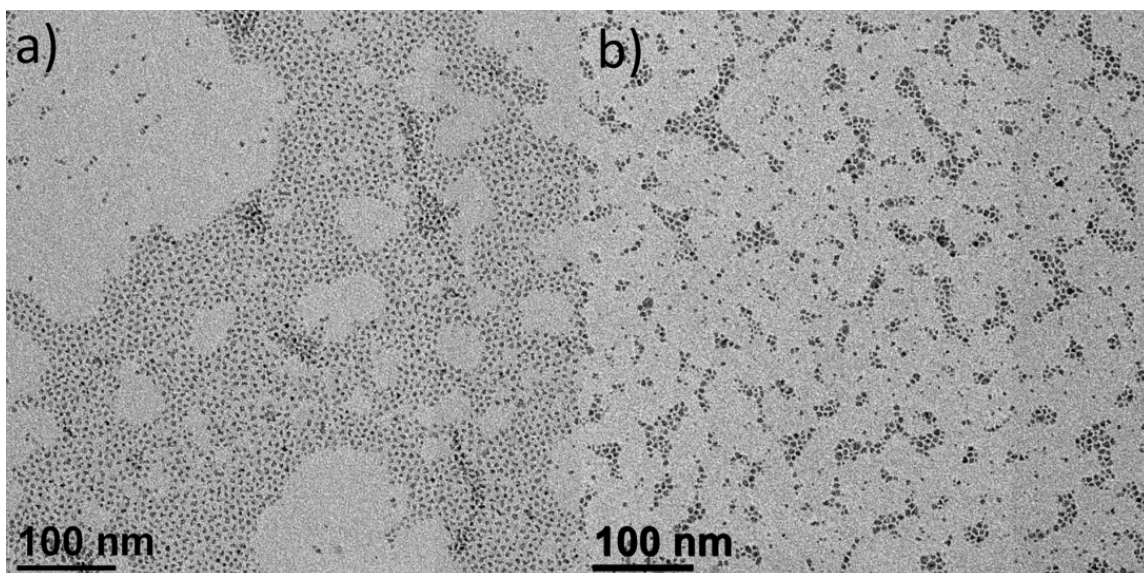
Figure 6.10. TEM images of a) undoped and b) 3% W-doped VO_x
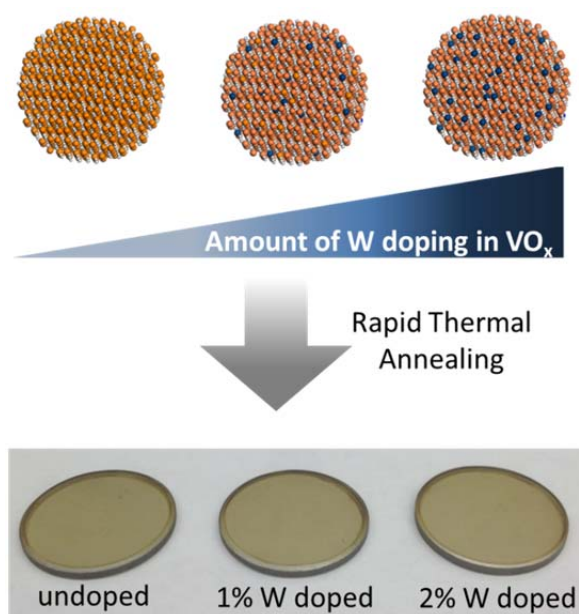
Figure 6.11. Photographs of undoped, 1%W doped, 2% W doped VO_2 thin-films

deposited on fused quartz.

Figure 6.12 displays the variable temperature reflectance of W-doped VO_2 thin films deposited on fused quartz substrates. A decrease in T_c is observed with an increase in W doping concentration in VO_2. It has been reported that increasing the doping concentration causes broadening of the temperature range in which the phase transition occurs and reduces the degree of property change across the transition.[299] However, we observe that a steep change in reflectance across the phase transition is maintained in W-doped VO_2 thin films formed from the colloidal NCs, similar to that in undoped VO_2. Figure 6.12b presents the first derivative of the optical reflectance (dR/dT) of W-doped thin films as a function of doping concentration. The full-width at half maximum (FWHM) of dR/dT is similar between the 0 to 1.9% (atomic %) doping concentrations that we explored. The same trend is also observed in the electrical measurements. The temperature-dependent resistivity of W-doped VO_2 thin films is investigated using the van der Pauw method. Figure 3c displays the electrical resistivity of W-doped VO_2 over a range of temperatures from 5 ^{o}C to 100 ^{o}C. It is observed that an increase in doping concentration leads to a decrease in T_c while maintaining the FWHM of dρ/dT, matching the trend observed by optical reflectance.
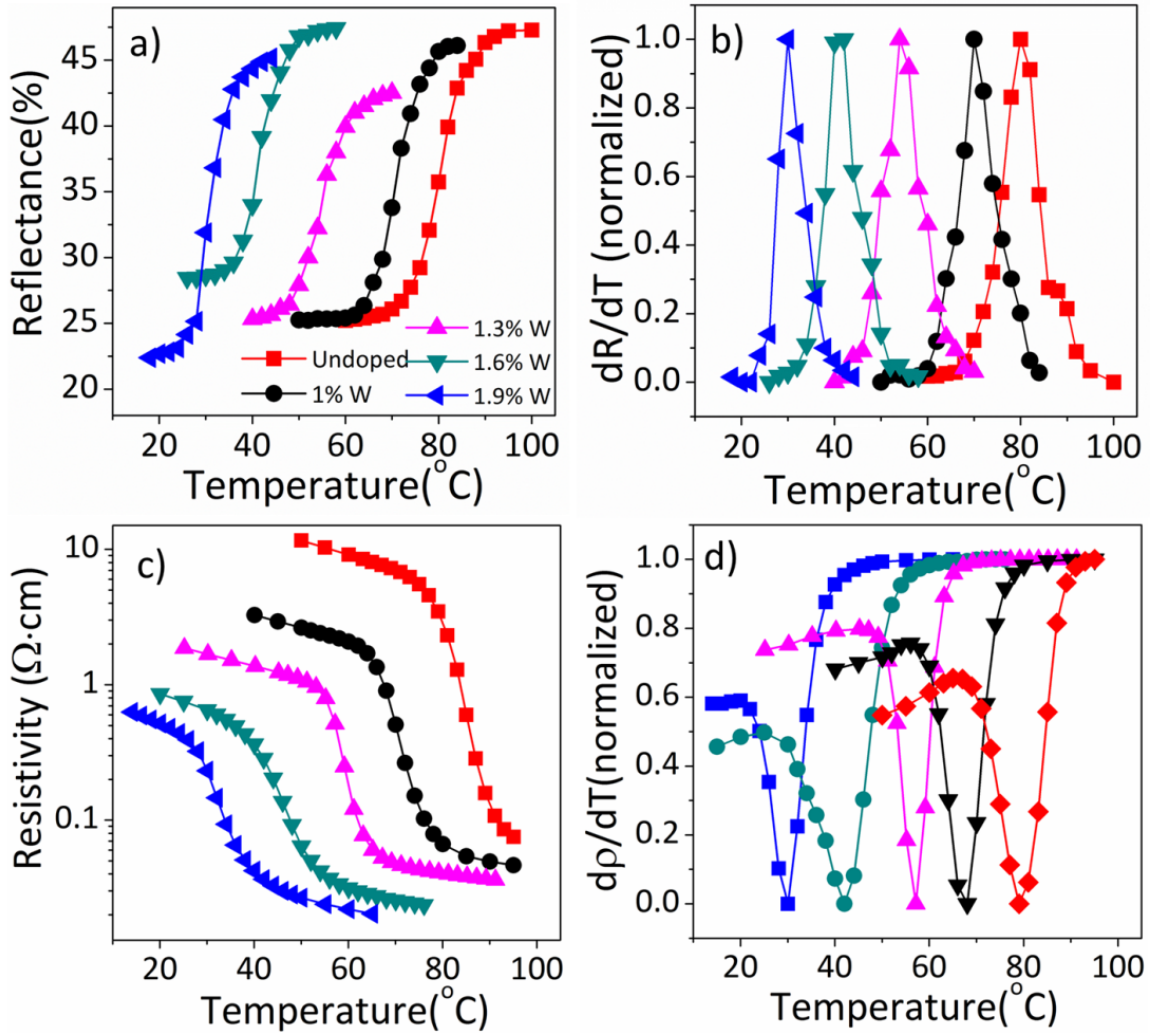
Figure 6.12. a) Temperature-dependent reflectivity at 2500 nm from W-doped VO$_2$ thin films with several different W-doping concentrations and b) the first derivatives of optical reflectivity spectra. c) Temperature dependent resistivity plots of W-doped VO$_2$ thin films on fused quartz substrates with several different W-doping concentrations and d) the first derivatives of resistivity.

A series of colloidal NC solutions, in which the stoichiometry of V and W are systematically varied, can be readily processed as on-demand NC inks by solution-based processes. This allows for the simple, robust, and reproducible integration of doped VO_2 into complex architectures for metamaterials. We employ this technique to build multilayered VO_2 nanostructures by sequential deposition of VO_2 with different doping concentrations. Layered films composed of metal and dielectric layers are technologically important as they allow the engineering of transmittance, reflectance, and absorption for applications in anti-reflective coatings,[300] 2-D waveguides,[301] and perfect light absorbers.[302] A multilayered VO_2 nanostructure composed of 1.9% W, 1.3% W and undoped layers, is fabricated by sequential spin-coating of colloidal NCs at 1500 rpm for 30 sec followed by RTA at 500 ^{o}C for 5 min after the deposition of each layer. The T_c of each layer is 30 ^{o}C, 52 ^{o}C, and 80 ^{o}C, respectively. Since the metallic and dielectric properties of W-doped VO_2 may be dynamically switched at T_c, this integrated layered structure incorporating different doping concentrations allows for layers that can be independently switched at different phase transition temperatures.

Figure 6.13(a-d) displays variable temperature reflectance measurements of the multilayered structure. At room temperature, all of the layers are insulating. Upon increasing the temperature above T_c for the 1.9% W-doped VO_2, a phase transition occurs in the bottom layer, resulting in the formation of metal-insulator-insulator structure. A shift in the peak and valley positions in the reflectance

fringe patterns is observed corresponding to the structural transformation. The reflectance minimum at the valleys of oscillating patterns decreases from 9% to 3% and shifts to longer wavelength (from 2300 nm to 3000 nm), demonstrating the anti-reflective property in the near-IR. The optical response of the metal-insulator-insulator structure is maintained until the temperature reaches the phase change temperature of the 1.3% W-doped VO_2. Around 50 ^{o}C, the second metal-insulator transition occurs in the middle layer to form a metal-metal-insulator structure, leading to a shift in the reflectance minimum to shorter wavelengths (from 3000 nm to 1700 nm). At the reflectance minimum, both reflectance and transmittance exhibit very low values (around 5%), indicating that a strong absorption resonance occurs in the metal-metal-insulating phase. This absorption resonance persists at incident angles from 5° to about 50° and reflection increases above 50° (Figure 6.14). At temperatures higher than the phase change temperature of undoped-VO_2, all of the layers become metallic VO_2 and the films become reflective throughout the near-IR and IR regions. This suggests that we can engineer the optical responses of multilayered reconfigurable materials, exhibiting abrupt switching from that of a strong light absorber to that of a Drude-like reflector in the near-IR region.
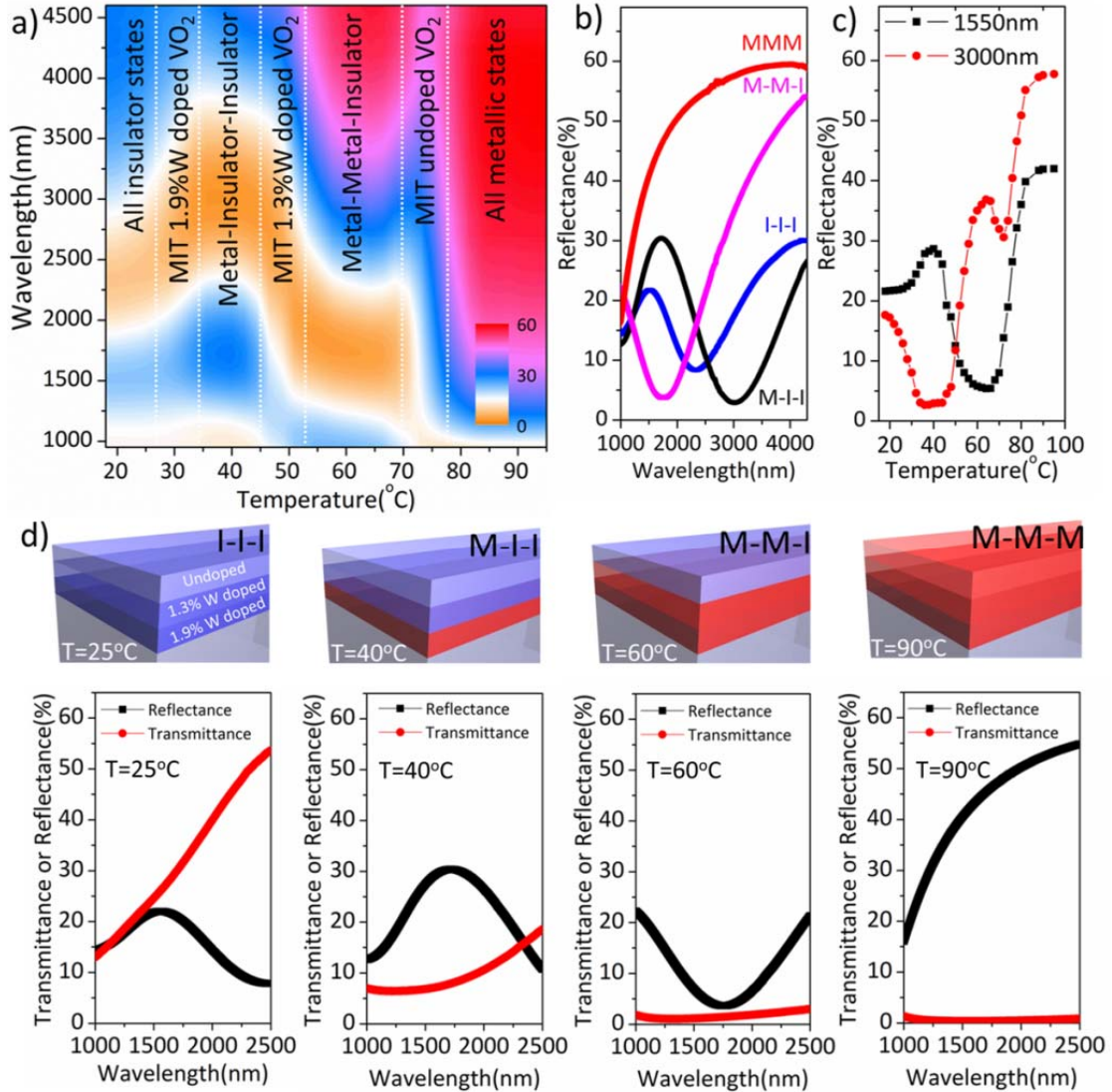
Figure 6.13. a) Variable temperature reflectance spectra of a multilayered VO$_2$ thin film composed of 1.9% W, 1.3% W and undoped VO$_2$ measured at a 20° incident angle and b) representative reflectance spectra during the phase transition. I and M stand for insulating and metallic phases of VO$_2$ at each layer. c) Optical reflectance spectra monitored at 1550 nm and 3000 nm. d) Transmittance and reflectance spectra collected at 25 ^{o}C, 40 ^{o}C, 60 ^{o}C and 90 ^{o}C and schematics of the phase of the differentially-doped VO$_2$ layers.

173
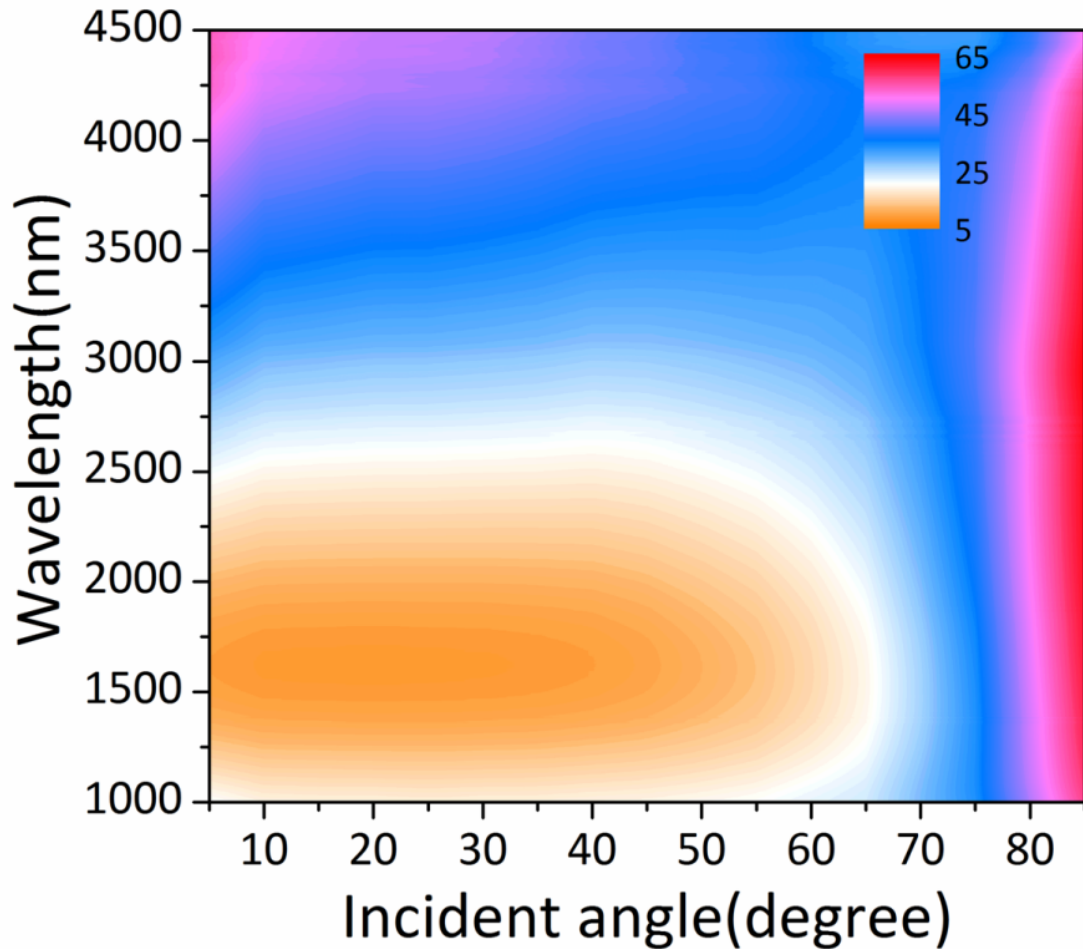
Figure 6.14. Reflectance spectra of VO$_2$ multilayer structures composed of a metal-metal-insulator phase with various angles of incidence ranging from 5° to 85°. The legend describes % reflectance.

The reflectance at single wavelengths is monitored to better visualize the phase transition of the multilayered films. Figure 6.13 presents the reflectance collected at 1550 nm and 3000 nm upon increasing temperature. It is worth

noting that the phase change temperature and steepness of the reflectance change of each layer at T_c are maintained even after integration into the multilayered structure. In addition, the plateaus between the T_c of each layer are also observed, indicating that each transition is discrete occurring only at the phase change temperatures of individual layers. Thus, we have demonstrated that VO_2 multilayered thin films, composed of different W doping concentrations, can exhibit multiple phase transition temperatures in a single structure, changing their optical properties at each phase transition.

Fabrication of sub-wavelength plasmonic building blocks from Au colloidal NCs has recently been demonstrated by nanoimprinting to achieve large-area, complex metamaterials.[303] Coupling this colloidal nanocrystal-based nanoimprinting technique with metallic VO_2 allows for the preparation of switchable plasmonic VO_2 nanostructures. Figure 6.15a shows the schematic of the process used to form nanostructured VO_2. First, polymer resists are patterned by nanoimprint lithography using a nanostructured Si master designed in size and shape. Then, colloidal NCs are spin-coated on top of the patterned substrate, followed by lift-off of the polymer resist to deposit patterned VO_x thin films. Phase-change VO_2 nanostructures are then obtained after RTA of the patterned VO_x NC films. Figure 6.15 shows SEM images of planar arrays of VO_2 (b, c) nanopillars and (d, e) nanowires. Nanostructured metallic VO_2 is expected to show a size-dependent dipolar plasmonic resonance as reported in previous studies,[304-306] although it is a strongly damped resonance due to optical losses.[289]

Figure 6.15f presents the normalized transmittance spectra of hexagonal arrays of metallic VO_2 nanopillars upon varying the pillar diameter. With increasing diameter from 250 nm to 460 nm, the resonance peaks are red-shifted from 1520 nm to 1750 nm. In order to understand the trend of the transmittance spectra of patterned VO_2, we conducted finite-difference time-domain (FDTD) simulations using the dielectric function of metallic VO_2 derived from spectroscopic ellipsometry. The resonance peaks of simulated spectra are also shifted to longer wavelength from 1600 nm to 2200 nm with increasing pillar diameter, consistent with the experimental results. The magnitude of the shift in the resonance frequency as a function of pillar size in the measured data is smaller than the values in simulated results. This is not suprising as the morphology of VO_2 nanopillars is known to dramatically affect plasmonic responses[289] and that is not captured in the simulations. The VO_2 nanostructures formed by the RTA of 4 nm diameter nanocrystals limit grain growth to about 40 nm and thus the granular features of the plasmonic VO_2 nanostructures could be responsible for the discrepancy between experiment and simulation.
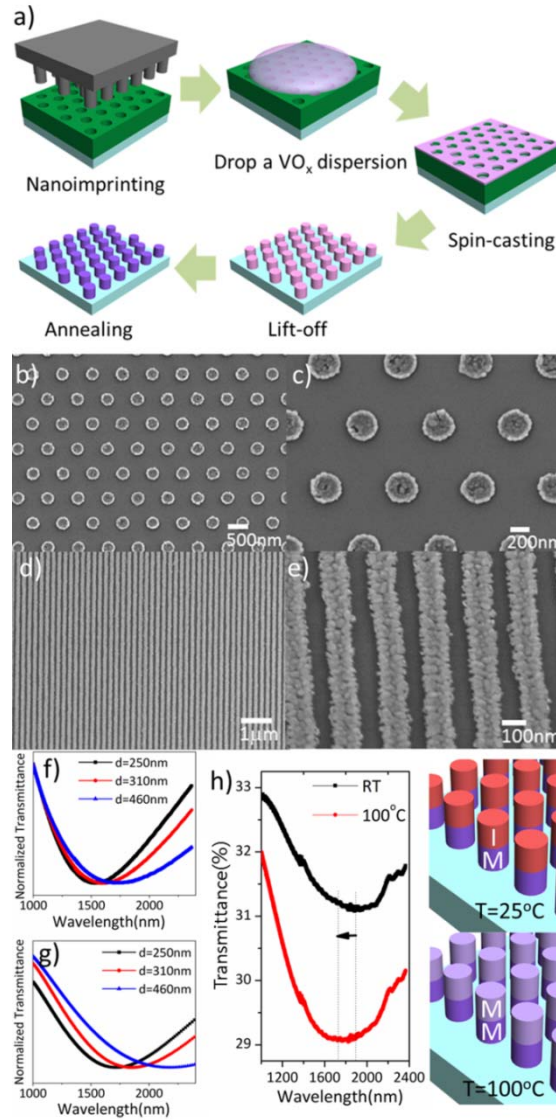
Figure 6.15. a) Schematic of subwavelength VO_2 nanostructure fabrication using nanoimprint lithography. SEM images of VO_2 nanostructure arrays of b, c) a hexagonal lattice of nanopillars and d, e) nanowires. f) Experimental and g) simulated transmittance of VO_2 nanopillar arrays of varying diameters.   h) Transmittance of layered VO_2 nanopillar arrays vertically stacked with 3% W and undoped VO_2. Transmittance spectra are collected at 25° C and 100° C.

Coupling lateral patterning of subwavelength VO_2 nanostructures by nanoimprint lithography with the vertical structuring of multi-layered thin films, we form three-dimensional VO_2 nanopillar arrays where each pillar consists of a vertical stack of doped VO_2 with different W doping concentrations. Figure 6.15d displays a schematic of nanopillar arrays composed of 3% W-doped and undoped VO_2. A three-dimensional, hierarchical nanostructure is fabricated by sequential spin-coating of 3% W doped VO_x and undoped VO_x onto the polymer resist. In order to prevent intermixing of NCs between two layers, mild heating at typically 100 ^{o}C for 30 min is applied after the first layer is deposited. As above, polymer resists are lifted-off using acetone and films are thermally annealed to obtain patterned VO_2. At room temperature, 3% W-doped VO_2 is metallic, forming metal-insulator structures in each pillar. The dipolar plasmonic response of the nanopillar arrays is observed by the broad peak located at about 1900 nm. Upon increasing the temperature above the T_c of undoped VO_2, the upper layer in the pillar changes to metallic and the resonance of the nanostructures blue-shifts from approximately 1900 nm to 1750 nm. The shift of the resonance peaks to shorter wavelengths is consistent with the second phase transition at the upper layer effectively causing an increase in the height of the metallic nanopillars, resulting in a shift of the resonance peaks to shorter wavelengths.[307,308]

6.3. Conclusion

In summary, we demonstrate solution-processed tunable VO_2 metamaterials using colloidal VO_x NCs. Colloidal VO_x NCs are synthesized using vanadium oxychloride precursors in the presence of 1-octadecanol and oleylamine solvent mixture. Thermochromic VO_2 are obtained by rapid thermal annealing of VO_x NCs. Stable dispersions of the colloidal NCs are readily processed by conventional deposition techniques, and nanostructured using nanoimprinting. Tungsten doping is readily controlled by changing the precursor concentration during the synthesis, allowing for a systematic change of the phase transition behaviors. Solution-based fabrication and controlled doping allow for integration of doped VO_2 building blocks into complex architectures including switchable metal-dielectric multilayered structures composed of W-doped VO_2 with different dopant concentrations and patterned layered structures. The versatility and processiblity of solution-based fabrication provides a route to integrate switchable VO_2 building blocks into a variety of nanostructured metamaterials to modulate the optical response in real-time.

6.4. Experimental Section

Materials. All chemicals are used as purchased without any further purification. Vanadium (V) oxychloride (99%), oleylamine (technical grade, 70%), are

purchased from Sigma Aldrich. 1-octadecanol (97%) are purchased from Alfa Aesar. Tungsten (VI) chloride (99.9+%) is purchased from Acros Organics.

Synthesis of VO$_x$ Nanocrystals. 1-octadecanol (7.92 g) and oleylamine (30 mL) are added to a 125 mL three-neck flask and degassed at 125 ^{o}C for 1 h. Then, 0.4 mL of vanadium oxychloride is added into the reaction mixtures and heated to 250 ^{o}C at a rate of 10 ^{o}C/min in ambient air environment. The temperature is maintained for 20 min allowing for the nanocrystal growth. Purification is conducted by adding toluene and excess methanol followed by centrifugation at 6000 rpm for 2 min. Precipitated nanocrystals are redispersed in anhydrous hexane and stored under N$_2$ environment to prevent oxidation of nanocrystals.

Rapid thermal annealing for structure transformation from VO$_x$ to monoclinic VO$_2$. Colloidal VO$_x$ nanocrystals are deposited on the substrates by spin-coating, typically at 1500 rpm for 30 sec. Nanocrystal thin-films are annealed using rapid thermal annealing (ULVAC MILA-3000) by ramping to 500 ^{o}C in 10 sec and annealing for 5min under 1mTorr of air environment.

Nanoimprint lithography. Vanadium oxide (VO$_2$) based plasmonic nanostructures are fabricated by nanoimprint lithography and lift-off using VO$_x$ colloidal nanocrystals. Commercial float glass (Delta-technologies) is cleaned by ultra-sonication with acetone and isopropyl alcohol for 10 min and rinsed with deionized water. Nanoimprinting lithography is done using a Nanonex (NX-2600) nanoimprinting system. A thermal nanoimprint resist (NXR-1000) film is made by spin-coating at 3000 rpm for 1 min, and baked at 150 °C for 5 min. A nanostructured Si based template is used as a master stamp. The thermal resist

coated glass substrate is covered by a master stamp, and then the stack of the stamp and substrate is heated and pressed up to 130 °C and 300 psi for 5 min in order to fill the cavity of the stack, and then, it is cooled for de-molding. After imprinting, an oxygen "descum" process is performed on the samples in a Technics dry etching tool for 35 sec with 80 sccm O_2 and 150 W power, in order to remove residual polymer layers. To fabricate vanadium oxide (VO_2) based plasmonic nanostructures, VO_x nanocrystals are spin-coated on the imprinted pattern on the glass substrate. Then, the polymer resist is removed by lift-off in acetone for 30 sec to obtain the inverted VO_x patterns. Nanostructured thermochromic VO_2 is obtained after rapid thermal annealing at 500 ^{o}C for 5 min under 1mTorr air.

Structural characterization. TEM images and electron diffraction patterns are collected using a JEM-1400 microscope equipped with a SC1000 ORIUS CCD camera operating at 120 kV. Scanning electron microscopy [142] and energy-dispersive X-ray spectroscopy was performed on a JEOL 7500F HRSEM. Powder X-ray diffraction, in-plane X-ray diffraction, small angle X-ray scattering are collected using a Rigaku Smartlab high-resolution diffractometer with Cu Kα radiation (λ=1.5416Å). The scattering curve is fit using Rigaku NANO-Solver software (shown in red line) with a spherical model and particle size distribution corresponding to the Schultz distribution function. Atomic force microscopy images are obtained using a MFP-3D AFM (Asylum Research). Temperature-dependent resistivity measurements are performed using a variable temperature

microprobe system K20 from MMR technologies coupled with a HP 4145B semiconductor parameter analyzer.

Optical characterization. Variable temperature specular reflectance spectra are collected using a Fourier-transform infrared (FTIR) spectrometer with a Seagull variable angle reflection accessory (Harrick Scientific) equipped with the aluminum heating stage. Ellipsometry spectra of VO_2 on quartz are collected using a M-2000 ellipsometer (J.A. Woollam Co.). For the ellipsometric measurement, the complex reflectance ratio is measured from 370 to 1680 nm at 45°, 55°, 65°, and 75°. Dielectric functions of VO_2 thin-films deposited on SiO_2/Si wafers are extracted by fitting with Drude-Lorentz oscillators using the CompleteEASE software package (J.A. Woollam Co.). Full-wave electromagnetic field calculations are performed using the commercially available simulation software package FDTD Solutions from Lumerical, Inc. A unit cell of the investigated structure is simulated using periodic boundary conditions along the x and y axes, and perfectly matched layers along the direction of propagation of the electromagnetic waves (z axis). Plane waves are launched incident to the unit cell along the +z direction, and transmittance is monitored with a power monitor placed behind the structure. Electric and magnetic fields are detected within the frequency profile monitors. To model VO_2 nanocrystals in the simulations, we use measured dispersion data.

7. REFERENCES

(1)   Murray, C. B.; Norris, D. J.; Bawendi, M. G. *J. Am. Chem. Soc.* **1993**, *115*, 8706-8715.

(2)   Murray, C. B.; Kagan, C. R.; Bawendi, M. G. *Annu. Rev. Mater. Sci.* **2000**, *30*, 545-610.

(3)   Talapin, D. V.; Lee, J.-S.; Kovalenko, M. V.; Shevchenko, E. V. *Chem. Rev.* **2010**, *110*, 389-458.

(4)   Alivisatos, A. P. *Science* **1996**, *271*, 933-937.

(5)   Burda, C.; Chen, X.; Narayanan, R.; El-Sayed, M. A. *Chem. Rev.* **2005**, *105*, 1025-1102.

(6)   Niederberger, M. *Acc. Chem. Res.* **2007**, *40*, 793-800.

(7)   Yin, Y.; Alivisatos, A. P. *Nature* **2005**, *437*, 664-670.

(8)   Taleb, A.; Petit, C.; Pileni, M. P. *Chem. Mater.* **1997**, *9*, 950-959.

(9)   Park, J.; An, K.; Hwang, Y.; Park, J.-G.; Noh, H.-J.; Kim, J.-Y.; Park, J.-H.; Hwang, N.-M.; Hyeon, T. *Nat. Mater.* **2004**, *3*, 891-895.

(10)   Kwon, S. G.; Piao, Y.; Park, J.; Angappane, S.; Jo, Y.; Hwang, N.-M.; Park, J.-G.; Hyeon, T. *J. Am. Chem. Soc.* **2007**, *129*, 12571-12584.

(11)   Kwon, S. G.; Hyeon, T. *Acc. Chem. Res.* **2008**, *41*, 1696-1709.

(12)   Haase, M.; Schäfer, H. *Angew. Chem. Int. Ed.* **2011**, *50*, 5808-5829.

(13)   Nikoobakht, B.; El-Sayed, M. A. *Chem. Mater.* **2003**, *15*, 1957-1962.

(14)   Petroski, J. M.; Wang, Z. L.; Green, T. C.; El-Sayed, M. A. *The Journal of Physical Chemistry B* **1998**, *102*, 3316-3220.

(15)   Xiong, Y.; McLellan, J. M.; Chen, J.; Yin, Y.; Li, Z.-Y.; Xia, Y. *J. Am. Chem. Soc.* **2005**, *127*, 17118-17127.

(16)   Huang, J.; Kovalenko, M. V.; Talapin, D. V. *J. Am. Chem. Soc.* **2010**, *132*, 15866.

(17)   Gao, J.; Bender, C. M.; Murphy, C. J. *Langmuir* **2003**, *19*, 9065-9070.

(18)   Cho, K.-S.; Talapin, D. V.; Gaschler, W.; Murray, C. B. *J. Am. Chem. Soc.* **2005**, *127*, 7140-7147.

(19)   Son, D. H.; Hughes, S. M.; Yin, Y.; Alivisatos, A. P. *Science* **2004**, *306*, 1009-1012.

(20)   Deka, S.; Miszta, K.; Dorfs, D.; Genovese, A.; Bertoni, G.; Manna, L. *Nano Lett.* **2010**, *10*, 3770-3776.

(21)   Jana, N. R.; Gearheart, L.; Murphy, C. J. *The Journal of Physical Chemistry B* **2001**, *105*, 4065-4067.

(22)   Sun, Y.; Xia, Y. *Adv. Mater.* **2002**, *14*, 833-837.

(23)   Michael B. Sigman , J.; Ghezelbash, A.; Hanrath, T.; Saunders, A. E.; Lee, F.; Korgel, B. A. *J. Am. Chem. Soc.* **2003**, *125*, 16050-16057.

(24)   Lee, N.; Choi, Y.; Lee, Y.; Park, M.; Moon, W. K.; Choi, S. H.; Hyeon, T. *Nano Lett.* **2012**, *12*, 3127-3131.

(25)   Manna, L.; Scher, E. C.; Alivisatos, A. P. *J. Am. Chem. Soc.* **2000**, *122*, 12700-12706.

(26)   Tao, A. R.; Habas, S.; Yang, P. *Small* **2008**, *4*, 310-325.

(27)   Peng, X.; Manna, L.; Yang, W.; Wickham, J.; Scher, E.; Kadavanich, A.; Alivisatos, A. P. *Nature* **2000**, *404*, 59-61.

(28)   Ithurria, S.; Tessier, M. D.; Mahler, B.; Lobo, R. P. S. M.; Dubertret, B.; Efros, A. L. *Nat. Mater.* **2011**, *10*, 936-941.

(29)   Jun, Y.-w.; Huh, Y.-M.; Cho, J.-s.; Lee, J.-H.; Song, H.-T.; Kim, S.; Yoon, S.; Kim, K.-S.; Shin, J.-S.; Suh, J.-S.; Cheon, J. *J. Am. Chem. Soc.* **2005**, *127*, 5732-5733.

(30)   Huh, Y.-M.; Jun, Y.-w.; Song, H.-T.; Kim, S.; Choi, J.-s.; Lee, J.-H.; Yoon, S.; Kim, K.-S.; Shin, J.-S.; Suh, J.-S.; Cheon, J. *J. Am. Chem. Soc.* **2005**, *127*, 12387-12391.

(31)   Bünzli, J.-C. G.; Piguet, C. *Chem. Soc. Rev.* **2005**, *34*, 1048-1077.

(32)   Auzel, F. *Chem. Rev.* **2004**, *104*, 139-174.

(33)   Wegh, R. T.; Donker, H.; Oskam, K. D.; Meijerink, A. *Science* **1999**, *283*, 663-666.

(34)   Dijk, J. M. F. v.; Schuurmans, M. F. H. *J. Chem. Phys.* **1983**, *78*, 5317.

(35)   Richards, B. S. *Sol. Energy Mater. Sol. Cells* **2006**, *90*, 1189-1207.

(36)   Güdel, H. U.; Pollnau, M. *J. Alloys Compd.* **2000**, *303-304*, 307-315.

(37)   Blasse, G.; Grabmaier, B. C. *Luminescent Materials*; Springer-Verlag: Berlin, 1994.

(38)   Heer, S.; Kömpe, K.; Güdel, H.-U.; Haase, M. *Adv. Mater.* **2004**, *16*, 2102-2105.

(39)   Wang, F.; Liu, X. *Chem. Soc. Rev.* **2009**, *38*, 976-989.

(40)   Zhang, Y.-W.; Sun, X.; Si, R.; You, L.-P.; Yan, C.-H. *J. Am. Chem. Soc.* **2005**, *127*, 3260-3261.

(41)   Roberts, J. E. *J. Am. Chem. Soc.* **1961**, *83*, 1087-1088.

(42)   Boyer, J.-C.; Cuccia, L. A.; Capobianco, J. A. *Nano Lett.* **2007**, *7*, 847-852.

(43)   Mai, H.-X.; Zhang, Y.-W.; Si, R.; Yan, Z.-G.; Sun, L.-d.; You, L.-P.; Yan, C.-H. *J. Am. Chem. Soc.* **2006**, *128*, 6429-6436.

(44)   Johnson, N. J. J.; Oakden, W.; Stanisz, G. J.; Prosser, R. S.; Veggel, F. C. J. M. v. *Chem. Mater.* **2011**, *23*, 3714-3722.

(45)   Mahalingam, V.; Vetrone, F.; Naccache, R.; Speghini, A.; Capobianco, J. A. *Adv. Mater.* **2009**, *21*, 4025-4028.

(46)   Sun, X.; Zhang, Y.-W.; Du, Y.-P.; Yan, Z.-G.; Si, R.; You, L.-P.; Yan, C.-H. *Chem. Eur. J.* **2006**, *13*, 2320-2322.

(47)   Gai, S.; Li, C.; Yang, P.; Lin, J. *Chem. Rev.* **2014**, *114*, 2343-2389.

(48)   Wu, S.; Han, G.; Milliron, D. J.; Aloni, S.; Altoe, V.; Talapin, D. V.; Cohen, B. E.; Schuck, P. J. *Proc. Natl. Acad. Sci. U. S. A.* **2009**, *106*, 10917-10926.

(49)   Caravan, P.; Ellison, J. J.; McMurry, T. J.; Lauffer, R. B. *Chem. Rev.* **1999**, *99*, 2293-2352.

(50)   Caravan, P. *Chem. Soc. Rev.* **2006**, *35*, 512-523.

(51)   Na, H. B.; Song, I. C.; Hyeon, T. *Adv. Mater.* **2009**, *21*, 2133-2148.

(52)   Na, H. B.; Hyeon, T. *J. Mater. Chem.* **2009**, *19*, 6267-6273.

(53)   Pöselt, E.; Kloust, H.; Tromsdorf, U.; Janschel, M.; Hahn, C.; Maßlo, C.; Weller, H. *ACS Nano* **2012**, *6*, 1619-1624.

(54)   Yoon, T.-J.; Lee, H.; Shao, H.; Hilderbrand, S. A.; Weissleder, R. *Angew. Chem. Int. Ed.* **2011**, *23*, 4793-4797.

(55)   Perez, J. M.; Josephson, L.; O'Loughlin, T.; Högemann, D.; Weissleder, R. *Nat. Nanotechnol.* **2002**, *20*, 816-820.

(56)   Josephson, L.; Perez, J. M.; Weissleder, R. *Angew. Chem. Int. Ed.* **2001**, *40*, 3204-3206.

(57)   Matsumura, Y.; Maeda, H. *Cancer Res.* **1986**, *46*, 6387-6392.

(58)   Jiang, W.; Kim, B. Y. S.; Rutka, J. T.; Chan, W. C. W. *Nat. Nanotechnol.* **2008**, *3*, 145-150.

(59)   Adriani, G.; Tullio, M. D. d.; Ferrari, M.; Hussain, F.; Pascazio, G.; Liu, X.; Decuzzi, P. *Biomaterials* **2012**, *33*, 5504-5513.

(60)   Maeda, H.; Wua, J.; Sawaa, T.; Matsumurab, Y.; Horic, K. *J. Controlled Release* **2000**, *65*, 271-284.

(61)   Albanese, A.; Peter S. Tang; Chan, W. C. W. *Annu. Rev. Biomed. Eng.* **2012**, *14*, 1.

(62)   Muro, S.; Garnacho, C.; Champion, J. A.; Leferovich, J.; Gajewski, C.; Schuchman, E. H.; Mitragotri, S.; Muzykantov, V. R. *Mol. Ther.* **2008**, *16*, 1450-1458.

(63)   Gratton, S. E. A.; Ropp, P. A.; Pohlhaus, P. D.; Luft, J. C.; Madden, V. J.; Napier, M. E.; DeSimone, J. M. *Proc. Natl. Acad. Sci. USA* **2008**, *105*, 11613-11618.

(64)   Chithrani, B. D.; Ghazani, A. A.; Chan, W. C. W. *Nano Lett.* **2006**, *6*, 662-668.

(65)   Qiua, Y.; Liua, Y.; Wanga, L.; Xua, L.; Baia, R.; Jib, Y.; Wub, X.; Zhaoa, Y.; Lic, Y.; Chen, C. *Biomaterials* **2010**, *31*, 7606-7619.

(66)   Zhang, Y.; Tekobo, S.; Tu, Y.; Zhou, Q.; Jin, X.; Dergunov, S. A.; Pinkhassik, E.; Yan, B. *ACS Appl. Mater. Interfaces* **2012**, *4*, 4099–4105.

(67)   Adriani, G.; Tullio, M. D. d.; Ferrari, M.; Hussain, F.; Pascazio, G.; Liu, X.; Decuzzi, P. *Biomaterials* **2012**, *33*, 5504.

(68)   Ji, Z.; Wang, X.; Zhang, H.; Lin, S.; Meng, H.; Sun, B.; George, S.; Xia, T.; Nel, A. E.; Zink, J. I. *ACS Nano* **2012**, *6*, 5366-5380.

(69)   Derfus, A. M.; Chan, W. C. W.; Bhatia, S. N. *Nano Lett.* **2004**, *4*, 11.

(70)   Colvin, V. L. *Nat. Biotechnol.* **2003**, *21*, 1166-1170.

(71)   Shevchenko, E. V.; Talapin, D. V.; Kotov, N. A.; O'Brien, S.; Murray, C. B. *Nature* **2005**, *439*, 55-59.

(72)   Evers, W. H.; Friedrich, H.; Filion, L.; Dijkstra, M.; Vanmaekelbergh, D. *Angew. Chem. Int. Ed.* **2009**, *48*, 9655-9657.

(73)   Philp, D.; Stoddart, J. F. *Angew. Chem. Int. Ed.* **2003**, *35*, 1154-1196.

(74)   Talapin, D. V.; Shevchenko, E. V.; Murray, C. B.; Titov, A. V.; Král, P. *Nano Lett.* **2007**, *7*, 1213-1219.

(75)   Shevchenko, E. V.; Talapin, D. V.; Murray, C. B.; O'Brien, S. *J. Am. Chem. Soc.* **2006**, *128*, 3620-3637.

(76)   Chen, Z.; O'Brien, S. *ACS Nano* **2008**, *2*, 1219-1229.

(77)   Bodnarchuk, M. I.; Kovalenko, M. V.; Heiss, W.; Talapin, D. V. *J. Am. Chem. Soc.* **2010**, *132*, 11967-11977.

(78)   Evers, W. H.; Nijs, B. D.; Filion, L.; Castillo, S.; Dijkstra, M.; Vanmaekelbergh, D. *Nano Lett.* **2010**, *10*, 4235-4241.

(79)   Gabriel, J.-C. P.; Davidson, P. *Top. Curr. Chem.* **2003**, *226*, 119-172.

(80)   Murphy, C. J.; Sau, T. K.; Gole, A. M.; Orendorff, C. J.; Gao, J.; Gou, L.; Hunyadi, S. E.; Li, T. *J. Phys. Chem. B* **2005**, *109*, 13857-13870.

(81)   Damasceno, P. F.; Engel, M.; Glotzer, S. C. *Science* **2012**, *337*, 453-457.

(82)   Glotzer, S. C.; Solomon, M. J. *Nat. Mater.* **2007**, *6*, 557-562.

(83)   Agarwal, U.; Escobedo, F. A. *Nat. Mater.* **2011**, *10*, 230-235.

(84)   John, B. S.; Juhlin, C.; Escobedo, F. A. *J. Chem. Phys.* **2008**, *128*, 044909.

(85)   Kooij, F. M. v. d.; Kassapidou, K.; Lekkerkerker, H. N. W. *Nature* **2000**, *406*, 868-871.

(86)   Santos, A.; Millan, J. A.; Glotzer, S. C. *Nanoscale* **2012**, *4*, 2640-2650.

185

(87)   Peroukidis, S. D.; Vanakaras, A. G.; Photinos, D. J. *J. Mater. Chem.* **2010**, *20*, 10495-10502.

(88)   Kleshchanok, D.; Petukhov, A. V.; Holmqvist, P.; Byelov, D. V.; Lekkerkerker, H. N. W. *Langmuir* **2010**, *26*, 13614-13621.

(89)   Henzie, J.; Grünwald, M.; Widmer-Cooper, A.; Geissler, P. L.; Yang, P. *Nat. Mater.* **2012**, *11*, 131-137.

(90)   Wang, L.; Xu, L.; Kuang, H.; Xu, C.; Kotov, N. A. *Acc. Chem. Res.* **2012**, *45*, 1916-1926.

(91)   Ye, X.; Collins, J. E.; Kang, Y.; Chen, J.; Chen, D. T. N.; Yodh, A. G.; Murray, C. B. *Proc. Natl. Acad. Sci. U. S. A.* **2010**, *107*, 22430-22435.

(92)   Sacanna, S.; Pine, D. J. *Curr. Opin. Colloid Interface Sci.* **2011**, *16*, 96-105.

(93)   Sacanna, S.; Irvine, W. T. M.; Chaikin, P. M.; Pine, D. J. *Nature* **2010**, *464*, 575-578.

(94)   Jones, M. R.; Macfarlane, R. J.; Lee, B.; Zhang, J.; Young, K. L.; Senesi, A. J.; Mirkin, C. A. *Nat. Mater.* **2010**, *9*, 913-917.

(95)   Grzelczak, M.; Vermant, J.; Furst, E. M.; Liz-Marzán, L. M. *ACS Nano* **2010**, *4*, 3591-3605.

(96)   Quan, Z.; Fang, J. *Nano Today* **2010**, *5*, 390-411.

(97)   Baker, J. L.; Widmer-Cooper, A.; Toney, M. F.; Geissler, P. L.; Alivisatos, A. P. *Nano Lett.* **2010**, *10*, 195-201.

(98)   Ryan, K. M.; Mastroianni, A.; Stancil, K. A.; Liu, H.; Alivisatos, A. P. *Nano Lett.* **2006**, *6*, 1479-1482.

(99)   Baranov, D.; Fiore, A.; Huis, M. v.; Giannini, C.; Falqui, A.; Lafont, U.; Zandbergen, H.; Zanella, M.; Cingolani, R.; Manna, L. *Nano Lett.* **2010**, *10*, 743-749.

(100)   Kim, F.; Kwan, S.; Akana, J.; Yang, P. *J. Am. Chem. Soc.* **2001**, *123*, 4360–4361.

(101)   Cao, Y. C. *J. Am. Chem. Soc.* **2004**, *126*, 7456-7457.

(102)   Saunders, A. E.; Ghezelbash, A.; Smilgies, D.-M.; Michael B. Sigman, J.; Korgel, B. A. *Nano Lett.* **2006**, *6*, 2959-2963.

(103)   Sun, X.; Zhang, Y.-W.; Du, Y.-P.; Yan, Z.-G.; Si, R.; You, L.-P.; Yan, C.-H. *Chem. Eur. J.* **2006**, *13*, 2320.

(104)   Yu, T.; Joo, J.; Park, Y. I.; Hyeon, T. *J. Am. Chem. Soc.* **2006**, *128*, 1786-1787.

(105)   Zhuang, Z.; Peng, Q.; Zhang, B.; Li, Y. *J. Am. Chem. Soc.* **2008**, *130*, 10482-10483.

(106)   Huo, Z.; Tsung, C.-K.; Huang, W.; Fardy, M.; Yan, R.; Zhang, X.; Li, Y.; Yang, P. *Nano Lett.* **2009**, *9*, 1260-1264.

(107)   Talapin, D. V.; Shevchenko, E. V.; Murray, C. B.; Kornowski, A.; Förster, S.; Weller, H. *J. Am. Chem. Soc.* **2004**, *126*, 12984-12988.

(108)   Sun, B.; Sirringhaus, H. *J. Am. Chem. Soc.* **2006**, *128*, 16231-16237.

(109)   Murphy, C. J.; Sau, T. K.; Gole, A. M.; Orendorff, C. J.; Gao, J.; Gou, L.; Hunyadi, S. E.; Li, T. *J. Phys. Chem. B* **2005**, *109*, 13857-13870.

(110)   Xia, Y.; Xiong, Y.; Lim, B.; Skrabalak, S. E. *Angew. Chem. Int. Ed.* **2008**, *48*, 60-103.

(111)   Kim, B. H.; Lee, N.; Kim, H.; An, K.; Park, Y. I.; Choi, Y.; Shin, K.; Lee, Y.; Kwon, S. G.; Na, H. B.; Park, J.-G.; Ahn, T.-Y.; Kim, Y.-W.; Moon, W. K.; Choi, S. H.; Hyeon, T. *J. Am. Chem. Soc.* **2011**, *133*, 12624-12631.

(112)   Tromsdorf, U. I.; Bruns, O. T.; Salmen, S. C.; Beisiegel, U.; Weller, H. *Nano Lett.* **2009**, *9*, 4434-4440.

(113)   Michalet, X.; Pinaud, F. F.; Bentolila, L. A.; Tsay, J. M.; Doose, S.; Li, J. J.; Sundaresan, G.; Wu, A. M.; Gambhir, S. S.; Weiss, S. *Science* **2005**, *307*, 538-544.

(114)   Gao, X.; Cui, Y.; Levenson, R. M.; Chung, L. W. K.; Nie, S. *Nat. Biotechnol.* **2004**, *22*, 969-976.

(115)   Cheon, J.; Lee, J.-H. *Acc. Chem. Res.* **2008**, *41*, 1630-1640.

(116)   Choi, J.-s.; Park, J. C.; Nah, H.; Woo, S.; Oh, J.; Kim, K. M.; Cheon, G. J.; Chang, Y.; Yoo, J.; Cheon, J. *Angew. Chem. Int. Ed.* **2008**, *47*, 6259-6262.

(117)   Kim, J.; Piao, Y.; Hyeon, T. *Chem. Soc. Rev.* **2009**, *38*, 372-390.

(118)   Yoo, D.; Lee, J.-H.; Shin, T.-H.; Cheon, J. *Acc. Chem. Res.* **2011**, *44*, 863-874.

(119)   Zhoua, J.; Suna, Y.; Dub, X.; Xionga, L.; Hua, H.; Li, F. *Biomaterials* **2010**, *31*, 3287-3295.

(120)   Wang, G.; Peng, Q.; Li, Y. *Acc. Chem. Res.* **2011**, *44*, 322-332.

(121)   Nyk, M.; Kumar, R.; Ohulchanskyy, T. Y.; Bergey, E. J.; Prasad, P. N. *Nano Lett.* **2008**, *8*, 3834-3838.

(122)   Boyer, J.-C.; Manseau, M.-P.; Murray, J. I.; Veggel, F. C. J. M. v. *Langmuir* **2010**, *26*, 1157-1164.

(123)   Das, G. K.; Johnson, N. J. J.; Cramen, J.; Blasiak, B.; Latta, P.; Tomanek, B.; Veggel, F. C. J. M. v. *J. Phys. Chem. Lett.* **2012**, *3*, 524-529.

(124)   Zhang, Q.; Yan, B. *Inorg. Chem.* **2010**, *49*, 6834-6839.

(125)   Si, R.; Zhang, Y.-W.; You, L.-P.; Yan, C.-H. *Angew. Chem. Int. Ed.* **2005**, *44*, 3256-3260.

(126)   Mai, H.-X.; Zhang, Y.-W.; Si, R.; Yan, Z.-G.; Sun, L.-d.; You, L.-P.; Yan, C.-H. *J. Am. Chem. Soc.* **2006**, *128*, 6426-6436.

(127)   Shao, X.; Agarwal, A.; Rajian, J. R.; Kotov, N. A.; Wang, X. *Nanotechnology* **2011**, *22*, 135102.

(128)   Wang, F.; Han, Y.; Lim, C. S.; Lu, Y.; Wang, J.; Xu, J.; Chen, H.; Zhang, C.; Hong, M.; Liu, X. *Nature* **2010**, *463*, 1061-1065.

(129)   Chatterjeea, D. K.; Rufaihaha, A. J.; Zhang, Y. *Biomaterials* **2008**, *29*, 937-943.

(130)   Boyer, J.-C.; Vetrone, F.; Cuccia, L. A.; Capobianco, J. A. *J. Am. Chem. Soc.* **2006**, *128*, 7444-7445.

(131)   Wang, F.; Liu, X. *J. Am. Chem. Soc.* **2008**, *130*, 5642-5643.

(132)   Sun, C.; Pratx, G.; Carpenter, C. M.; Liu, H.; Cheng, Z.; Gambhir, S. S.; Xing, L. *Adv. Mater.* **2011**, *23*, H195-H199.

(133)   Carpenter, C. M.; Sun, C.; Pratx, G.; Liu, H.; Cheng, Z.; Xing, L. *Opt. Express* **2012**, *20*, 11598-11604.

(134)   Liu, Y.; Chen, W.; Wang, S.; Joly, A. G.; Westcott, S.; Woo, B. K. *J. Appl. Phys.* **2008**, *2008*, 063105.

(135)   Shevchenko, E. V.; Talapin, D. V.; Schnablegger, H.; Kornowski, A.; Festin, O.; Svedlindh, P.; Haase, M.; Weller, H. *J. Am. Chem. Soc.* **2003**, *125*, 9090-101.

(136)   Rieker, T.; Hanprasopwattana, A.; Datye, A.; Hubbard, P. *Langmuir* **1999**, *15*, 638-641.

(137)   Borchert, H.; Shevchenko, E. V.; Robert, A.; Mekis, I.; Kornowski, A.; Grübel, G.; Weller, H. *Langmuir* **2005**, *21*, 1931-1936.

(138)   Kotlarchyk, M.; Chen, S. H. *J. Chem. Phys.* **1983**, *79*, 2461-2469.

(139)   Johnson, N. J. J.; Korinek, A.; Dong, C.; Veggel, F. C. J. M. v. *J. Am. Chem. Soc.* **2012**, *134*, 11068-11071.

(140)   Zalkin, A.; Templeton, D. H. *J. Am. Chem. Soc.* **1953**, *75*, 2453-2458.

(141)   Das, G. K.; Zhang, Y.; D'Silva, L.; Padmanabhan, P.; Heng, B. C.; Loo|, J. S. C.; Selvan, S. T.; Bhakoo, K. K.; Tan, T. T. Y. *Chem. Mater.* **2011**, *23*, 2439-2446.

(142)   Bridot, J.-L.; Faure, A.-C.; Laurent, S.; Rivière, C.; Billotey, C.; Hiba, B.; Janier, M.; Josserand, V.; Coll, J.-L.; Elst, L. V.; Muller, R.; Roux, S.; Perriat, P.; Tillement, O. *J. Am. Chem. Soc.* **2007**, *129*, 5076-5084.

(143)   Sarma, V. R.; Silverton, E. W.; Davies, D. R.; Terry, W. D. *The Journal of Biological Chemistry* **1971**, *246*, 3753-3759.

(144)   Tsunekawa, S.; Ito, S.; Kawazoe, Y. *Appl. Phys. Lett.* **2004**, *85*, 3845.

(145)   Norek, M.; Kampert, E.; Zeitler, U.; Peters, J. A. *J. Am. Chem. Soc.* **2008**, *130*, 5335-5340.

(146)   Dong, A.; Ye, X.; Chen, J.; Kang, Y.; Gordon, T.; Kikkawa, J. M.; Murray, C. B. *J. Am. Chem. Soc.* **2011**, *133*, 998-1006.

(147)   Hall, B. D.; Monot, R. *Computers in Physics* **1991**, *5*, 414.

(148)   Eykyn, T. R.; Payne, G. S.; Leach, M. O. *Phys. Med. Biol.* **2005**, *50*, N371-N376.

(149)   Lauffer, R. B. *Chem. Rev.* **1987**, *87*, 901-927.

(150)   Nel, A. E.; Mädler, L.; Velegol, D.; Xia, T.; Hoek, E. M. V.; Somasundaran, P.; Klaessig, F.; Castranova, V.; Thompson, M. *Nat. Mater.* **2008**, *8*, 543-557.

(151)   Chithrani, B. D.; Chan, W. C. W. *Nano Lett.* **2007**, *7*, 1542-1550.

(152)   Verma, A.; Uzun, O.; Hu, Y.; Hu, Y.; Han, H.-S.; Watson, N.; Chen, S.; Irvine, D. J.; Stellacc, F. *Nat. Mater.* **2008**, *7*, 588-595.

(153)   Yoon, T.-J.; Lee, H.; Shao, H.; Weisslede, R. *Angew. Chem. Int. Ed.* **2011**, *50*, 4663-4666.

(154)   Gambhir, S. S. *Nat. Rev. Cancer* **2002**, *2*, 683-693.

(155)   Gao, X.; Cui, Y.; Levenson, R. M.; Chung, L. W. K.; Nie, S. *Nat. Biotechnol.* **2004**, *22*, 969-976.

(156)   Weissleder, R.; Pittet, M. J. *Nature* **2008**, *452*, 580-589.

(157)   Liu, Y.; Welch, M. J. *Bioconjugate Chem.* **2012**, *23*, 671-682.

(158)   Cho, E. C.; Glaus, C.; Chen, J.; Welch, M. J.; Xia, Y. *Trends Mol. Med.* **2010**, *16*, 561-573.

(159)   Burda, C.; Chen, X.; Narayanan, R.; El-Sayed, M. A. *Chem. Rev.* **2005**, *105*, 1025-1102.

(160)   Mai, H.-X.; Zhang, Y.-W.; Si, R.; Yan, Z.-G.; Sun, L.-d.; You, L.-P.; Yan, C.-H. *J. Am. Chem. Soc.* **2006**, *128*, 6426-6436.

(161)   Wong, R. M.; Gilbert, D. A.; Liu, K.; Louie, A. Y. *ACS Nano* **2012**, *6*, 3461-3467.

(162)   Freund, B.; Tromsdorf, U. I.; Bruns, O. T.; Heine, M.; Giemsa, A.; Bartelt, A.; Salmen, S. C.; Raabe, N.; Heeren, J.; Ittrich, H.; Reimer, R.; Hohenberg, H.; Schumacher, U.; Weller, H.; Nielsen, P. *ACS Nano* **2012**, *6*, 7318-7325.

(163)   Marmorato, P.; Simonelli, F.; Abbas, K.; Kozempel, J.; Holzwarth, U.; Franchini, F.; Ponti, J.; Gibson, N.; Rossi, F. *J. Nanopart. Res.* **2011**, *13*, 6707-6717.

(164)   Yang, Y.; Sun, Y.; Cao, T.; Peng, J.; Liu, Y.; Wu, Y.; Feng, W.; Zhang, Y.; Li, F. *Biomaterials* **2013**, *34*, 774-783.

(165)   Wang, Y.; Liu, Y.; Luehmann, H.; Xia, X.; Wan, D.; Cutler, C.; Xia, Y. *Nano Lett.* **2013**, *13*, 581-585.

(166)   Sun, Y.; Yu, M.; Liang, S.; Zhang, Y.; Li, C.; Mou, T.; Yang, W.; Zhang, X.; Li, B.; Huang, C.; Li, F. *Biomaterials* **2011**, *32*, 2999-3007.

(167)   Cremonesi, M.; Ferrari, M.; Paganelli, G.; Rossi, A.; Chinol, M.; Bartolomei, M.; Prisco, G.; Tosi, G. *Eur. J. Nucl. Med. Mol. Imag.* **2006**, *33*, 1321-1327.

(168)   Giammarile, F.; Bodei, L.; Chiesa, C.; Flux, G.; Forrer, F.; Kraeber-Bodere, F.; Brans, B.; Lambert, B.; Konijnenberg, M.; Borson-Chazot, F.; Tennvall, J.; Luster, M. *Eur. J. Nucl. Med. Mol. Imag.* **2011**, *38*, 1393-1406.

(169)   Lhommel, R.; van Elmbt, L.; Goffette, P.; Van den Eynde, M.; Jamar, F.; Pauwels, S.; Walrand, S. *Eur. J. Nucl. Med. Mol. Imag.* **2010**, *37*, 1654-62.

(170)   Elschot, M.; Vermolen, B. J.; Lam, M. G.; de Keizer, B.; van den Bosch, M. A.; de Jong, H. W. *PloS ONE* **2013**, *8*, e55742.

(171)   Liu, H.; Ren, G.; Miao, Z.; Zhang, X.; Tang, X.; Han, P.; Gambhir, S. S.; Cheng, Z. *PloS ONE* **2010**, *5*, e9470.

(172)   Paik, T.; Ko, D.-K.; Gordon, T. R.; Doan-Nguyen, V.; Murray, C. B. *ACS Nano* **2011**, *5*, 8322-8330.

(173)   Paik, T.; Gordon, T. R.; Prantner, A. M.; Yun, H.; Murray, C. B. *ACS Nano* **2013**, *7*, 2850-2859.

(174)   Alkilany, A. M.; Nagaria, P. K.; Hexel, C. R.; Shaw, T. J.; Murphy, C. J.; Wyatt, M. D. *Small* **2009**, *5*, 701-708.

(175)   Verma, A.; Stellacci, F. *Small* **2010**, *6*, 12-21.

(176)   Serda, R. E.; Gu, J.; Bhavane, R. C.; Liu, X.; Chiappini, C.; Decuzzi, P.; Ferrari, M. *Biomaterials* **2009**, *30*, 2440-2448.

(177)   Robertson, R.; Germanos, M. S.; Li, C.; Mitchell, G. S.; Cherry, S. R.; Silva, M. D. *Phys. Med. Biol.* **2009**, *54*, N355-N365.

(178)   Thorek, D. L.; Robertson, R.; Bacchus, W. A.; Hahn, J.; Rothberg, J.; Beattie, B. J.; Grimm, J. *Am. J. Nucl. Med. Mol. Imaging* **2012**, *2*, 163-173.

(179)   Boschi, F.; Spinelli, A. E. *RSC Advances* **2012**, *2*, 11049-11052.

(180)   Dothager, R. S.; Goiffon, R. J.; Jackson, E.; Harpstrite, S.; Piwnica-Worms, D. *PloS ONE* **2010**, *5*, e13300.

(181)   Louie, A. *Chem. Rev.* **2010**, *110*, 3146-3195.

(182)   Bottrill, M.; Kwok, L.; Long, N. J. *Chem. Soc. Rev.* **2006**, *35*, 557-571.

(183)   Das, G. K.; Johnson, N. J. J.; Cramen, J.; Blasiak, B.; Latta, P.; Tomanek, B.; Veggel, F. C. J. M. v. *J. Phys. Chem. Lett* **2012**, *3*, 524-529.

(184)   Lauffer, R. B. *Chem. Rev.* **1987**, *87*, 901-927.

(185)   Eykyn, T. R.; Payne, G. S.; Leach, M. O. *Phys. Med. Biol.* **2005**, *50*, N371-N376.

(186)   Murray, C. B.; Kagan, C. R.; Bawendi, M. G. *Science* **1995**, *270*, 1335-1338.

(187)   Collier, C. P.; Vossmeyer, T.; Heath, J. R. *Annu. Rev. Phys. Chem.* **1998**, *49*, 371-404.

(188)   Urban, J. J.; Talapin, D. V.; Shevchenko, E. V.; Kagan, C. R.; Murray, C. B. *Nature Materials* **2007**, *6*, 115-121.

(189)   Dong, A.; Chen, J.; Vora, P. M.; Kikkawa, J. M.; Murray, C. B. *Nature* **2010**, *466*, 474-477.

(190)   Chen, J.; Dong, A.; Cai, J.; Ye, X.; Kang, Y.; Kikkawa, J. M.; Murray, C. B. *Nano Lett.* **2010**, *10*, 5103-5108.

(191)   Ye, X.; Chen, J.; Diroll, B. T.; Murray, C. B. *Nano Lett.* **2013**, *13*, 1291-1297.

(192)   Shevchenko, E. V.; Ringler, M.; Schwemer, A.; Talapin, D. V.; Klar, T. A.; Rogach, A. L.; Feldmann, J.; Alivisatos, A. P. *J. Am. Chem. Soc.* **2008**, *130*, 3274-3275.

(193)   Kang, Y.; Ye, X.; Chen, J.; Qi, L.; Diaz, R. E.; Doan-Nguyen, V.; Xing, G.; Kagan, C. R.; Li, J.; Gorte, R. J.; Stach, E. A.; Murray, C. B. *J. Am. Chem. Soc.* **2013**, *135*, 1499-1505.

(194)   Zhang, S. *Nat. Biotechnol.* **2003**, *21*, 1171- 1178.

(195)   Kadler, K. E.; Holmes, D. F.; Trotter, J. A.; Chapman, J. A. *Biochem. J* **1996**, *316*, 1-11.

(196)   Hartgerink, J. D.; Beniash, E.; Stupp, S. I. *Science* **2001**, *294*, 1684-1688.

(197)   Ghezelbash, A.; Koo, B.; Korgel, B. A. *Nano Lett.* **2006**, *6*, 1832-1836.

(198)   Si, R.; Zhang, Y.-W.; Zhou, H.-P.; Sun, L.-D.; Yan, C.-H. *Chem. Mater.* **2007**, *19*, 18-27.

(199)   Miszta, K.; Graaf, J. d.; Bertoni, G.; Dorfs, D.; Brescia, R.; Marras, S.; Ceseracciu, L.; Cingolani, R.; Roij, R. v.; Dijkstra, M.; Manna, L. *Nat. Mater.* **2011**, *10*, 872-876.

(200)   Qi, W.; Graaf, J. d.; Qiao, F.; Marras, S.; Manna, L.; Dijkstra, M. *Nano Lett.* **2012**, *12*, 5299-5303.

(201)   Sánchez-Iglesias, A.; Grzelczak, M.; Pérez-Juste, J.; Liz-Marzán, L. M. *Angew. Chem. Int. Ed.* **2010**, *49*, 9985-9989.

(202)   Wang, T.; Zhuang, J.; Lynch, J.; Chen, O.; Wang, Z.; Wang, X.; LaMontagne, D.; Wu, H.; Wang, Z.; Cao, Y. C. *Science* **2012**, *338*, 358-363.

(203)   Nagaoka, Y.; Wang, T.; Lynch, J.; LaMontagne, D.; Cao, Y. C. *Small* **2012**, *8*, 843-846.

(204)   Ming, T.; Kou, X.; Chen, H.; Wang, T.; Tam, H.-L.; Cheah, K.-W.; Chen, J.-Y.; Wang, J. *Angew. Chem. Int. Ed.* **2008**, *47*, 9685-9690.

(205)   Dong, A.; Chen, J.; Vora, P. M.; Kikkawa, J. M.; Murray, C. B. *Nature* **2010**, *466*, 474-477.

(206)   Ye, X.; Collins, J. E.; Kang, Y.; Chen, J.; Chen, D. T. N.; Yodh, A. G.; Murray, C. B. *Proceedings of the National Academy of Sciences* **2010**, *107*, 22430-22435.

(207)   Chaikin, P. M.; Lubensky, T. C. *Principles of Condensed Matter Physics*; Cambridge University Press: Cambridge, 1995.

(208)   Bigioni, T. P.; Lin, X.-M.; Nguyen, T. T.; Corwin, E. I.; Witten, T. A.; Jaeger, H. M. *Nature* **2006**, *5*, 265-270.

(209)   Narayanan, S.; Wang, J.; Lin, X.-M. *Phys. Rev. Lett.* **2004**, *93*, 135503.

(210)   Friedrich, H.; Gommes, C. J.; Overgaag, K.; Meeldijk, J. D.; Evers, W. H.; Nijs, B. d.; Boneschanscher, M. P.; Jongh, P. E. d.; Verkleij, A. J.; Jong, K. P. d.; Blaaderen, A. v.; Vanmaekelbergh, D. *Nano Lett.* **2009**, *9*, 2719-2724.

(211)   Bodnarchuk, M. I.; Kovalenko, M. V.; Pichler, S.; Fritz-Popovski, G.; Hesser, G.; Heiss, W. *ACS Nano* **2010**, *4*, 423-431.

(212)   Titov, A. V.; Kral, P. *Nano Lett.* **2008**, *8*, 3605-3612.

(213)   Maeda, H.; Maeda, Y. *Phys. Rev. Lett.* **2003**, *90*, 018303.

(214)   Schuster, M.; Gobel, H. *J. Phys. D: Appl. Phys.* **1995**, *28*, A270-A275.

(215)   Omote, K.; Ito, Y.; Kawamura, S. *Appl. Phys. Lett.* **2003**, *82*, 544-546.

(216)   Smilgies, D.-M. *J. Appl. Crystallogr.* **2009**, *42*, 1030-1034.

(217)   Lee, B.; Podsiadlo, P.; Rupich, S.; Talapin, D. V.; Rajh, T.; Shevchenko, E. V. *J. Am. Chem. Soc.* **2009**, *131*, 16386-16388.

(218)   Jones, M. R.; Macfarlane, R. J.; Prigodich, A. E.; Patel, P. C.; Mirkin, C. A. *J. Am. Chem. Soc.* **2011**, *133*, 18865-18869.

(219) Carbone, L.; Nobile, C.; Giorgi, M. D.; Sala, F. D.; Morello, G.; Pompa, P.; Hytch, M.; Snoeck, E.; Fiore, A.; Franchini, I. R.; Nadasan, M.; Silvestre, A. F.; Chiodo, L.; Kudera, S.; Cingolani, R.; Krahne, R.; Manna, L. *Nano Lett.* **2007**, *7*, 2942-2950.

(220) Sun, Y.; Xia, Y. *Science* **2002**, *298*, 2176-2179.

(221) Anpo, M.; Takeuchi, M. *J. Catal.* **2003**, *216*, 505-516.

(222) Chen, M. S.; Goodman, D. W. *Science* **2004**, *306*, 252-255.

(223) Yabe, S.; Satob, T. *J. Solid State Chem.* **2002**, *171*, 7-11.

(224) Grätzel, M. *Prog. Photovolt. Res. Appl.* **2000**, *8*, 171-185.

(225) Özgür, Ü.; Alivov, Y. I.; Liu, C.; Teke, A.; Reshchikov, M. A.; Doğan, S.; Avrutin, V.; Cho, S.-J.; Morkoç, H. *J. Appl. Phys.* **2005**, *98*, 041301.

(226) Whittingham, M. S. *Chem. Rev.* **2004**, *104*, 4271-4302.

(227) Gordon, T. R.; Cargnello, M.; Paik, T.; Mangolini, F.; Weber, R. T.; Fornasiero, P.; Murray, C. B. *J. Am. Chem. Soc.* **2012**, *134*, 6751-6761.

(228) Gordon, T. R.; Paik, T.; Klein, D. R.; Naik, G. V.; Caglayan, H.; Boltasseva, A.; Murray, C. B. *Nano Lett.* **2013**, *13*, 2857-2863.

(229) Niederberger, M. *Acc. Chem. Res.* **2007**, *40*, 793-800.

(230) Soukoulis, C. M.; Wegener, M. *Nat. Photonics* **2011**, *5*, 523-530.

(231) Zheludev, N. I.; Kivshar, Y. S. *Nat. Mater.* **2012**, *11*, 917-924.

(232) Boltasseva, A.; Atwater, H. A. *Science* **2011**, *331*, 290-291.

(233) Shelby, R. A.; Smith, D. R.; Schultz, S. *Science* **2001**, *292*, 77-79.

(234) Valentine, J.; Zhang, S.; Zentgraf, T.; Ulin-Avila, E.; Genov, D. A.; Bartal, G.; Zhang, X. *Nature* **2008**, *455*, 376-379.

(235) Smith, D. R.; Pendry, J. B.; Wiltshire, M. C. K. *Science* **2004**, *305*, 788-792.

(236) Pendry, J. B. *Phys. Rev. Lett.* **2000**, *85*, 3966-3969.

(237) Fang, N.; Lee, H.; Sun, C.; Zhang, X. *Science* **2005**, *308*, 534-537.

(238) Schurig, D.; Mock, J. J.; Justice, B. J.; Cummer, S. A.; Pendry, J. B.; Starr, A. F.; Smith, D. R. *Science* **2006**, *314*, 977-980.

(239) Alù, A.; Engheta, N. *Phys. Rev. E* **2005**, *72*, 016623.

(240) Liu, N.; Mesch, M.; Weiss, T.; Hentschel, M.; Giessen, H. *Nano Lett.* **2010**, *10*, 2342-2348.

(241) Anker, J. N.; Hall, W. P.; Lyandres, O.; Shah, N. C.; Zhao, J.; Duyne, R. P. V. *Nat. Mater.* **2008**, *7*, 442-453.

(242) Pryce, I. M.; Aydin, K.; Kelaita, Y. A.; Briggs, R. M.; Atwater, H. A. *Nano Lett.* **2010**, *10*, 4222-4227.

(243) Hess, O.; Pendry, J. B.; Maier, S. A.; Oulton, R. F.; Hamm, J. M.; Tsakmakidis, K. L. *Nat. Mater.* **2012**, *11*, 573-584.

(244) Boardman, A. D.; Grimalsky, V. V.; Kivshar, Y. S.; Koshevaya, S. V.; Lapine, M.; Litchinitser, N. M.; Malnev, V. N.; Noginov, M.; Rapoport, Y. G.; Shalaev, V. M. *Laser & Photon. Rev.* **2010**, *5*, 287-307.

(245) Hsiao, V. K. S.; Zheng, Y. B.; Juluri, B. K.; Huang, T. J. *20* **2008**, *18*, 3528.

(246) Krasavin, A. V.; Zheludev, N. I. *Appl. Phys. Lett.* **2004**, *84*, 1416-1418.

(247) Wang, Z.; Chumanov, G. *Adv. Mater.* **2003**, *15*, 1285-1289.

(248) Pernice, W. H. P.; Bhaskaran, H. *Appl. Phys. Lett.* **2012**, *101*, 171101.

(249) Sámson, Z. L.; MacDonald, K. F.; Angelis, F. D.; Gholipour, B.; Knight, K.; Huang, C. C.; Fabrizio, E. D.; Hewak, D. W.; Zheludev, N. I. *Appl. Phys. Lett.* **2010**, *96*, 143105.

(250)   Maaza, M.; Nemraoui, O.; Sella, C.; Beye, A. C.; Baruch-Barak, B. *Opt. Commun.* **2005**, *254*, 188-195.

(251)   Goodenough, J. B. *Annu. Rev. Mater. Sci.* **1971**, *1*, 101-138.

(252)   Morin, F. J. *Phys. Rev. Lett.* **1959**, *3*, 34-36.

(253)   Tselev, A.; Luk'yanchuk, I. A.; Ivanov, I. N.; Budai, J. D.; Tischler, J. Z.; Strelcov, E.; Kolmakov, A.; Kalinin, S. V. *Nano Lett.* **2010**, *10*, 4409-4416.

(254)   Cao, J.; Ertekin, E.; Srinivasan, V.; Fan, W.; Huang, S.; Zheng, H.; Yim, J. W. L.; Khanal, D. R.; Ogletree, D. F.; Grossman, J. C.; Wu, J. *Nat. Nanotechnol.* **2009**, *4*, 732-737.

(255)   Ruzmetov, D.; Gopalakrishnan, G.; Ko, C.; Narayanamurti, V.; Ramanathan, S. *J. Appl. Phys.* **2010**, *107*, 114516.

(256)   Nakano, M.; Shibuya, K.; Okuyama, D.; Hatano, T.; Ono, S.; Kawasaki, M.; Iwasa, Y.; Tokura, Y. *Nature* **2012**, *487*, 459-462.

(257)   Jeong, J.; Aetukuri, N.; Graf, T.; Schladt, T. D.; Samant, M. G.; Parkin, S. S. P. *Science* **2013**, *339*, 1402-1405.

(258)   Granqvist, C. G. *Adv. Mater.* **2003**, *15*, 1789-1803.

(259)   Granqvist, C. G. *Sol. Energy Mater. Sol. Cells* **2007**, *91*, 1529-1598.

(260)   Gea, L. A.; Boatner, L. A. *Appl. Phys. Lett.* **1996**, *68*, 3081-3083.

(261)   Driscoll, T.; Kim, H.-T.; Chae, B.-G.; Kim, B.-J.; Lee, Y.-W.; Jokerst, N. M.; Palit, S.; Smith, D. R.; Ventra, M. D.; Basov, D. N. *Science* **2009**, *325*, 1518-1521.

(262)   Lee, M.-J.; Park, Y.; Suh, D.-S.; Lee, E.-H.; Seo, S.; Kim, D.-C.; Jung, R.; Kang, B.-S.; Ahn, S.-E.; Lee, C. B.; Seo, D. H.; Cha, Y.-K.; Yoo, I.-K.; Kim, J.-S.; Park, B. H. *Adv. Mater.* **2007**, *19*, 3919-3923.

(263)   Coy, H.; Cabrera, R.; Sepúlveda, N.; Fernández, F. E. *J. Appl. Phys.* **2010**, *108*, 113115.

(264)   Stefanovich, G.; Pergament, A.; Stefanovich, D. *J. Phys.: Condens. Matter* **2000**, *12*, 8837-8845.

(265)   Yang, Z.; Ko, C.; Ramanathan, S. *Annu. Rev. Mater. Res.* **2011**, *41*, 337-367.

(266)   Liu, M.; Hwang, H. Y.; Tao, H.; Strikwerda, A. C.; Fan, K.; Keiser, G. R.; Sternbach, A. J.; West, K. G.; Kittiwatanakul, S.; Lu, J.; Wolf, S. A.; Omenetto, F. G.; Zhang, X.; Nelson, K. A.; Averitt, R. D. *Nature* **2012**, *487*, 345-348.

(267)   Driscoll, T.; Palit, S.; Qazilbash, M. M.; Brehm, M.; Keilmann, F.; Chae, B.-G.; Yun, S.-J.; Kim, H.-T.; Cho, S. Y.; Jokerst, N. M.; Smith, D. R.; Basov, D. N. *Appl. Phys. Lett.* **2008**, *93*, 024101.

(268)   Kruger, B. A.; Joushaghani, A.; Poon, J. K. S. *Opt. Express* **2012**, *20*, 23598-23609.

(269)   Kats, M. A.; Blanchard, R.; Genevet, P.; Yang, Z.; Qazilbash, M. M.; Basov, D. N.; Ramanathan, S.; Capasso, F. *Opt. Lett.* **2012**, *38*, 368-370.

(270)   Dicken, M. J.; Aydin, K.; Pryce, I. M.; Sweatlock, L. A.; Boyd, E. M.; Walavalkar, S.; Ma, J.; Atwater, H. A. *Opt. Express* **2009**, *17*, 18330-8339.

(271)   Sweatlock, L. A.; Diest, K. *Opt. Express* **2012**, *20*, 8700-8709.

(272)   Béteille, F.; Morineau, R.; Livage, J.; Nagano, M. *Mater. Res. Bull.* **1997**, *32*, 1109-1117.

(273)   Partlow, D. P.; Gurkovich, S. R.; Radford, K. C.; Denes, L. J. *J. Appl. Phys.* **1991**, *70*, 443-452.

(274)   Lopez, R.; Boatner, L. A.; Haynes, T. E.; Feldman, L. C.; Haglund, R. F. *J. Appl. Phys.* **2002**, *92*, 4031-4036.

(275)   Ruzmetov, D.; Zawilski, K.; Narayanamurti, V.; Ramanathan, S. *J. Appl. Phys.* **2007**, *102*, 113715.

(276)   Guiton, B. S.; Gu, Q.; Prieto, A. L.; Gudiksen, M. S.; Park, H. *J. Am. Chem. Soc.* **2005**, *127*, 498-499.

(277)   Kim, D. H.; Kwok, H. S. *Appl. Phys. Lett.* **1994**, *65*, 3188-3190.

(278)   Jorgenson, G. V.; Lee, J. C. *Sol. Energy Mater.* **1986**, *14*, 205-214.

(279)   Sargent, E. H. *Nat. Photonics* **2009**, *3*, 325-331.

(280)   Gur, I.; Fromer, N. A.; Geier, M. L.; Alivisatos, A. P. *Science* **2005**, *310*, 462-465.

(281)   Böberl, M.; Kovalenko, M. V.; Gamerith, S.; List, E. J. W.; Heiss, W. *Adv. Mater.* **2007**, *19*, 3574-3578.

(282)   Lewis, J. A. *Curr. Opin. Solid State Mater. Sci.* **2002**, *6*, 245-250.

(283)   Katzke, H.; Tole´dano, P.; Depmeier, W. *Phys. Rev. B* **2004**, *68*, 024109.

(284)   Griffiths, C. H.; Eastwood, H. K. *J. Appl. Phys.* **1974**, *45*, 2201-2206.

(285)   Okimura, K.; Sakai, J.; Ramanathan, S. *J. Appl. Phys.* **2010**, *107*, 063503.

(286)   Fu, D.; Liu, K.; Tao, T.; Lo, K.; Cheng, C.; Liu, B.; Zhang, R.; Bechtel, H. A.; Wu, J. *J. Appl. Phys.* **2013**, *113*, 043707.

(287)   Cui, Y.; Ramanathan, S. *J. Vac. Sci. Technol., A* **2011**, *29*, 041502.

(288)   Lopez, R.; Haynes, T. E.; Boatner, L. A.; Feldman, L. C.; R. F. Haglund, J. *Phys. Rev. B* **2002**, *65*, 224113.

(289)   Appavoo, K.; Lei, D. Y.; Sonnefraud, Y.; Wang, B.; Pantelides, S. T.; Maier, S. A.; R. F. Haglund, J. *Nano Lett.* **2012**, *12*, 780-786.

(290)   Brassard, D.; Fourmaux, S.; Jean-Jacques, M.; Kieffer, J. C.; Khakania, M. A. E. *Appl. Phys. Lett.* **2005**, *87*, 051910.

(291)   Strelcov, E.; Tselev, A.; Ivanov, I.; Budai, J. D.; Zhang, J.; Tischler, J. Z.; Kravchenko, I.; Kalinin, S. V.; Kolmakov, A. *Nano Lett.* **2012**, *12*, 6198-6205.

(292)   Wei, J.; Ji, H.; Guo, W.; Nevidomskyy, A. H.; Natelson, D. *Nat. Nanotechnol.* **2012**, *7*, 357-362.

(293)   Mocatta, D.; Cohen, G.; Schattner, J.; Millo, O.; Rabani, E.; Banin, U. *Science* **2011**, *332*, 77-81.

(294)   Ba, J.; Rohlfing, D. F.; Feldhoff, A.; Brezesinski, T.; Djerdj, I.; Wark, M.; Niederberger, M. *Chem. Mater.* **2006**, *18*, 2848-2854.

(295)   Mikulec, F. V.; Kuno, M.; Bennati, M.; Hall, D. A.; Griffin, R. G.; Bawendi, M. G. *J. Am. Chem. Soc.* **2000**, *122*, 2532-2540.

(296)   Buonsanti, R.; Llordes, A.; Aloni, S.; Helms, B. A.; Milliron, D. J. *Nano Lett.* **2011**, *11*, 4706-4710.

(297)   Norris, D. J.; Yao, N.; Charnock, F. T.; Kennedy, T. A. *Nano Lett.* **2001**, *1*, 3-7.

(298)   Schwartz, D. A.; Norberg, N. S.; Nguyen, Q. P.; Parker, J. M.; Gamelin, D. R. *J. Am. Chem. Soc.* **2003**, *125*, 13205-13218.

(299)   Nag, J.; Jr, R. F. H. *J. Phys.: Condens. Matter* **2008**, *20*, 264016.

(300)   Bouhafs, D.; Moussi, A.; Chikouche, A.; Ruiz, J. M. *Sol. Energy Mater. Sol. Cells* **1998**, *52*, 79-93.

(301)   Dionne, J. A.; Sweatlock, L. A.; Atwater, H. A.; Polman, A. *Physical Review B* **2005**, *72*, 075405.

(302)   Kats, M. A.; Sharma, D.; Lin, J.; Genevet, P.; Blanchard, R.; Yang, Z.; Qazilbash, M. M.; Basov, D. N.; Ramanathan, S.; Capasso, F. *Appl. Phys. Lett.* **2012**, *101*, 221101.

193

(303)   Fafarman, A. T.; Hong, S.-H.; Caglayan, H.; Ye, X.; Diroll, B. T.; Paik, T.; Engheta, N.; Murray, C. B.; Kagan, C. R. *Nano Lett.* **2013**, *13*, 350-357.

(304)   Bai, H.; Cortie, M. B.; Maaroof, A. I.; Dowd, A.; Kealley, C.; Smith, G. B. *Nanotechnology* **2009**, *20*, 085607.

(305)   Lopez, R.; Haynes, T. E.; Boatner, L. A.; Feldman, L. C.; R. F. Haglund, J. *Opt. Lett.* **2002**, *27*, 1327-1329.

(306)   Lopez, R.; Feldman, L. C.; R. F. Haglund, J. *Phys. Rev. Lett.* **2004**, *93*, 177403.

(307)   Zheng, Y. B.; Juluri, B. K.; Mao, X.; Walker, T. R.; Huang, T. J. *J. Appl. Phys.* **2008**, *103*, 014308.

(308)   Barchiesi, D.; Kessentini, S.; Guillot, N.; Chapelle, M. L. d. l.; Grosges, T. *Opt. Express* **2013**, *21*, 2245-2262.